CHARACTERIZATION OF ASPHALT CONCRETE USING ANISOTROPIC DAMAGE VISCOELASTIC-VISCOPLASTIC MODEL

A Dissertation

by

SHADI ABDEL-RAHMAN SAADEH

Submitted to the Office of Graduate Studies of
Texas A&M University
in partial fulfillment of the requirements for the degree of

DOCTOR OF PHILOSOPHY

December 2005

Major Subject: Civil Engineering

CHARACTERIZATION OF ASPHALT CONCRETE USING ANISOTROPIC DAMAGE VISCOELASTIC-VISCOPLASTIC MODEL

A Dissertation

by

SHADI ABDEL-RAHMAN SAADEH

Submitted to the Office of Graduate Studies of
Texas A&M University
in partial fulfillment of the requirements for the degree of

DOCTOR OF PHILOSOPHY

Approved by:

Chair of Committee,	Eyad Masad
Committee Members,	Dallas Little
	Robert Lytton
	Amy Epps Martin
	Ibrahim Karaman
Head of Department,	David Rosowsky

December 2005

Major Subject: Civil Engineering

ABSTRACT

Characterization of Asphalt Concrete Using Anisotropic Damage Viscoelastic-Viscoplastic Model. (December 2005)

Shadi Abdel-Rahman Saadeh, B.S., University of Jordan;

M.S., Washington State University

Chair of Advisory Committee: Dr. Eyad Masad

This dissertation presents the integration of a damage viscoelastic constitutive relationship with a viscoplastic relationship in order to develop a comprehensive anisotropic damage viscoelastic-viscoplastic model that is capable of capturing hot mix asphalt (HMA) response and performance under a wide range of temperatures, loading rates, and stress states. The damage viscoelasticity model developed by Schapery (1969) is employed to present the recoverable response, and the viscoplasticity model developed at the Texas Transportation Institute (TTI) is improved and used to model the irrecoverable strain component. The influence of the anisotropic aggregate distribution is accounted for in both the viscoelastic and viscoplastic responses.

A comprehensive material identification experimental program is developed in this study. The experimental program is designed such that the quantification and decomposition of the response into viscoelastic and viscoplastic components can be achieved. The developed experimental program and theoretical framework are used to analyze repeated creep tests conducted on three mixes that include aggregates with different characteristics.

An experiment was conducted to capture and characterize the three-dimensional distribution of aggregate orientation and air voids in HMA specimens. X-ray computed tomography (CT) and image analysis techniques were used to analyze the microstructure in specimens before and after being subjected to triaxial repeated creep and recovery tests as well as monotonic constant strain rate tests. The results indicate that the different loading conditions and stress states induce different microstructure distributions at the same macroscopic strain level. Also, stress-induced anisotropy is shown to develop in HMA specimens.

DEDICATION

I dedicate this dissertation to my parents Mohammad and Sarah. I also dedicate it to the person who made this work possible by endless support and understanding, my wife Linda. In addition I dedicate this work to the one who added the glory to my life, my daughter Sarah.

ACKNOWLEDGMENTS

I would like to take this opportunity to thank Dr. Masad for being a responsible advisor, a mentor, and most important of all, a friend. Dr. Masad has always provided me with the guidance, knowledge, encouragement, and support that I needed throughout my graduate studies. His advice has been extremely valuable, and I learned so much from him. I consider myself fortunate to have had him as my advisor.

I also would like to thank the Federal Highway Administration and the International Center for Aggregates Research for funding this project.

Special thanks are due to Dr. Dallas Little, Dr. Robert Lytton, Dr. Amy Epps Martin, and Dr. Ibrahim Karaman for serving as committee members and for their valuable input to this work.

Special thanks to Cathy Bryan and Pam Kopf from the Texas Transportation Institute for their tireless help. Special thanks are also due to the staff of the Department of Civil and Environmental Engineering at Washington State University.

TABLE OF CONTENTS

CHAPTER Page

CHAPTER Page

LIST OF FIGURES

FIGURE Page

FIGURE Page

FIGURE Page

LIST OF TABLES

CHAPTER I

INTRODUCTION

PROBLEM STATEMENT

Hot mix asphalt (HMA) is a particulate composite material and its behavior is influenced by the properties and interaction of the mix constituents. HMA performance is known to be influenced by loading rate, pressure, and temperature. There is an increasing demand to develop models and associated experimental methods that can be used to predict HMA performance.

Researchers adopted different modeling approaches and performed different experimental programs to identify the HMA response under various loading and environmental conditions. Strain decomposition to recoverable and irrecoverable components is the first step toward the development of a theoretical framework for the analysis of HMA behavior and performance. This step can be achieved through adopting an experimental program that is capable of measuring the recoverable and irrecoverable strain components and also monitoring any damage associated with these components.

Probably the approach that has received the most application to HMA is the one based on theory of damage viscoelasticity, which was initiated and further developed at the Texas Transportation Institute (TTI). The researchers who worked on this approach used Schapery's viscoelastic correspondence principle (Schapery 1984).

This dissertation follows the style and format of the *Journal of Engineering Mechanics* (ASCE).

In this approach, the correspondence principle and the work potential theory were used to model the accumulated damage and microdamage healing. This approach has been mainly used to analyze fatigue damage in HMA.

Recent research at TTI has focused on developing a damage viscoplasticity model. Tashman (2003) developed a model that is based on Perzyna's formulation with the Drucker-Prager yield function modified to account for the material anisotropy and microstructure damage. The material parameters were determined based on the assumption that work hardening is the dominant deformation mechanism between the flow stress and the damage threshold; thereafter, the damage mechanism becomes dominant and deformation is primarily influenced by void growth. Including the damage parameter in the model enabled capturing the softening behavior of HMA.

Dessouky (2005) further developed the TTI elasto-viscoplastic continuum model to predict HMA response and performance. A Drucker-Prager yield surface that is modified to capture the influence of stress path direction on the material response was adopted by Dessouky (2005). The model was implemented in a finite element program and was used to predict the performance of different HMA mixtures that included aggregates with various characteristics.

The TTI model did not include the viscoelastic response of the material. Also, the monotonic compressive strength tests used in the previous studies were limited in providing a methodology for identifying the different material responses (viscoelastic versus viscoplastic). However, a comprehensive model needs to include both damage viscoelastic response and viscoplastic response in order to capture HMA response at

various temperatures and loading rates. The recent findings that the temperature-time superposition can be applied for HMA well into the damage state would significantly facilitate determining the model's parameters using a reasonable number of tests (Chehab et al. 2003, and Schwartz et al. 2004).

OBJECTIVES

The objectives of this study are to:

1. Decompose and quantify the recoverable and irrecoverable responses of HMA, which will be achieved through:
    a. Adopting an experimental methodology within a theoretical framework to decompose the HMA response, and
    b. Carrying out the experimental program on mixes that incorporate aggregates with various characteristics.
2. Develop a comprehensive anisotropic damage viscoelastic-viscoplastic model for HMA, which will be achieved through:
    a. Adding a damage viscoelastic component to the TTI viscoplastic model. This is considered a major improvement, as it allows the model to capture the response at low temperatures and high strain rates where damage viscoelasticity dominates the material response and captures the response at high temperatures and low strain rates where damage viscoplastic deformation is significant.

b. Accounting for the anisotropic behavior of the mix in both the viscoelastic and viscoplastic components.

3. Study the influence of loading conditions and stress states (repeated creep tests versus monotonic tests) on microstructure distribution in terms of the percent and size of voids (air voids and cracks) and three-dimensional aggregate orientation. The implications of the relationship between loading condition and microstructure distribution on modeling HMA are also discussed in this dissertation.

OUTLINE OF THE DISSERTATION

This dissertation is written according to Texas A&M University Thesis Manual standards. The dissertation follows the style and format of the *Journal of Engineering Mechanics* (ASCE). The dissertation consists of six chapters organized as follows:

Chapter I is an introduction. The problem statement is presented followed by the objective and the outline of the dissertation.

Chapter II presents a literature review that begins by offering preliminaries on the different material responses that cover elastic, viscoelastic, plastic, and viscoplastic behaviors. This is followed by discussion on the different approaches for analyzing and modeling the response of HMA. The models are divided into empirical, damage viscoelastic, damage viscoplastic, damage elasto-viscoplastic, and anisotropic damage elasto-viscoplastic models.

Chapter III presents the experimental measurements, data analysis, and the approach for the analysis of the irrecoverable and recoverable strain components.

Chapter IV presents the integration of a damage viscoelastic constitutive relationship with a viscoplastic relationship in order to develop a comprehensive anisotropic damage viscoelastic-viscoplastic model that is capable of capturing HMA response and performance under a wide range of temperatures, loading rates, and stress states.

Chapter V presents an experiment to study the influence of loading conditions and stress states on microstructure distribution and its implications on modeling HMA response.

Chapter VI presents the conclusions and recommendations of this study.

CHAPTER II

LITERATURE REVIEW

INTRODUCTION

The literature review starts by offering preliminaries on the different material responses that cover elastic, viscoelastic, plastic and viscoplastic behaviors. This is followed by discussion on the different approaches for modeling the response of asphalt mixes. The focus will be on the experimental methods used in these approaches to extract the model's parameters. The models are divided into empirical models, damage viscoelastic, damage viscoplastic, damage elasto-viscoplastic, and anisotropic damage elasto-viscoplastic models.

PRELIMINARIES ON MATERIAL RESPONSE

The elastic behavior is described by the response at which the strain is recovered upon unloading instantaneously. For a linear elastic response, the stress and strain are related using Hooke's law, which has the form in Eq. (2-1) for a uniaxial condition:

$$\sigma = E\,\varepsilon \tag{2-1}$$

where σ is stress, ε is strain, and E is modulus of elasticity or Young's modulus. It can be seen that for a material to be linear elastic, stress should be proportional to strain. Moreover, it should adhere to the compatibility conditions or the superposition principle.

Slaughter (2002) describes elastic behavior as "the material in which the change in the stress at a material point in a body, between two arbitrary configurations of the

body, is independent of the time taken in going from on configuration to the other and to the path followed in the space of all possible configurations."

Fig. 2.1 presents the response of the material within its linear range under loading and unloading conditions. Poisson's ratio is the ratio of instantaneous lateral strain to axial strain (direction of loading) during a uniaxial tensile or compressive test. Fig. 2.2 illustrates different material responses that do not obey linear elastic behavior under loading and unloading conditions.

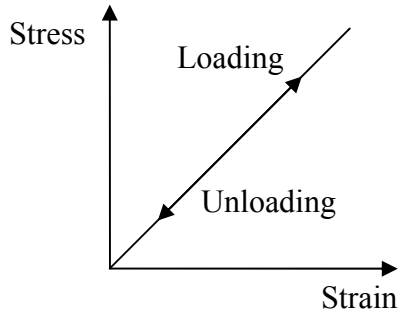

Fig. 2.1. Stress-Strain Diagram for Linear Elastic Material

In Fig. 2.2A, the loading and unloading paths coincide and the strain is recoverable; however, the stress and strain are not proportional, which is typical for nonlinear elastic material. If some of the strain ceases to recover upon unloading, then the material is described as elasto-plastic, as shown in Fig. 2.2B. On the other hand, if all strain continues to recover upon unloading even when the stress is reduced to zero, then the material is called viscoelastic, as in Fig. 2.2C.

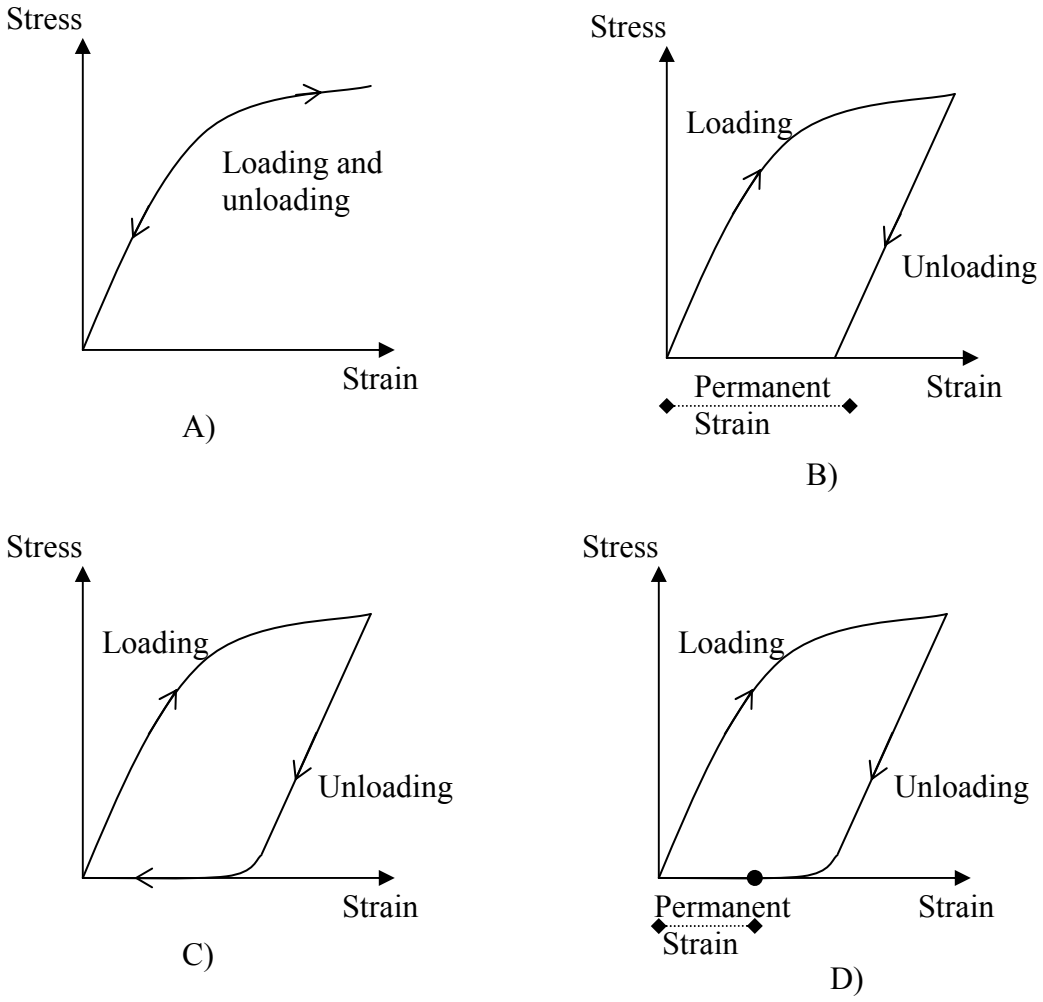

Fig. 2.2. Illustration of Different Material Responses A) Nonlinear Elastic, B) Elasto-Plastic, C) Viscoelastic, and D) Elasto-viscoplastic (after Boresi and Schmidt 1993)

As described later, this behavior is usually associated with solid-like viscoelastic materials, while liquid-like viscoelastic material can be modeled to retain some permanent deformation after the load is removed. In the viscoelastic response, the

elastic portion, theoretically speaking, recovers immediately upon the removal of stress. The strain that recovers as a function of time at zero stress is referred to as viscoelastic or, sometimes, delayed elastic. Fig. 2.2D depicts the behavior of an elasto-viscoplastic material. The elastic strain is recovered immediately upon unloading; the viscoelastic strain is recovered with time, while the viscoplastic strain remains unrecovered even after the removal of the stress.

A viscoelastic material exhibits some properties of viscous fluid and some of elastic solid. Hooke's law is used to describe the linear elastic behavior in which the stress is proportional to strain and independent of strain rate. Newton's law is used to describe the Newtonian viscous material in which the stress is proportional to strain rate and independent of strain (Moore 1993).

The response under creep loading (constant load) offers explanation of the different material responses as shown in Fig. 2.3. It can be seen that the elastic material has instantaneous response and the strain is fully recovered upon the removal of the load (Fig. 2.3A). However, the viscous material develops increasing strain with time and the strain does not recover upon unloading (Fig. 2.3B). The behavior of a viscoelastic material combines aspects of the elastic and viscous responses. There is an instantaneously recoverable part which reflects the elastic response and another part that recovers strain as a function of time. The rate at which the viscoelastic material recovers strain and whether all strain is recovered or some permanent strain remains varies among viscoelastic materials (Young et al. 1998). The plastic response is not time-dependent as shown in Fig. 2.3B, and strain is not recovered upon the removal of stress Fig. (2.3).

The elasto-viscoplastic response in depicted in Fig 2.3D. In this response, it is assumed that all the viscoelastic response is recovered if sufficient time is allowed, and permanent strain is caused by the plastic and viscoplastic responses. It can be seen that the strain has an instantaneous part, ε^{e}, and a viscoelastic component that develops with time, ε^{ve}. The plastic part can be distinguished directly since upon unloading the recoverable strain is not equal to the instantaneous strain developed upon loading. The recovered strain with time after unloading is termed viscoelastic ε^{ve}; this part is time-dependent. The unrecovered part is divided into two parts, the first is plastic, ε^{p}, as described above, and another is viscoplastic, ε^{vp}, which is the unrecoverable strain that develops as a function of time.

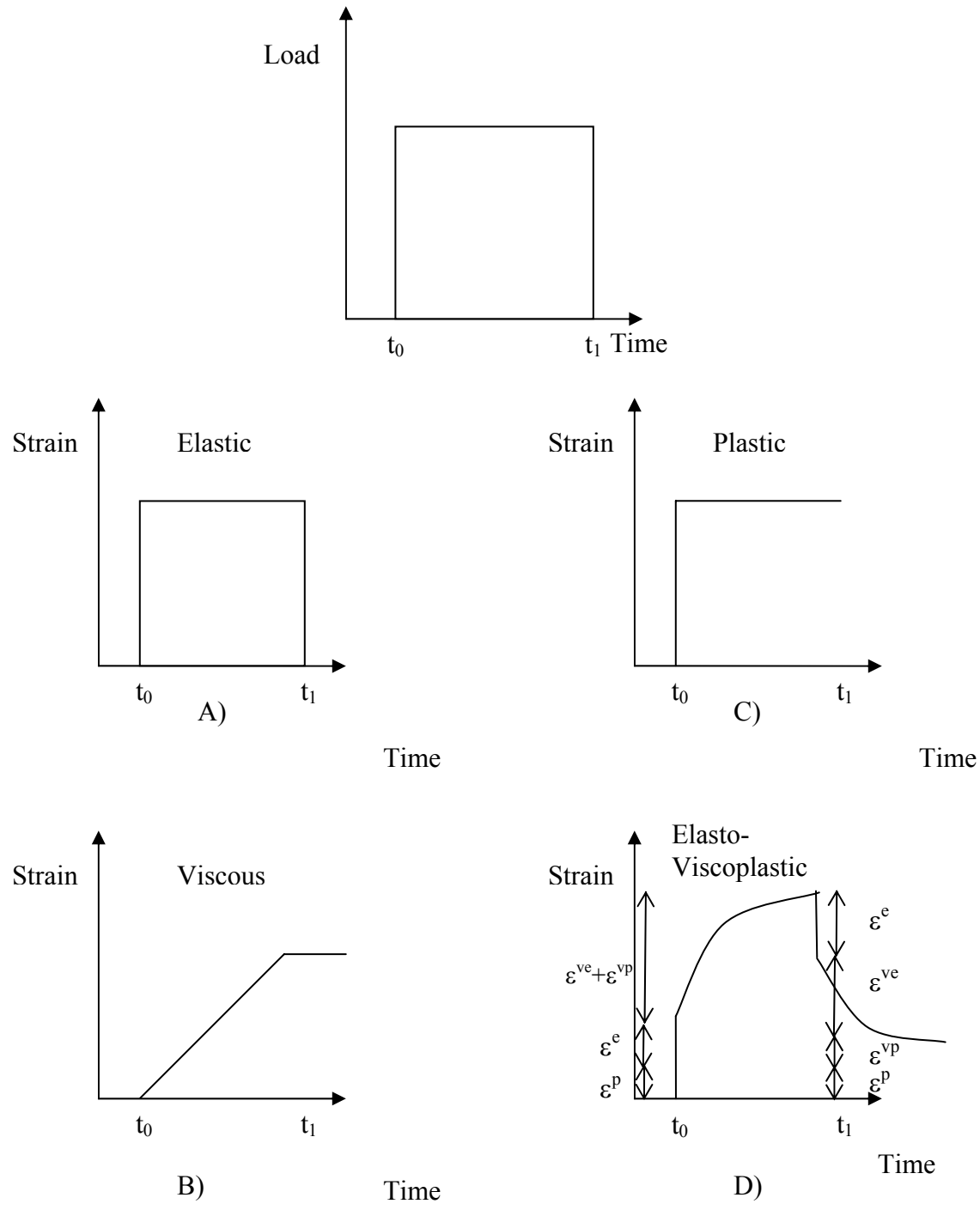

Fig. 2.3. Response to Time Load A) Elastic, B) Viscous, C) Plastic, and D) Viscoelastic and Viscoplastic

It is noted that some viscoelastic response can be modeled such that permanent strain remains after unloading as shown in Fig. 2.4A or all strain is recovered as shown in Fig. 2.4B. The choice of a viscoelastic model versus an elasto-viscoplastic model to describe the material behavior is dependent on the mechanisms (sliding, binder deformation, and rate of permanent strain accumulation) that govern the material behavior, and whether these mechanisms can be described by viscoelastic behavior or viscoplastic behavior.

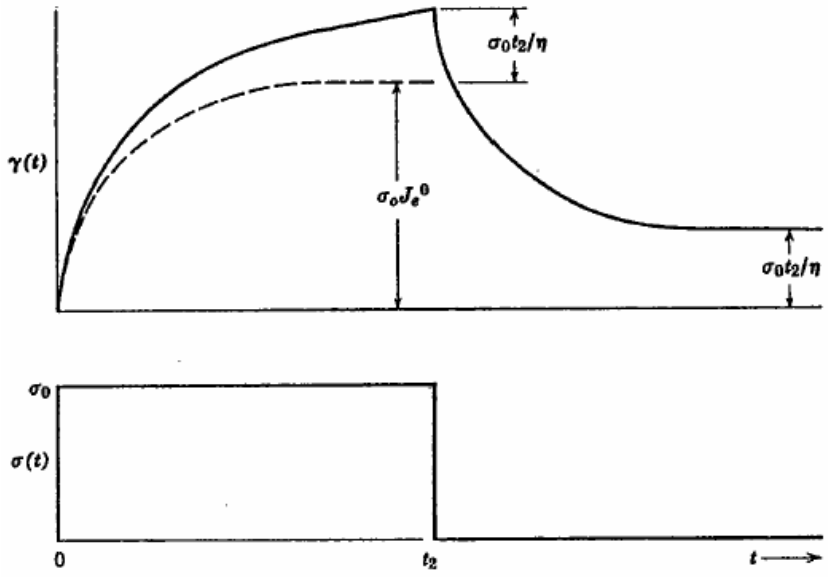

A)

Fig. 2.4. A) Shear Creep and Creep Compliance for Viscoelastic Liquid, B) Shear Creep and Creep Recovery for Viscoelastic Solid (Ferry 1980)

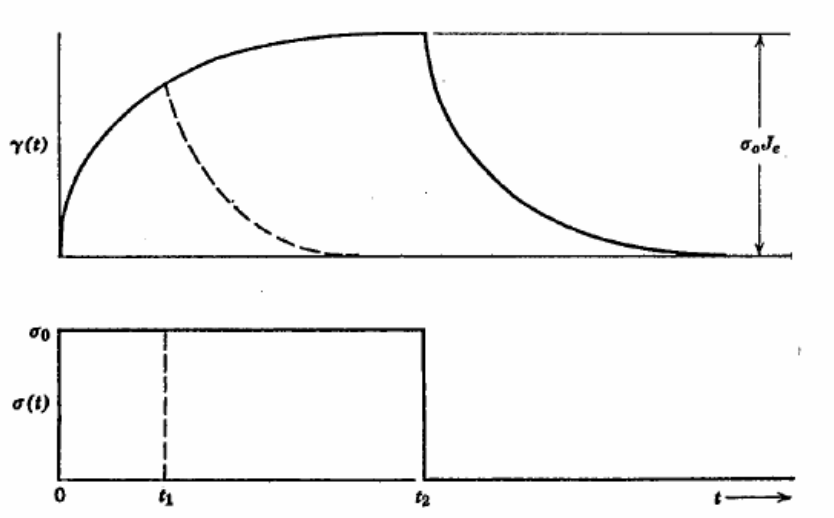

B)

Fig. 2.4. Continued

In general, there are three stages of creep, as illustrated in Fig. 2.5. Each of these stages could happen at different load-temperature combinations. The first stage is called primary and is expected to happen at relatively low stress and temperature at which the creep rate for the later stage is zero. If an intermediate stress-temperature combination is achieved, the second stage will proceed and the creep rate will be constant. At relatively high stress-temperature level, the third stage, which is called tertiary, will take over and will end in failure.

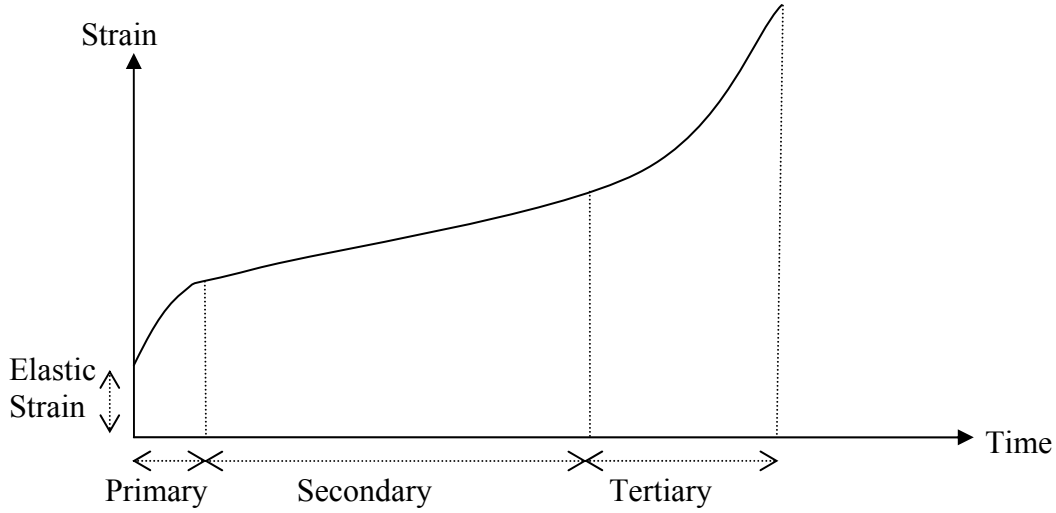

Fig. 2.5. Creep Curve and Its Stages

IDENTIFYING MATERIAL RESPONSE

The literature review in this section focuses on the HMA mechanical response and approaches used to define the different components of the response. The approaches are divided into empirical damage viscoelastic, damage viscoplastic, damage elasto-viscoplastic, and anisotropic damage elasto-viscoplastic models.

Empirical Relationships

The term "empirical relationships" is used here to refer to studies in which the main objective was to define the different strain components from experimental measurements without focusing on developing mechanistic models to describe these strains. The development of an approach for decomposing the material response into the

different components is valuable and necessary as it constitutes the first step towards developing models for these strain components.

Perl et al. (1983)

The experimental observations made by Perl et al. (1983) and Sides et al. (1985), and later by other researchers, suggest that the total strain for an asphalt mix can be described by recoverable and irrecoverable components, some of which are time-dependent and some of which are time-independent. The total elasto-viscoplastic strain can be separated into four components, as shown earlier in Fig. 2.3D, for the first cycle of a creep test as follows:

$$\varepsilon = \varepsilon^{e} + \varepsilon^{ve} + \varepsilon^{p} + \varepsilon^{vp} \tag{2-2}$$

where ε is the total strain; ε^{e} is the elastic strain, which is recoverable and time-independent; ε^{ve} is the viscoelastic strain, which is recoverable and time-dependent; ε^{p} is the plastic strain, which is irrecoverable and time-independent; and ε^{vp} is the viscoplastic strain, which is irrecoverable and time-dependent. Upon removal of the load, the instantaneous response includes only the elastic response and the time-dependent response after unloading is due to viscoelasticity only. After some time, the response of the material tends to be asymptotic to the sum of the plastic and viscoplastic, which are irrecoverable components (Lytton et al. 1993). It is noteworthy that Fig. 2.3D and Eq. (2-2) form the basis of modeling the response of HMA in most of the studies available in the literature.

Perl et al. (1983) developed relationships that describe the strain components as

follows:

$$\varepsilon_e = E\sigma \tag{2-3}$$

$$\varepsilon_p = \left(\sigma / H\right) \cdot N^a \tag{2-4}$$

$$\varepsilon_{ve}(\sigma, t) = A(\sigma)\left\{\sum_{i=1}^{N}\left[t-(2i-2)T_L\right]^{\alpha} - \left[t-(2i-1)T_L\right]^{\alpha}\right\} \tag{2-5}$$

$$\varepsilon_{vp}(\sigma, t_n, N) = B(\sigma)T_L^{\beta}(N-1)^b\left[1+\left(t_n / T_L\right)^{\beta}\left(b/N - b\right)\right] \tag{2-6}$$

where E is Young's modulus, H is the slope of the stress versus plastic strain, N is number of loading cycles, a, b, α, and β are material constants, t is time, $A(\sigma)$ and $B(\sigma)$ are material functions of stress, t_n is the time elapsed from the beginning of the N^{th} cycle, and T_L is the loading period.

Experimental limitations could make it very difficult to separate the time-dependent from the time-independent components. For example, it is difficult to totally remove the load within a very short time that would allow the deformation measurement devices to record the instantaneous response. In fact, one has to assume a small time at which the response is considered instantaneous. Therefore, for the sake of simplicity, some of the strain components are sometimes lumped into one component. Abdulshafi and Majidzadeh (1984) and Bonnier (1993) combined the irrecoverable components into one viscoplastic strain and the recoverable components into a viscoelastic strain.

Uzan (1996)

Uzan (1996) used the same approach used by Sides et al. (1985) to analyze the strain response under creep loading and a wide range of temperatures. Uzan (1996) showed that the irrecoverable components make up most of the axial and residual strain for HMA at relatively high temperatures, as shown in Fig. 2.6. Therefore, it was noted by Uzan (1996) that rutting, which usually occurs during a very hot summer combined with heavy traffic loads, is mainly due to the viscoplastic (including plastic) deformation, whereas the viscoelastic component contributes very little to such a phenomenon. These findings were also supported by a previous study by Sides et al. (1985) for sand-asphalt mixtures.

Damage Viscoelastic Models

Kim and Little (1990) and Kim et al. (1997)

Probably the approach that has received the most significant attention in HMA modeling is the one based on theory of damage viscoelasticity. The researchers who worked on this approach used Schapery's viscoelastic correspondence principle (Schapery 1969). In this approach, the correspondence principle and the work potential theory were used to model the accumulated damage and microdamage healing.

Two testing protocols need to be performed in these models. The first test has to be done at small stress or strain levels such that no damage occurs. This test is used to measure the linear viscoelastic properties that define the intact undamaged material. The linear viscoelastic properties are used to calculate the pseudo-strain (Schapery 1984).

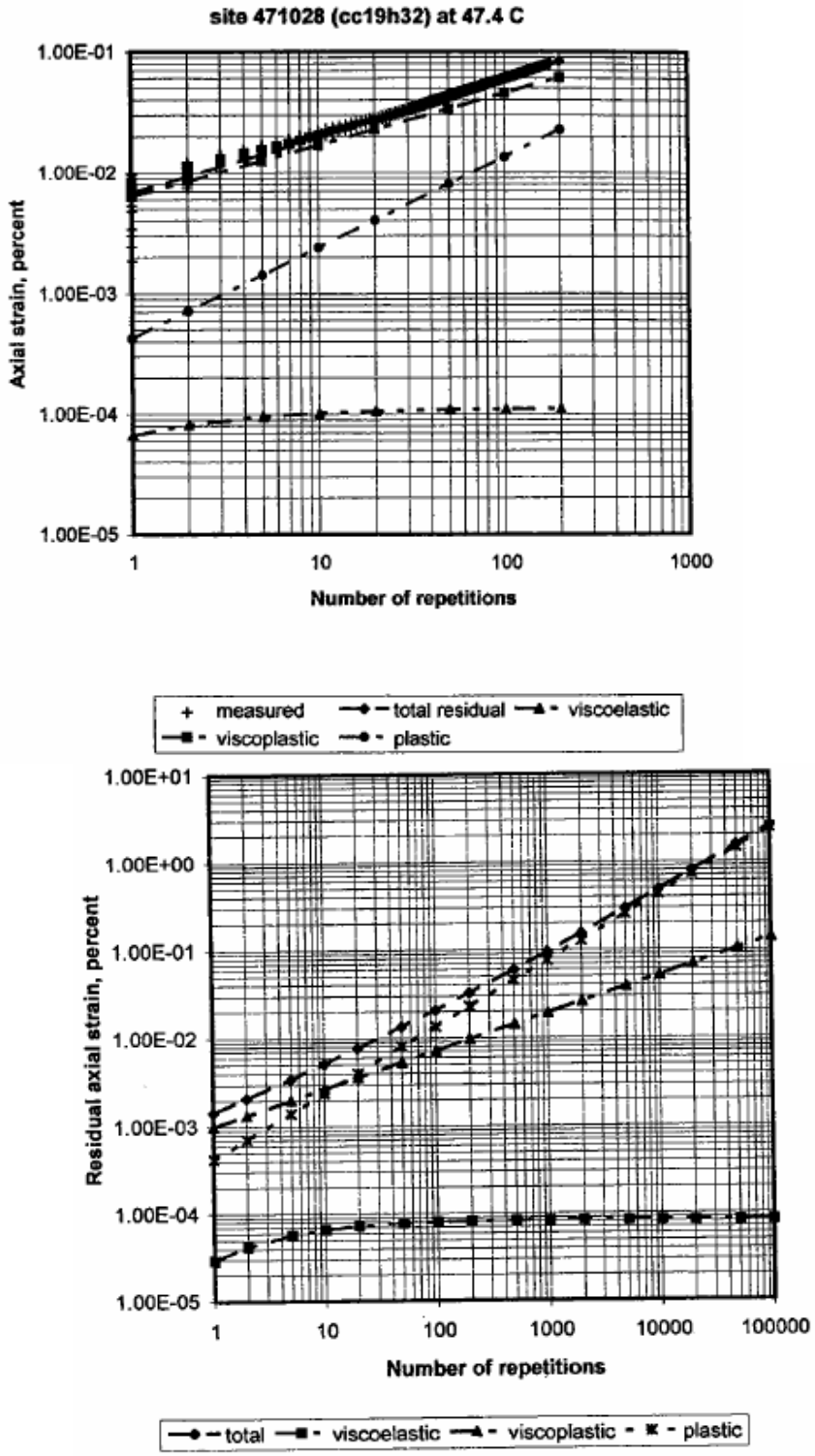

Fig. 2.6. Components of Axial and Residual Strain versus Number of Repetitions at 105 °F (Uzan 1996)

The second test is supposed to be conducted at higher stresses that induce damage in the material. The difference between the responses at the low and high stresses is quantified by the dissipated pseudo-strain energy, or a damage function.

Kim et al. (1997) used a constant strain rate tensile monotonic test at different strain rates to validate the application of the correspondence principle at variable strain rates, and obtain the viscoelastic properties. Then, a tensile cyclic loading with constant stress/strain amplitudes without a rest periods was conducted to account for the damage growth of the material. In addition, Kim et al. (1997) conducted tensile cyclic loading with constant stress/strain amplitudes with rest periods to account for the material healing. The effect of the rest period was reflected in an increase in the pseudo-stiffness (applied stress/pseudo-strain) and compared with the no rest period stiffness. It should be mentioned that this approach was mainly applied to the fatigue of asphalt mixes, and it was not used for rutting.

Si et al. (2002)

Si et al. (2002) developed a nonlinear damage viscoelastic model that utilized the pseudo-strain energy and the pseudo-stiffness to characterize the fatigue microdamage and healing in asphalt concrete. They applied a loading pattern that consisted of a strain-controlled relaxation test, a strain-controlled haversine repeated loading at low strain level to characterize the viscoelastic response. Then they conducted haversine repeated loading at higher strain values to induce damage and calculated the dissipated pseudo-strain energy. They were able to monitor the material healing by introducing rest periods

after loading periods. The loading period was 0.1 second the rest period was 0.9 second. Fig. 2.7 presents the pattern of loading used by Si et al. (2002). The test temperature was 25 °C, as the interest was fatigue damage.

The main contribution of this study is detecting the nonlinear viscoelastic response of the material and developing an approach to normalize with respect to this nonlinear response when the dissipated energy responsible for damage is calculated.

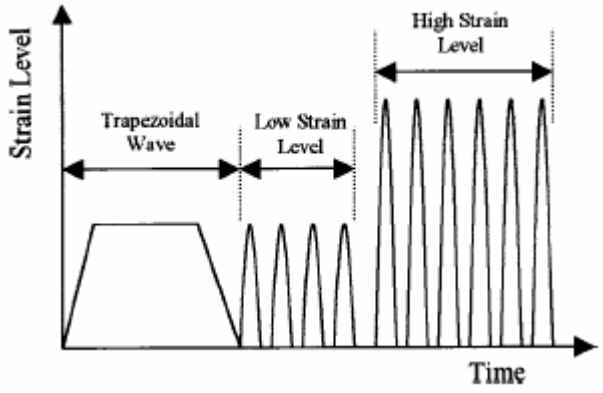

Fig. 2.7. Graphical Illustration of the Input Wave Form (Si et al. 2002)

Sousa et al. (1993)

Sousa et al. (1993) developed a damage viscoelastic model to predict permanent deformation of HMA. The developed model was intended to capture important phenomena that influence permanent deformation of HMA including the dilatancy under shear loading, the effect of confining pressure on the shear modulus, the temperature and rate of loading dependency, and the residual accumulation of permanent deformation

under repetitive loading. Sousa et al. (1993) emphasized that a valid constitutive model for HMA cannot assume the material as isotropic and linear elastic. In addition, it is important to develop standardized test procedures to determine the material parameters for a constitutive model.

The model consisted of a number of three-dimensional Maxwell elements in parallel. Each Maxwell element was composed of a nonlinear spring and dashpot. The dilatancy effect and the increase in effective shear modulus under confining pressure are due to the aggregate skeleton, whereas temperature and rate dependency are associated with the asphalt binder (Sousa et al. 1993). The hardening was associated with the spring, and temperature and rate dependency were associated with the dashpot. Damage was accounted for by including a damage parameter in the equilibrium equation for the dashpot.

Simple shear at constant height, uniaxial strain and volumetric tests were used to determine the nonlinear elastic material parameters. The viscous parameters were determined from the simple shear frequency sweep test, and the damage parameters were determined from the simple shear strain sweep test at constant height. Damage was found to follow an S-curve shape ranging between no damage at very low shear strain and almost complete failure at relatively high values of shear strain, as shown in Fig. 2.8. Adding a damage component in their model significantly improved the ability to simulate test measurements.

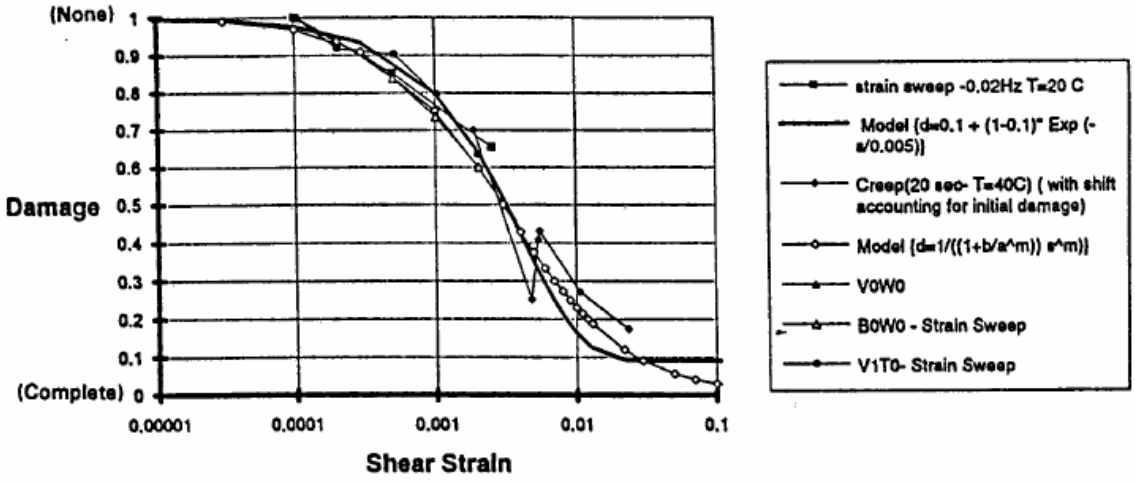

Fig. 2.8. Shape of the Damage Function Obtained from Shear Strain Sweeps and Shear Creep Tests (Sousa et al. 1993)

Damage Viscoplastic Models

Scarpas et al. (1997)

Scarpas et al. (1997) presented a damage viscoplastic model. They utilized Perzyna's theory of viscoplasticity with Desai's yield surface (Desai et al. 1986, Desai and Zhang 1987, Desai 1990) as follows:

$$f = \frac{J_2}{P_a^2} - F_a \cdot F_b \tag{2-7}$$

in which,

$$F_a = \gamma\left(\frac{I_1 + R}{P_a}\right)^2 - \alpha\left(\frac{I_1 + R}{P_a}\right)^n \tag{2-8}$$

$$F_b = \left(1 - \beta \cdot \cos 3\theta\right)^{-1/2} \tag{2-9}$$

$$\cos 3\theta = \frac{3\sqrt{3}}{2} \cdot \frac{J_3}{J_2^{3/2}} \tag{2-10}$$

where I_1, J_2, and J_3 are the first invariant of the stress tensor, the second invariant of the deviatoric stress tensor, and the third invariant of the deviatoric stress tensor, respectively; P_a is the atmospheric pressure; R is the triaxial tensile strength; and α, β, γ, and n are material parameters defining the yield surface.

Scarpas et al. (1997) also included an additional strain component, ε_{cr}, to account for damage due to crack formation as follows:

$$w = l_c \cdot \varepsilon_{cr} \tag{2-11}$$

where w is the crack opening and l_c is a characteristic length scale.

Monotonic triaxial compression and tension tests were used to determine material parameters related to stress path and rate dependency. In addition, incremental creep tests were used to determine material parameters related to hardening and viscosity. The model was implemented in a dynamic nonlinear Finite Element (FE) system to simulate flexible pavement response. The FE simulation showed that all elements in the vicinity of the load were subjected to intense shearing deformation and that the shear stresses (compression and tension) comprised the major domain of the pavement top layer response. Scarpas et al. (1997) noted that shear compression can be applied by a standard triaxial testing apparatus, whereas shear tension is not easy to apply.

Damage Elasto-Viscoplastic Models

Schwartz et al. (2004)

The researchers developed a model that accounts for viscoelastic, viscoplastic, and damage behavior of HMA. The damage viscoelastic part of the model is similar to that by Kim et al. (1997). The testing regime was designed to calibrate the viscoplastic model and to evaluate the applicability of low-strain time-temperature superposition for large-strain viscoplastic response. They performed two series of uniaxial compression creep and recovery tests. The tests were divided into two groups, uniform load tests and uniform time tests. The uniform load tests were designed such that the stress remains the same and the duration of loading and recovery increases from one cycle to another. The uniform time tests were designed such that the duration of the loading and recovery period are fixed from one cycle to another and the stress increases.

The focus of the authors in this paper was limited to the viscoplastic response component at intermediate and high temperatures. The viscoplastic model has the form:

$$\varepsilon_{vp} = \left(\frac{p+1}{D}\right)^{\frac{1}{p+1}} \left(\sigma^{q}\right)^{\frac{1}{p+1}} t^{\frac{1}{p+1}} \tag{2-12}$$

where ε_{vp} is the viscoplastic strain, p and D are material properties, σ is uniaxial stress, and t is time.

The viscoplastic strains were determined from the recovery period after each loading cycle from both series of uniform load and uniform stress. Nonlinear least square optimization was used to fit the data to the results and find the model parameters. Fig. 2.9 presents the viscoplastic model fitting.

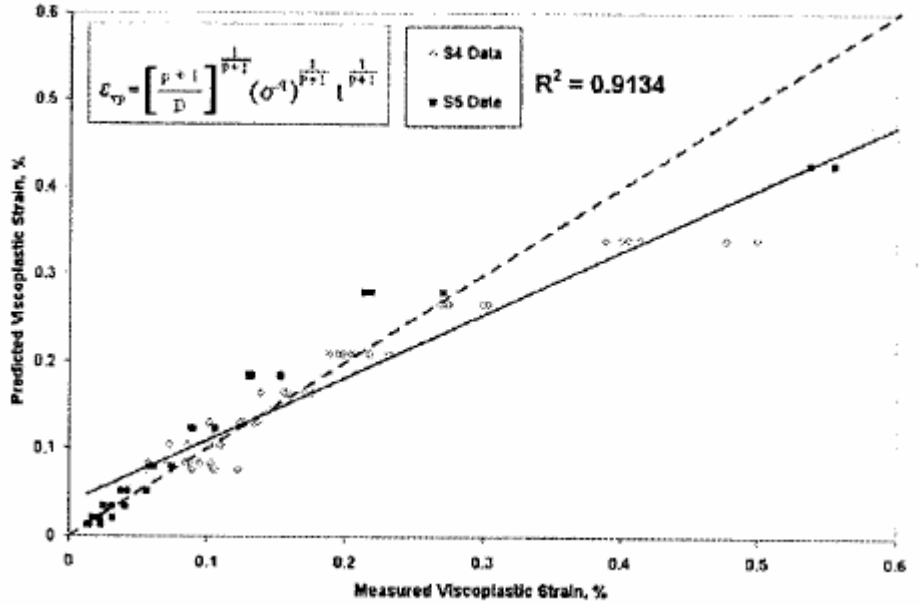

Fig. 2.9. Measured versus Predicted Viscoplastic Strain (Schwartz et al. 2004)

Chehab et al. (2003)

Chehab et al. (2003) developed a model that accounts for elastic, viscoelastic, plastic, and viscoplastic responses of asphalt concrete. This model includes a viscoelastic relationship to characterize the elastic and viscoelastic responses and a viscoplastic relationship to characterize the plastic and viscoplastic responses.

The viscoelastic model is based on the Schapery's continuum damage approach, similar to Kim et al. (1997). The viscoelastic strain is determined by evaluating the inverse to the integral:

$$\varepsilon_{ve} = E_R \int_0^{\xi} D(\xi - \xi') \frac{d\left(\frac{\sigma}{C(S^*)}\right)}{d\xi'} d\xi' \qquad (2\text{-}13)$$

where ε_{ve} is the viscoelastic strain, E_R is the reference modulus, $D(\xi')$ is uniaxial creep compliance, ξ is the reduced time, ξ' is an integration constant, C is the pseudo-stiffness, and S^* is damage parameter.

Chehab et al. (2003) used monotonic constant strain rate test in tension at low temperatures of -10 °C and 5 °C to determine the parameters and validate the viscoelastic model. Fig. 2.10 presents the experimental and predicted viscoelastic strain.

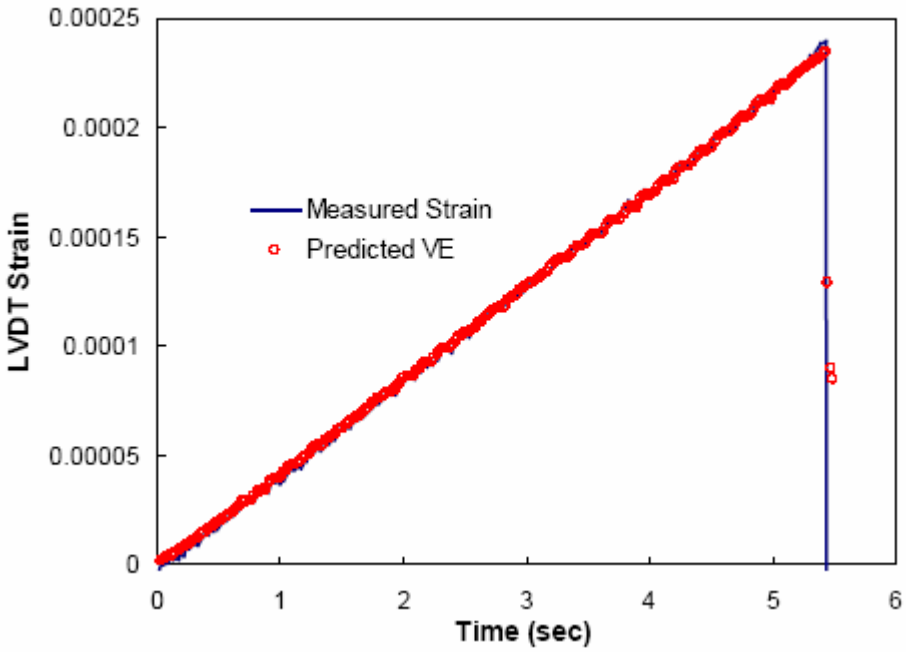

Fig. 2.10. Predicted versus Experimental Strain at -10 °C (Chehab et al. 2003)

The developed viscoplastic strain rate was based on relationships proposed by Uzan (1996) and Schapery (1999). The model has a form similar to the one discussed previously by Schwartz et al. (2004).

Chehab et al. (2003) used constant cross head rate tests in uniaxial tension at temperatures of (-30 °C to 40 °C) to model the viscoplastic component of the strain. The monotonic tests were used as input to the developed viscoelastic strain to predict the viscoelastic strain. The predicted viscoelastic strain is subtracted from the total measured strain, and the resulting strain was attributed to viscoplasticity. Fig. 2.11 presents the predicted viscoplastic and viscoelastic of total strain at 40 °C.

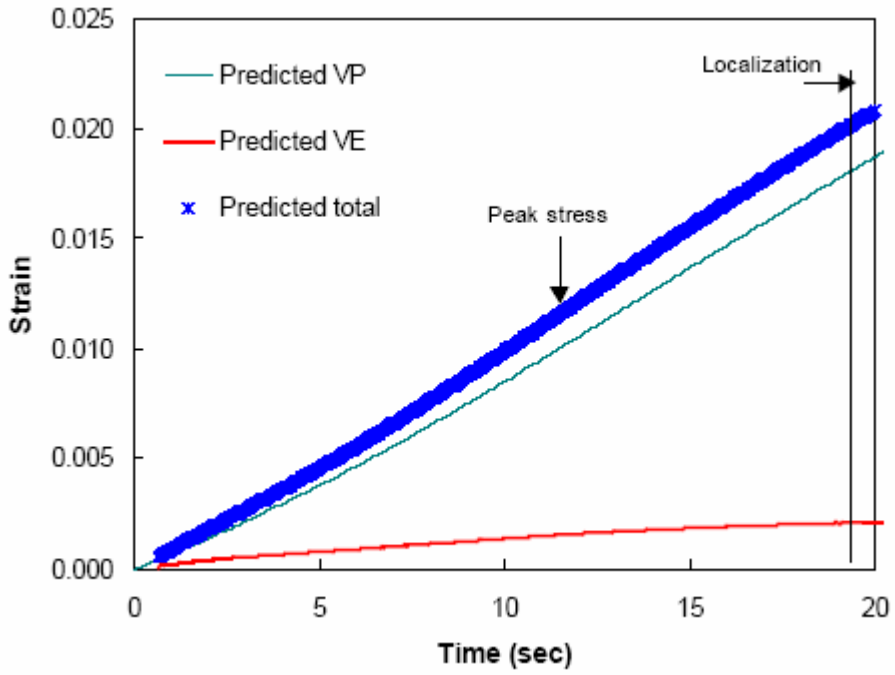

Fig. 2.11. Predicted Viscoplastic, Viscoelastic, and Total Strain at 40 °C (Chehab et al. 2003)

The model was verified under a single stress path, which is a monotonic testing in tension. Experimental measurements as well as numerical simulations have shown that rutting in asphalt mixes takes place close to the surface where the stress path is dominated mainly by shear stresses (Sousa et al. 1993), which is not well captured in monotonic tension test.

Anisotropic Damage Elasto-Viscoplastic Models

Tashman (2003)

Tashman (2003) developed a model that is based on Perzyna's formulation with the Drucker-Prager yield function modified to account for the material anisotropy and microstructure damage. The material anisotropy is captured through microstructural analysis of two-dimensional sections of HMA in terms of aggregate distribution. Furthermore, a damage parameter is included in the model in order to quantify the nucleation of cracks and growth of air voids and cracks (voids).

The model is based on Perzyna's theory on time rate flow rule where the viscoplastic strain rate is defined using the flow rule as follows:

$$\dot{\varepsilon}_{vp} = \Gamma \cdot < \phi(f) > \cdot \frac{\partial g}{\partial \sigma} \tag{2-14}$$

where, Γ is the fluidity parameter, which establishes the relative rate of viscoplastic strain and is experimentally determined; and $\frac{\partial g}{\partial \sigma}$ is a measure of the direction of viscoplastic strain.

Triaxial compressive strength tests conducted at five strain rates and three confining pressures were used to systematically determine important material parameters that represent different phenomena influencing the permanent deformation of HMA. These phenomena include the aggregate structure friction, aggregate structure dilation, confining pressure dependency, strain rate dependency, anisotropy, and damage.

The material parameters were determined based on the assumption that work hardening is the dominant deformation mechanism between the flow stress and a damage threshold; thereafter, the damage mechanism becomes dominant and deformation is primarily influenced by void growth. The anisotropy parameter (vector magnitude) provided the capability to account for aggregate structure distribution in the model.

Including the damage parameter in the model enabled capturing the softening behavior of HMA, which occurs as soon as the damage mechanism overcomes work hardening resulting in a drop in the load-carrying capacity of the material. The model was found to be in good agreement with the experimental data.

The developed model did not include the viscoelastic response of the material. The monotonic compressive strength tests were limited in providing a methodology for identifying the different material responses (viscoelastic versus viscoplastic). An assumption was made that the elastic response can be defined by the linear portion of the stress-strain relationship.

Dessouky (2005)

Dessouky (2005) developed an elasto-viscoplastic continuum model to predict HMA response and performance. The model incorporates a Drucker-Prager yield surface that is modified to capture the influence of stress path direction on the material response. Parameters that reflect the directional distribution of aggregates and damage density in the microstructure are included in the model. The elasto-viscoplastic model is converted into a numerical formulation and is implemented in FE analysis using a user-defined material subroutine (UMAT). A fully implicit algorithm in time-step control is used to enhance the efficiency of the FE analysis. The FE model was used to simulate permanent deformation of pavement sections.

The developed model decomposes the total strain rate $\dot{\varepsilon}$ into:

$$\dot{\varepsilon}_{ij} = \dot{\varepsilon}_{ij}^{e} + \dot{\varepsilon}_{ij}^{vp} \tag{2-15}$$

where the superscript (*e*) refers to the elastic part and (*vp*) refers to the viscoplastic part. The elastic strain component can be defined according to Hook's law as follows:

$$\dot{\sigma}_{ij} = D_{ijkl}\dot{\varepsilon}_{kl}^{e} \tag{2-16}$$

where $\dot{\sigma}$ is the stress rate tensor and D_{ijkl} is the fourth-order elastic stiffness tensor. The viscoplastic component dominates the response for the material at higher magnitudes of stress and higher temperatures. The viscoplastic strain rate component is based on Perzyna's theory as described earlier in Tashman (2003).

The model builds upon the formulation developed by Tashman (2003), but it is expanded to include the elastic response of the material and to account for the influence of

stress path direction. In addition, the procedure to account for anisotropy in the constitutive relationship is simplified. The new model accounted for the following phenomena: elastic response prior to reaching the yielding stress threshold; shear as the dominant stress causing permanent deformation; dilation and hydrostatic pressure dependency of the material; stress path dependency of the viscoplastic response; work hardening/softening of the material; aggregate directional distribution in the microstructure; and damage in terms of cracks and air voids.

Triaxial compression and extension strength tests on granite, gravel, and limestone mixes were used to determine model parameters. These tests were conducted at different loading rates and confining pressures.

The developed model did not include the damage in the elastic response of the material. Similar to the model by Tashman (2003), the monotonic triaxial strength tests are limited in their ability to identify the different material responses.

CHARACTERIZING DAMAGE USING X-RAY COMPUTED TOMOGRAPHY

X-ray computed tomography (CT) is fast becoming a powerful nondestructive tool in characterizing the microstructure of many engineering materials such as concrete, soil, rocks, metals, and HMA. Although some of these materials vary significantly in their microstructural composition and distribution, the motivation behind using this new technology has been the same, and that is the nondestructive nature of X-ray CT, its accuracy, and the need to characterize the material microstructure. A review of the application of X-ray CT to the characterization of asphalt mixes is provided by Masad

(2004).

Synolakis et al. (1996) presented a new method for computing the microscopic internal displacement fields associated with permanent deformation of three-dimensional HMA cores while satisfying the small gradient approximation of continuum mechanics. They computed the displacement field associated with diametral loading of a cylindrical asphalt core using X-ray CT to collect three-dimensional images from sequences of two-dimensional images scanned before and after loading. The pair of three-dimensional images was then used to compute the displacement field by comparing their three-dimensional representation before and after the deformation.

Shi et al. (1999) used X-ray CT to monitor the evolution of internal failure in different soils, particularly the formation of shear bands. They used an apparatus that can be fitted into the chamber of a medical CT. CT images were then taken on different cross-sections inside the specimens at different loading stages to monitor soil deformation continuously. They showed that X-ray CT is a powerful nondestructive tool for studying the deformation patterns and capturing the formation of cracks and shear bands in soils.

Landis and Keane (1999) used high resolution X-ray microtomography to measure internal damage and crack growth in small mortar cylinders loaded in uniaxial compression. In their experiment, small mortar cylinders were inserted into a small loading frame that could be mounted directly on the X-ray rotation table. This was done in order to scan the specimens at varying strain values so that internal damage could be quantified and correlated with load deformation information. Aluminum was chosen for the loading frame

because of its relatively low X-ray absorption, leading to better X-ray absorption resolution in the specimens. Multiple tomographic scans were made of the same specimen at different levels of deformation applied through a custom-built loading frame, and image analysis of the scanned images was used to measure the internal crack growth during each deformation increment.

Landis and Keane (1999) used X-ray CT to characterize damage in cement concrete. They showed that beyond 30% of ultimate strength, cracking occurred at the cement-aggregate interface. At about 70% of the peak load, these distributed cracks started to localize and matrix cracking occurred, which macroscopically became large-scale axial splitting. Post-peak response was characterized by additional matrix cracking and frictional mechanisms in a relatively narrow band. However, measured post-peak behavior was found to be highly dependent on the testing setup and specimen geometry.

Masad et al. (2002a) used X-ray CT along with image analysis technique (IAT) to characterize the statistical distribution of air void sizes at different depths in HMA specimens. They found that air void size distribution follows a Weibull distribution, which was used to quantify the effect of compaction effort, method of compaction, and aggregate size distribution on air voids. They also found that air void size distribution in Superpave gyratory compacted specimens exhibit a "bath-tub" shape, where larger air voids were present at the top and bottom parts of a specimen. This shape was more pronounced at higher compaction efforts. Specimens prepared with different aggregate sizes were found to have noticeably different air void sizes. Specifically, larger air voids were present in specimens that consisted of smaller aggregate particles.

Tashman et al. (2004) used X-ray CT to characterize damage evolution in HMA at relatively high temperatures. HMA specimens were loaded using a triaxial compression setup to four predefined strain levels at three confining pressures. X-ray CT was used to capture the microstructure of the HMA specimens before and after they were deformed, and IAT was used to characterize the evolution of air voids and cracks (voids) in the deformed specimens. IAT was developed to distinguish between air void growth and crack evolution.

Damage in HMA was shown to initiate following a period of microstructure hardening. The damage was found to be a localized phenomenon in the sense that there exists a critical section in a specimen that is mainly responsible for failure. Growth and propagation of cracks in this critical section were significantly larger than in the rest of the specimen. Tashman et al. (2004) found that the top part of the specimens exhibited significant cracking, the middle part exhibited significant dilation, and minor microstructural changes occurred in the bottom part. They have attributed the variations within a specimen to the heterogeneity of the HMA microstructure.

CHAPTER III

AN EXPERIMENTAL PROGRAM TO IDENTIFY ASPHALT CONCRETE RESPONSES FOR CONSTITUTIVE MODELING

OVERVIEW

The response of hot mix asphalt (HMA) to different loading paths has long been investigated by researchers. Researchers adopted different modeling approaches and performed different experimental programs to identify the different responses (elastic, viscoelastic, plastic, and viscoplastic) of HMA. In this chapter a comprehensive material identification experimental program is proposed. The experimental program is designed such that it is able to quantify and decompose the response to its components including elastic, plastic, viscoelastic, and viscoplastic. This experimental program is adopted within a theoretical framework that is capable of modeling the different HMA responses. The damage viscoelastic model, based on Schapery's model, is employed in identifying the damage viscoelastic response and separating it from the viscoplastic response.

The developed experimental program and theoretical framework were used to analyze repeated creep tests conducted on three mixes that include aggregates with different characteristics.

INTRODUCTION

Researchers have adopted different models to describe the HMA response, and followed different experimental approaches to determine the models' parameters. Park et

al. (1996) used a uniaxial tension test under different strain rates at a temperature of 25 °C to evaluate the parameters of a viscoelastic continuum damage model. Lee and Kim (1998) used tensile uniaxial cyclic tests in controlled-strain mode at different strain amplitudes to determine their damage viscoelastic model's parameters. Scarpas et al. (1997) used monotonic compression and tension tests coupled with incremental creep tests at temperatures ranging between 10 °C and 40 °C in order to extract the parameters of a damage elasto-viscoplastic model.

Chehab et al. (2003) developed a damaged viscoelastic relationship to characterize the elastic and viscoelastic responses and a viscoplastic relationship to characterize the plastic and viscoplastic responses. The viscoelastic model is based on Schapery's continuum damage approach. The developed viscoplastic model is based on a one-dimensional relationship proposed by Uzan (1996). They used dynamic testing at small strains to model and characterize the linear viscoelastic response. They also used monotonic tests at relatively low temperatures to determine the damage viscoelastic response. The predicted damage viscoelastic strain was then subtracted from the total strain measured using constant cross head rate tests in uniaxial tension at temperatures of -30 °C to 40 °C to model the viscoplastic component of the strain. The experimental measurements presented by Chehab et al. (2003) were all conducted using tension tests.

Schwartz et al. (2004) adopted the same model as Chehab et al. (2003), but they conducted compression uniaxial and triaxial tests. Schwartz et al. (2004) used uniform time and uniform load creep and recovery tests, at temperatures ranging from 25 °C to 45 °C, to extract their viscoplastic model parameters. The viscoplastic strains were

determined from the recovery period after each loading cycle from both series of uniform time and uniform load. Both Chehab et al. (2003) and Schwartz et al. (2004) showed that HMA is a thermologically simple material even at high viscoplastic strains at high temperatures.

OBJECTIVES

Many researchers have been working on modeling the response of HMA. The response of HMA consists of four components namely elastic, plastic, viscoelastic, and viscoplastic. Decomposition and quantification of these responses for HMA is the main purpose of this chapter. Once these responses are identified, constitutive models can be developed to describe them. The objective of this chapter is to develop and perform an experimental program that is capable of decomposition and identification of the constitutive HMA response.

MIX DESIGN AND MATERIALS PROPERTIES

Mix Design

Four-inch diameter (101.6 mm) HMA specimens of three mixes with different aggregate types were compacted using a Servo Pac gyratory compactor to a target air void content of 7.0 %. The three aggregate types were gravel, limestone, and granite. These aggregate types were selected because they represent a wide range of aggregate properties. Mix volumetrics and laboratory data of these three mixes are tabulated in Table 3.1. All three mixes were prepared according to the Superpave specifications for high traffic roads

(10 to 30 million equivalent single axle loads (ESAL's). Fig. 3.1 shows the gradations of the aggregates used in the three mixes.

Table 3.1. Mix Design Factors for the Three Mixes

Mix	**Gravel**	**Limestone**	**Granite**
Avg. Measured Air void, %	7.04	6.7	6.89
SD of AV	0.48	0.25	0.30
Binder Type	PG 64-22	PG 64-22	PG 64-22
Binder Content, %	3.6	4.85	4.86
Maximum Specific Gravity	2.484	2.47	2.471
Specimen Height, mm	155	157.5	157.5
Sieve Size, mm	**Percent Passing**		
12.5	100	98.8	98.8
9.5	91.748	79.5	79.5
4.75	48.22	46.2	46.2
2.36	32.71	31.6	31.6
1.18	27.96	24.5	24.5
0.6	22.26	17.8	17.8
0.3	9.75	11.2	11.2
0.15	3.94	6.3	6.3
0.075	2.95	1.5	1.5
Pan	0	0	0

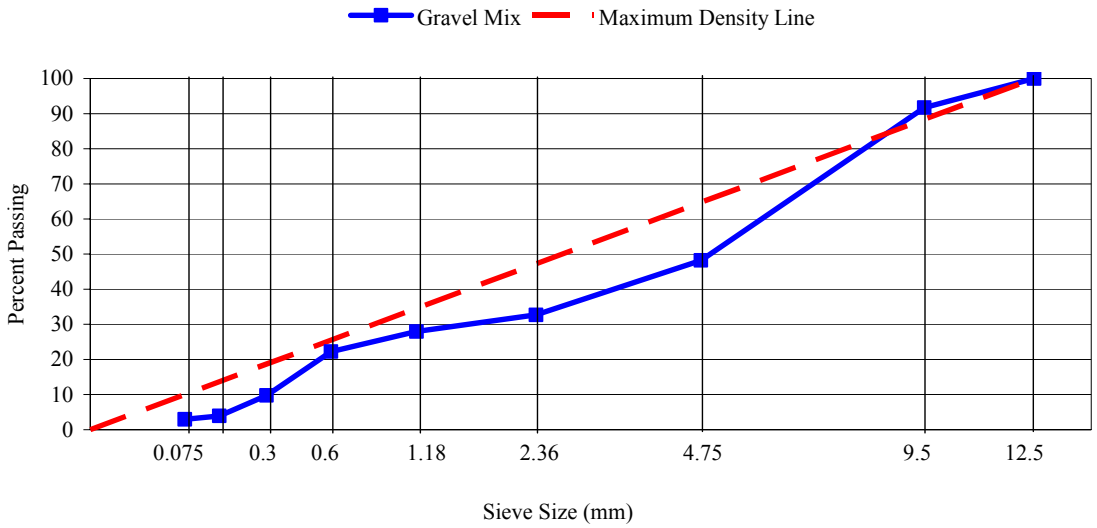

A) Gravel Mix

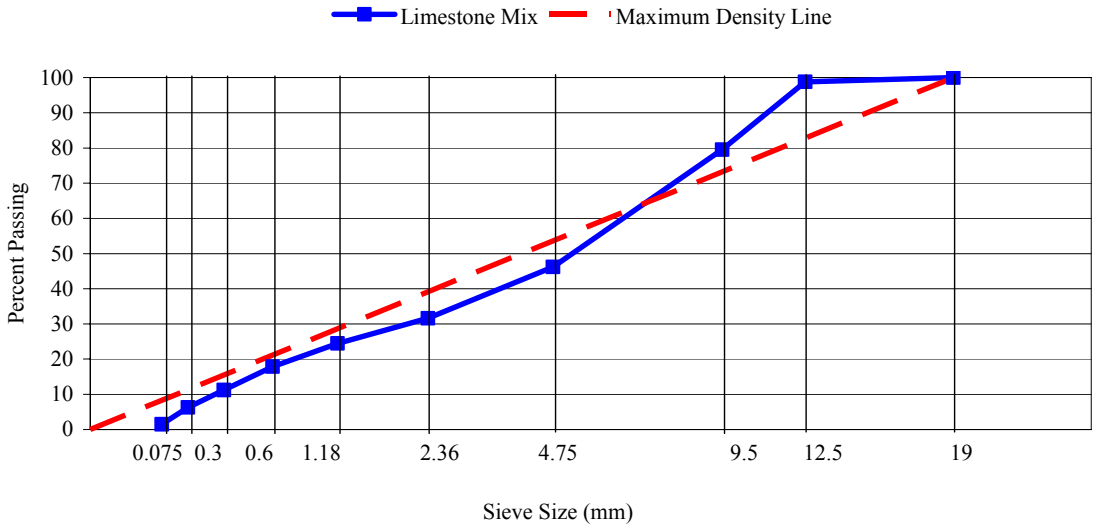

B) Limestone Mix

Fig. 3.1. 0.45 Power Gradation Charts of the Three Mixes A) Gravel, B) Limestone, and C) Granite

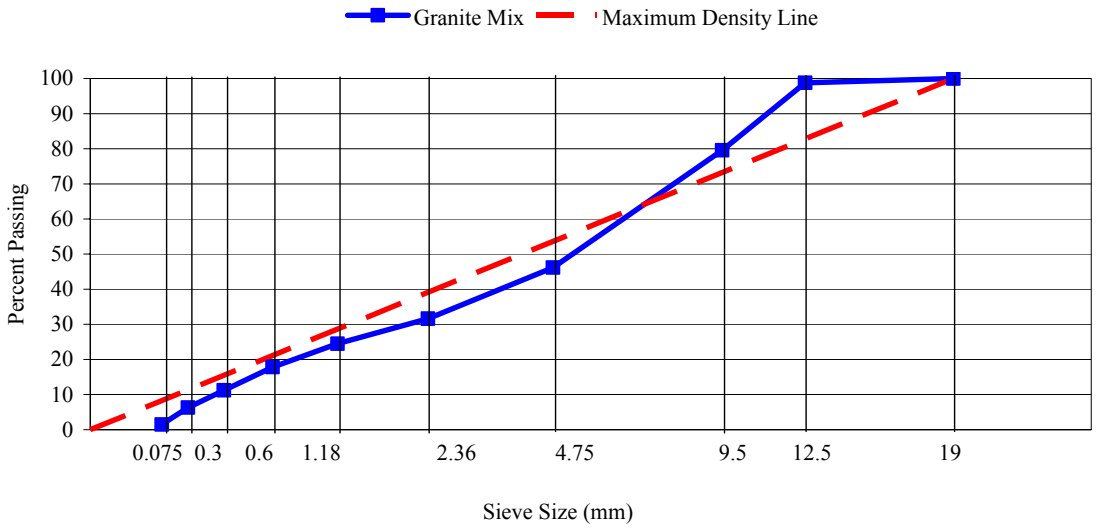

C) Granite Mix

Fig. 3.1. Continued

Material Properties

The shape characteristics of the three aggregates used in this study were characterized by Masad et al. (2005). Aggregate images were captured using the Aggregate Imaging System (AIMS) that was developed to capture images of both fine and coarse aggregate (Masad 2003). AIMS uses eigenvector analysis to identify the longest and shortest dimensions of a black and white image of a particle projection. It is also capable of measuring the depth of a particle. The three lengths are used to calculate the sphericity index (SP), which is a measure of the particle form as follows:

$$Sphericity\ \ Index = \sqrt[3]{\frac{d_S \cdot d_I}{d_L^2}} \qquad (3\text{-}1)$$

where d_L is the longest dimension, d_I is the intermediate dimension, and d_S is the shortest dimension. The sphericity values for coarse aggregates are shown in Table 3.2. A particle with equal dimensions will have a sphericity value of 1.0.

AIMS also provides an angularity index which increases as particle angularity increases. Texture analysis is conducted on gray scale images using wavelet theory. The texture index increases with an increase in surface texture (Masad 2003).

The angularity and texture results are reported in Table 3.2. As reported by Masad et al. (2005), among the fine aggregates tested, the granite was the most angular while the uncrushed gravel was the least angular. Both fine limestone and granite possessed higher texture values compared to gravel, and the limestone aggregate had the highest texture values. Image analysis of coarse aggregates showed that the granite exhibited the highest angularity and texture levels, whereas the gravel had the lowest texture and angularity values. According to the sphericity results, limestone was the most elongated while gravel was the least elongated.

Table 3.2. Aggregate Shape Parameters

Type	Size	Angularity	Texture	Form (Sphericity)
Limestone	Fine	2652.38	192.00	N/A
	Coarse	3041.00	245.50	0.69
Gravel	Fine	2044.5	93.00	N/A
	Coarse	1936.26	150.00	0.78
Granite	Fine	4401.40	145.00	N/A
	Coarse	3347.32	422.00	0.71

ANISOTROPY OF HMA AGGREGATE STRUCTURE

The vector magnitude Δ introduced by Curray (1956) can be used for the purpose of quantifying the material anisotropy in terms of aggregate distribution within the microstructure:

$$\Delta = \frac{1}{M}\left[\left(\sum_{k=1}^{M}\cos 2\theta^{k}\right)^{2} + \left(\sum_{k=1}^{M}\sin 2\theta^{k}\right)^{2}\right]^{\frac{1}{2}} \tag{3-2}$$

where θ_k is the orientation of an individual aggregate on a two-dimensional image of HMA cut section ranging from -90^o to +90^o and M is the total number of aggregates analyzed in the image. Theoretically, the value of Δ ranges between zero and unity. Zero value indicates the aggregates are completely randomly distributed, which is analogous to isotropic materials, and a unity value indicates the aggregates are all oriented in one direction (Tashman 2003).

Aggregate structure anisotropy is included in the constitutive model through introducing a modified stress tensor ($\bar{\sigma}_{ij}$) that is as a function of stress tensor σ_{ij} and fabric tensor F_{ij} as shown in Eq. (3-3) (Tobita and Yanagisawa 1988, Masad et al. 2003):

$$\bar{\sigma}_{ij} = \frac{3}{2}\left[\sigma_{ik}F_{kj} + F_{ik}\sigma_{kj}\right] \tag{3-3}$$

The anisotropic tensor F_{ij} is a function of Δ, which is measured using image analysis of two-dimensional vertical sections of HMA specimens. The Δ value in HMA was found to vary between zero and 0.5 for HMA (Masad et al. 1999, Tashman 2003). Accordingly, the deviatoric stress in a triaxial creep test is modified as

in Eq. (3-4) to account for the aggregate distribution as follows:

$$\overline{\sigma} = \overline{\sigma_1} - \overline{\sigma_3} \tag{3-4}$$

$$\overline{\sigma_1} = \frac{3\sigma_1(1-\Delta)}{3+\Delta} \tag{3-5}$$

$$\overline{\sigma_3} = \frac{3\sigma_3(1+\Delta)}{3+\Delta} \tag{3-6}$$

where σ_1 is the axial creep stress and σ_3 is the associated creep confinement. In essence, the applied stress is replaced with a modified stress tensor that reflects the effect of anisotropic distribution of aggregate structure on the anisotropic mechanical response (Masad et al. 2005). As will be shown in this chapter and the following chapter, this approach simplifies the procedure to account for anisotropy in the constitutive model.

EXPERIMENTS TO IDENTIFY STRAIN COMPONENTS

The strain components as described earlier in Chapter II are defined as:

$$\varepsilon = \varepsilon^e + \varepsilon^{ve} + \varepsilon^p + \varepsilon^{vp} \tag{3-7}$$

where ε is the total strain; ε^e is the elastic strain, which is recoverable and time-independent; ε^{ve} is the viscoelastic strain, which is recoverable and time-dependent; ε^p is the plastic strain, which is irrecoverable and time-independent; and ε^{vp} is the viscoplastic strain, which is irrecoverable and time-dependent. In creep test the elastic component is defined by setting a time limit that would identify the difference between the elastic and viscoelastic components. This time limit varies with the type of the material and it is

controlled by the accuracy of the measuring devices and usually identified based on the experimental results. Therefore, motivated by practicality and for the sake of simplicity, recoverable components (elastic and viscoelastic) will be referred to herein as viscoelastic response. Similarly, the irrecoverable components (plastic and viscoplastic) will be combined and referred to as a viscoplastic component. This approach has already been adopted in several studies in the past (Abdulshafi and Majidzadeh 1984, Bonnier 1993, Chehab et al. 2003, Schwartz et al. 2004).

In this chapter the damage viscoelastic strain, ε^{dve}, will be identified by first measuring the linear viscoelastic response. Then, damaged viscoelasticity theory will be employed to characterize the damage parameters. Once ε^{dve} is identified, it can be subtracted from the total strain to quantify the viscoplastic strain. Accordingly, the components of the strain in this study are governed by the following equation:

$$\varepsilon = \varepsilon^{dve} + \varepsilon^{vp} \tag{3-8}$$

Linear Viscoelastic Response

The linear viscoelastic response is quantified by performing a dynamic frequency sweep compression test. The data were analyzed to solve for the creep compliance, which describes the linear viscoelastic behavior of HMA.

HMA specimens were tested using frequency sweep dynamic compression tests at five different frequencies and one temperature (130 °F). The dynamic testing was performed in stress-controlled mode that would generate peak-to-peak strain ranging between 50 and 150 microstrains with no confinement. At this strain level, HMA is

typically assumed to exhibit linear viscoelastic response (Chehab et al. 2003). Two replicates from each of the gravel, limestone, and granite were tested. Table 3.3 presents the loads applied on each of the mixes.

Table 3.3. Dynamic Testing Loads for Each Mix

	Granite	Limestone	Gravel
Frequency, Hz	Load, lb		
25	900	900	500
10	800	800	450
5	600	600	350
1	350	350	175
0.5	300	300	150
0.1	250	250	125

The procedure described in National Cooperative Highway Research Program (NCHRP) 9-19 was followed in performing this test (Witczak and Pellinen 2000). The equations used for fitting the stress and strain functions have the following forms, respectively:

$$\sigma(t) = \sigma_o + \sigma_1 \sin(2\pi f t) \tag{3-9}$$

$$\varepsilon(t) = \varepsilon_o + \varepsilon_1 \sin(2\pi f t - \delta) \tag{3-10}$$

where σ_o and ε_o are the peak-to-peak stress and strain added to the bedding stress and strain, σ_1 and ε_1 are peak-to-peak stress and strain, respectively, f is the frequency of loading in Hz, t is time, and δ is the phase angle in radians.

After fitting the data to these functions, the dynamic creep compliance and the phase angle were calculated as follows:

$$\left|D^*\right| = \frac{\varepsilon_1}{\bar{\sigma}_1} = \frac{(3+\Delta)\,\varepsilon_1}{3(1-\Delta)\,\sigma_1} \tag{3-11}$$

$$\delta = \omega\,\Delta t \tag{3-12}$$

The above two properties were calculated at each frequency for the two replicates. Then the average compliance and average phase angle were calculated for each mix. The result from applying the dynamic compression test on the granite mix is shown in Table 3.4. To keep the notations simple, the symbol "$\left|\ \right|$" around the creep compliance was removed.

Table 3.4. Dynamic Compression Results for Granite Mix

Frequency	$\left\|D^*\right\|$	δ
Hz	1/ psi	Degrees
25	1.08E-06	56
10	3.42E-06	49
5	8.55E-06	48
1	1.22E-05	53
0.5	1.29E-05	34
0.1	1.20E-05	29

The creep compliance and the phase angle values of the three mixes are presented in the Fig. 3.2. One of the performance parameters recommended by NCHRP

9-19, E*/sin δ, is calculated and graphed in Fig. 3.3. However, it should be kept in mind the E^* parameter presented here differs from the typical modulus, and the one used here accounts for material anisotropy. The E*/sin δ parameter ranks the mixes in descending order as limestone, gravel, and then granite. It can be seen that the difference between the gravel and granite mixes is insignificant. These results do not agree with the shape characteristics in Table 3.2 that show granite to exhibit more angularity and texture than gravel. As such, granite is expected to have much better resistance to permanent deformation than the gravel mix. The superior resistance of the granite mix to permanent deformation compared with the gravel mix will be supported later with the permanent deformation measurements from the creep and recovery tests. Consequently, the viscoelastic parameter E*/sin δ failed to rank the three mixes in terms of their resistance to permanent deformation. This might be due to the reliance of this parameter on energy dissipated in viscoelastic deformation, while as will be shown later, the viscoelastic response is small compared to the damage viscoelastic response and viscoplastic response at the test temperature.

In order to determine the creep compliance D(t) as a function of time from the dynamic creep compliance as a function of frequency, three different methods were used. The first is according to the procedure by Schapery as documented by Chehab et al. (2003), the second is an interconversion relationship for linear viscoelastic functions (Ferry 1980), and the third is by using the phenomenological theory of linear viscoelastic behavior (Tschoegl 1989).

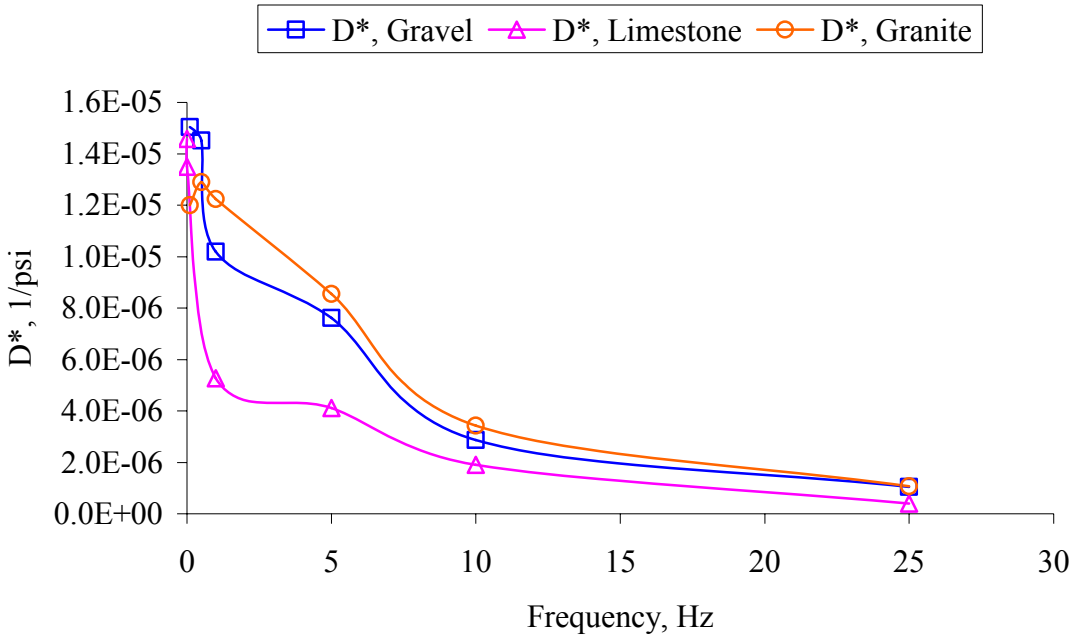

A)

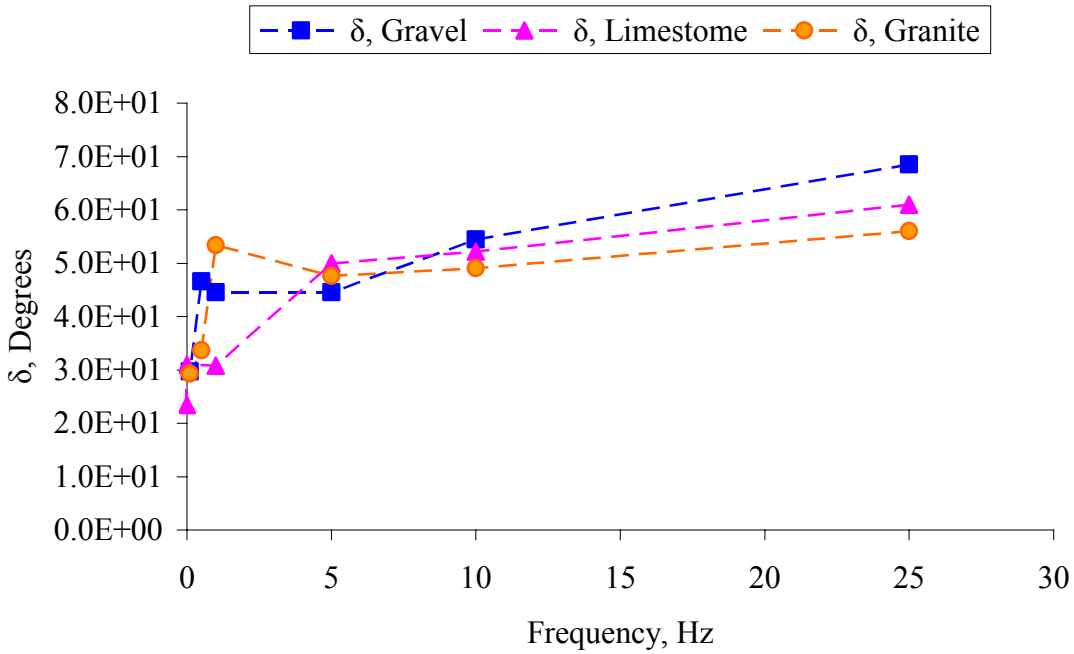

B)

Fig. 3.2. A) Creep Compliance and B) Phase Angle for the Three Mixes

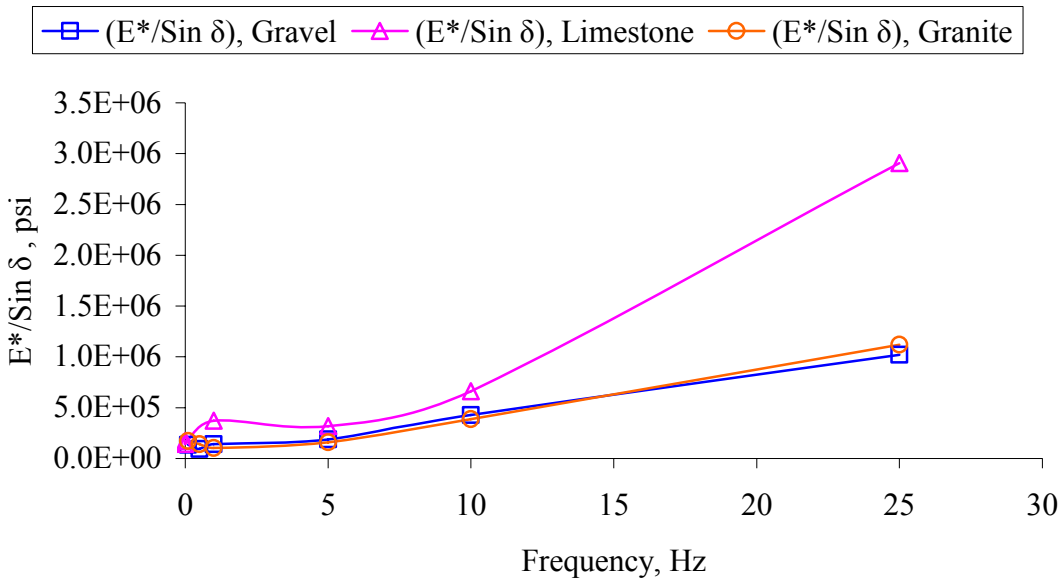

Fig. 3.3. Linear Viscoelastic Parameter, E*/Sin δ, for the Three Mixes

Chehab et al. (2003) followed Eq. (3-13) to convert the dynamic relaxation modulus to relaxation modulus as a function of time:

$$E(t) \cong \frac{1}{\lambda} E(f)\Big|_{f=\frac{1}{t}} \tag{3-13}$$

where

$$\lambda = \Gamma(1 - n)\cos(n\pi/2) \tag{3-14}$$

Γ is the Gamma function, n is the log-log slope of the dynamic modulus-frequency relationship:

$$n = \frac{d \log E(f)}{d \log f} \tag{3-15}$$

Now that the relaxation modulus is determined it can be fitted to a Prony series,

$$E(t) = E_{\infty} + \sum_{m=1}^{M} E_m e^{-t/\rho_m} \tag{3-16}$$

where E_{∞}, ρ_m, and E_m are long-time equilibrium modulus, relaxation time, and regression coefficient of Prony series, respectively. Then, the relaxation modulus can be converted to creep compliance by using the relation in Eq. (3-17):

$$E(t)D(t) = \frac{\sin n\pi}{n\pi} \tag{3-17}$$

from which the creep compliance is obtained and fitted to a Prony series in the form:

$$D(t) = D_0 + \sum_{m=1}^{M} D_m \left[1 - e^{-t/\tau_m}\right] \tag{3-18}$$

where τ_m is the retardation time, D_m is the regression coefficient, and D_0 is the initial creep compliance at time zero.

The second method used is an interconversion relationship which has the following form (Ferry 1980):

$$D(t) = D'(\omega) + 0.4\,D''(0.4\,\omega) - 0.014 D''(10\omega)\Big|_{\omega=\frac{1}{t}} \tag{3-19}$$

where

$$D'(\omega) = D^*(\omega)\cos\delta \tag{3-20}$$

$$D''(\omega) = D^*(\omega)\sin\delta \tag{3-21}$$

where ω is the frequency in radians. The creep compliance is then fitted to a Prony series as in Eq. (3-18).

The third method to convert D^* to $D(t)$ uses the phenomenological theory of linear viscoelastic behavior (Tschoegl 1989). In this method, the storage and loss components of

the dynamic creep compliance are fitted to Eqs. (3-22 and 3-23) that represent the Generalized Maxwell model (generalized Prony series):

$$D'(w) = D_0 + \sum_{m=1}^{M} \frac{D_m}{1 + w^2 \tau_m^2} \tag{3-22}$$

$$D''(w) = \sum_{m=1}^{M} \frac{D_m w \tau_m}{1 + w^2 \tau_m^2} \tag{3-23}$$

where D_0, D_m, and τ_m are material constants and w is the frequency in radians/ sec. These parameters were used to determine the creep compliance as described by the Prony series in Eq. (3-18).

The three methods were applied to the three mixes and Fig. 3.4 presents the creep compliance from the three methods.

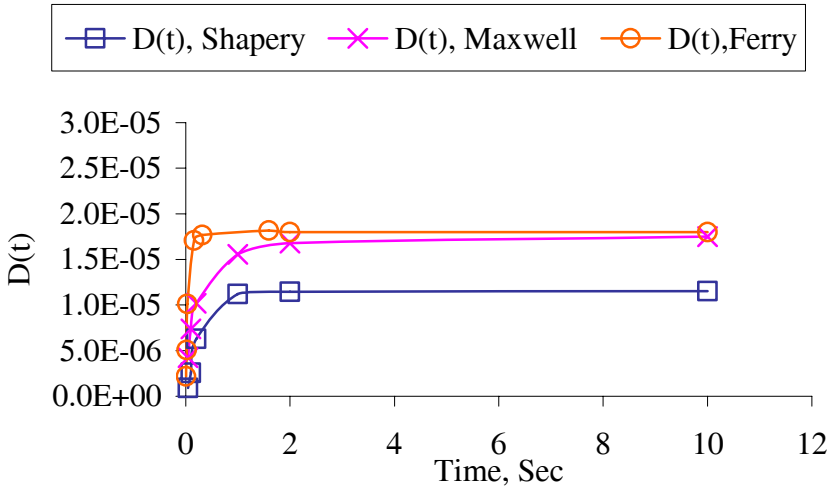

A) Gravel Mix

Fig. 3.4. Creep Compliance for A) Gravel, B) Limestone, and C) Granite Mixes

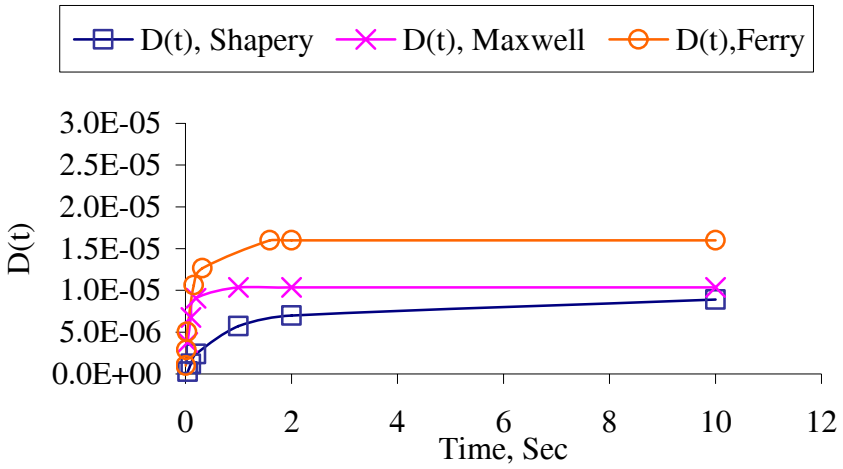

B) Limestone Mix

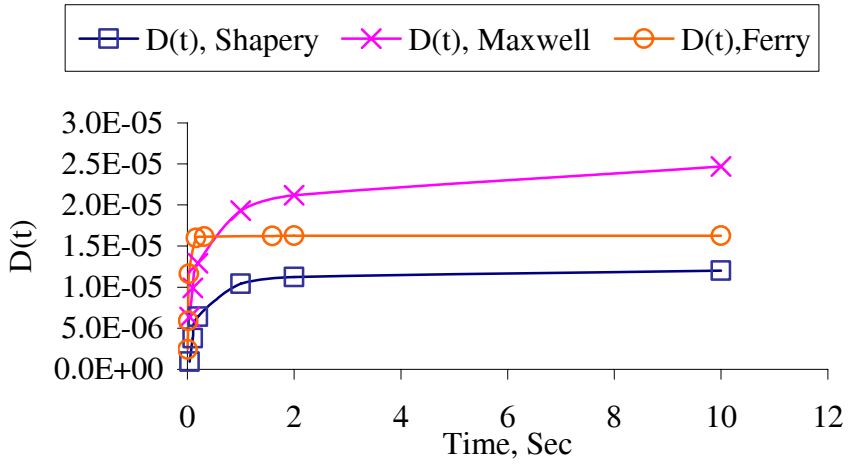

C) Granite Mix

Fig. 3.4. Continued

It can be seen that the compliance calculated from the phenomenological theory of linear viscoelastic behavior, Eqs. (3.22 and 3.23) and the interconversion among linear viscoelastic functions, Eq. (3-19), are closer to each other from Eq. (3-13). It is interesting to note that the linear viscoelastic properties in Fig. 3.4 were not sensitive to aggregate type

used in mixes. This can be attributed to the low strain amplitudes applied in these tests. The Prony series coefficients for the three mixes based on Ferry's (1980) equation are presented in Tables 3.5 to 3.7.

Table 3.5. Prony Series Coefficients for Gravel Mix by Ferry (1980)

Prony series coefficients for Gravel by Ferry's (1980)			
D_0	-9.95E-07		
D_1	3.29E-03	τ_1	6.58E-02
D_2	-1.88E-03	τ_2	6.59E-02
D_3	8.72E-04	τ_3	6.35E-02
D_4	8.72E-04	τ_4	6.35E-02
D_5	3.35E-04	τ_5	5.22E-02
D_6	-1.88E-03	τ_6	6.59E-02
D_7	-5.28E-04	τ_7	6.04E-02
D_8	-5.28E-04	τ_8	6.04E-02
D_9	-5.28E-04	τ_9	6.04E-02

Table 3.6. Prony Series Coefficients for Limestone Mix by Ferry (1980)

Prony series coefficients for Limestone by Ferry's (1980)			
D_0	-3.11E-07		
D_1	7.89E-06	τ_1	4.34E-02
D_2	9.69E-03	τ_2	1.49E-01
D_3	-5.55E-04	τ_3	1.31E-01
D_4	5.81E-03	τ_4	1.52E-01
D_5	-4.51E-03	τ_5	1.43E-01
D_6	-5.17E-03	τ_6	1.50E-01
D_7	5.62E-04	τ_7	1.49E-01
D_8	1.14E-02	τ_8	1.43E-01
D_9	-1.72E-02	τ_9	1.48E-01

Table 3.7. Prony Series Coefficients for Granite Mix by Ferry (1980)

Prony series coefficients for Granite by Ferry's (1980)			
D_0	-1.66E-06		
D_1	4.71E-03	τ_1	6.57E-02
D_2	-2.03E-03	τ_2	6.65E-02
D_3	6.69E-04	τ_3	6.32E-02
D_4	6.69E-04	τ_4	6.32E-02
D_5	5.18E-04	τ_5	5.13E-02
D_6	-2.03E-03	τ_6	6.65E-02
D_7	-8.27E-04	τ_7	6.03E-02
D_8	-8.27E-04	τ_8	6.03E-02
D_9	-8.27E-04	τ_9	6.03E-02

Experimental Setup to Identify Damage Viscoelastic and Viscoplastic Responses

Repeated creep tests were conducted to characterize the damage viscoelastic and viscoplastic responses. This test was selected as it allows for the separation of the different responses. The testing included three confinement levels of 0, 15, and 30 psi, three levels of axial loading for each confinement, and two replicates for each stress level. The main considerations in the development of the testing program were to:

1) Select multiple stress levels such that some of stress levels cause hardening only while other levels cause damage. This is considered important in order to determine the hardening and damage parameters of the model presented in the following chapter.

2) Reach maximum strain during loading within each cycle (strain rate is almost zero). This condition is necessary to capture all the plastic strain in each cycle, and to facilitate the determination of the viscoplastic model parameters.

3) Use stress levels that are equal or at least close in values in loading all materials.

It was a challenge to achieve all the above three factors given the difference in materials in strength and response to different loading rates. Preliminary testing was conducted to determine the appropriate stress levels for each mix. Since the gravel mix had the least strength, it was considered the limiting case, and it was used to determine the appropriate stress levels. The load was chosen such that the mixes would reach similar strain levels after about 15 cycles in favor of reducing the testing time. Table 3.8 presents a breakdown of the creep tests performed on the gravel mix. Similar testing but different deviatoric stresses were performed for the granite and limestone mixes.

All experiments were performed at a temperature of 130 °F (58 °C). Dual lubricated latex sheets were used to minimize the end effect at the bottom and top of the specimen. Two vertical linear variable differential transformers (LVDT's) were fixed 180° apart to measure the vertical deformation with a vertical gage length of 3 in. Radial deformation was measured using a radial LVDT that was fixed around the specimen's circumference. The LVDT is capable of measuring deformations of up to 4 mm. This corresponded to an axial strain of about 1.5%, after which there was no experimental measurements of the radial deformation. A load cell of 5 kip capacity was used to measure the applied loads.

Figs. 3.5 to 3.7 present the experimental results of the repeated creep tests for the three mixes at 0, 15, and 30 psi confinements and three stress levels. The tests show that some stress levels went through hardening (reduction is strain rate with an increase in number of cycles), while other tests exhibited damage (increase in strain rate). Most of the

tests reached the maximum strain (strain rate = 0) within each cycle during the hardening behavior. As will be discussed later, this condition facilitated capturing the viscoplastic strain and determining the models parameters.

By examining Figs. 3.5 to 3.7 it can be seen that at zero confinement the gravel mix needed lower stress levels in order to develop comparable strain levels to the other two mixes. The difference is stress levels among the three mixes decreased in the confined tests.

Table 3.8. Breakdown of Creep Tests for the Gravel Mix

	Compression		
Confinement, psi	0	15	30
Specimen	00A	15A	30A
Deviatoric Stress, psi	71	471	982
Specimen	00B	15B	30B
Deviatoric Stress, psi	55	393	884
Specimen	00C	15C	30C
Deviatoric Stress, psi	39	314	785

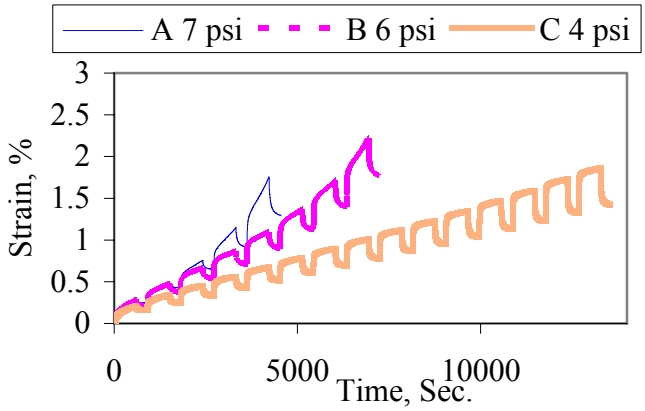

A) 0 psi

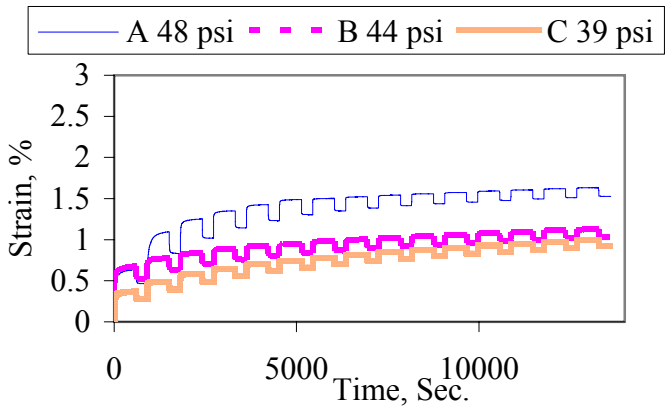

B) 15 psi

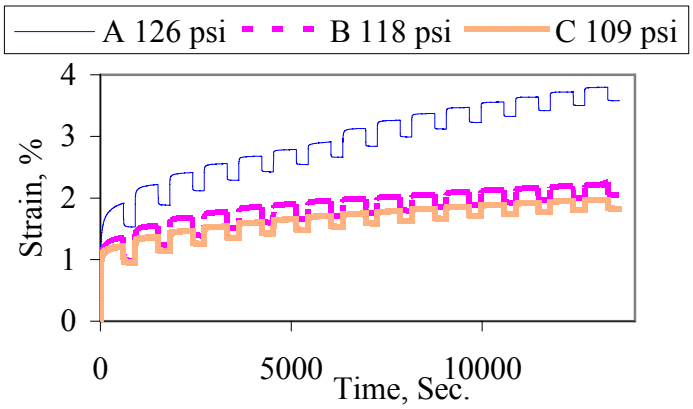

C) 30 psi

Fig. 3.5. Repeated Creep Test Results on Gravel Mix at A) 0, B) 15, and C) 30 psi Confinement

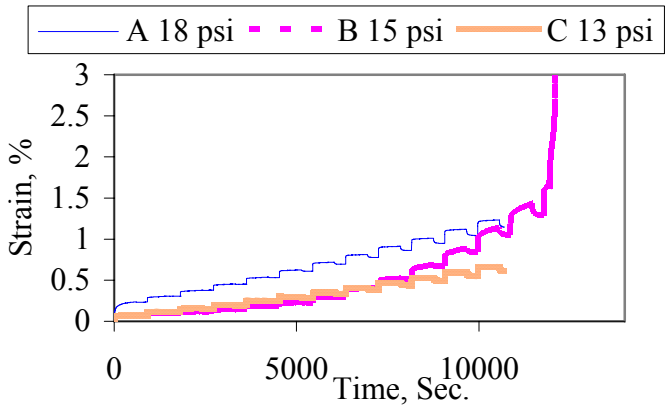

A) 0 psi

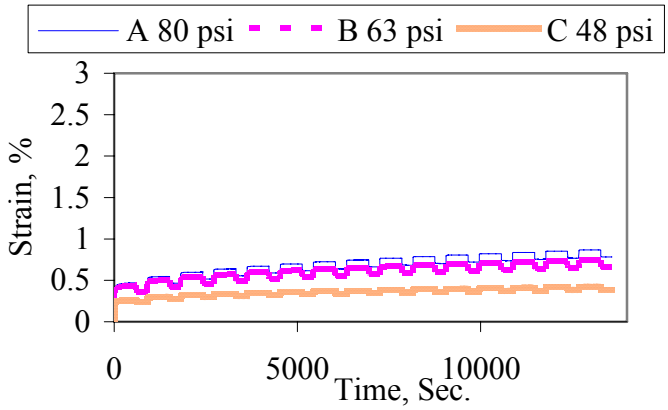

B) 15 psi

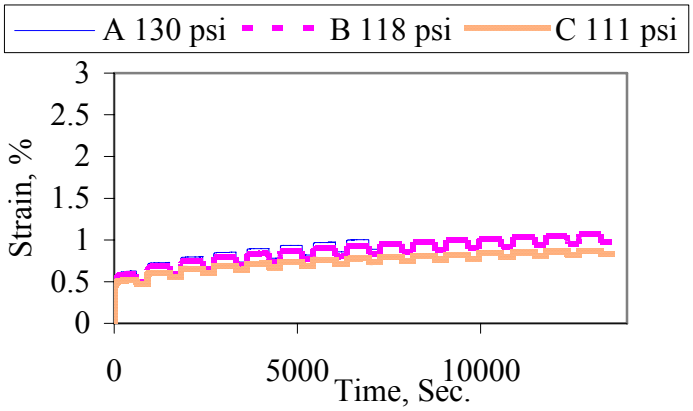

C) 30 psi

Fig. 3.6. Repeated Creep Test Results on Limestone Mix at A) 0, B) 15, and C) 30 psi Confinement

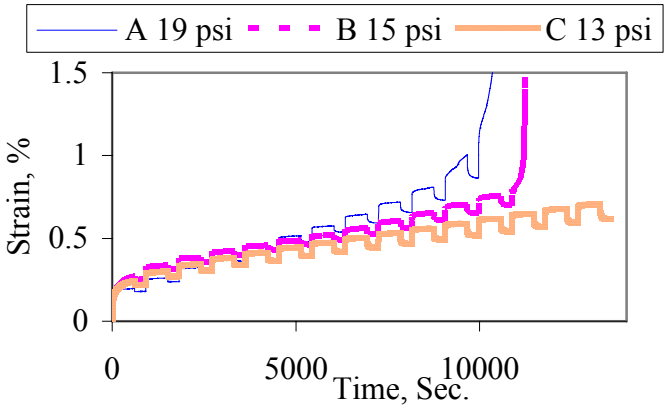

A) 0 psi

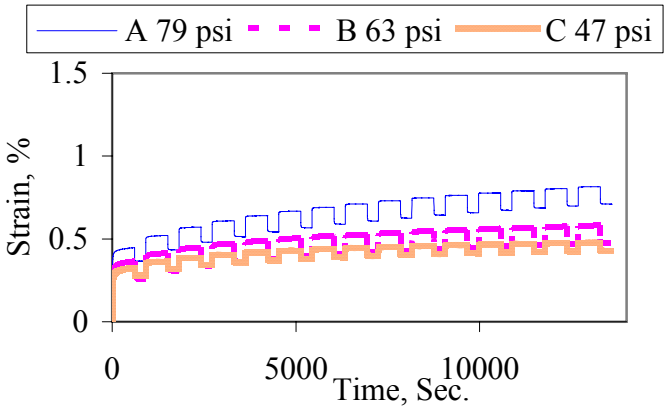

B) 15 psi

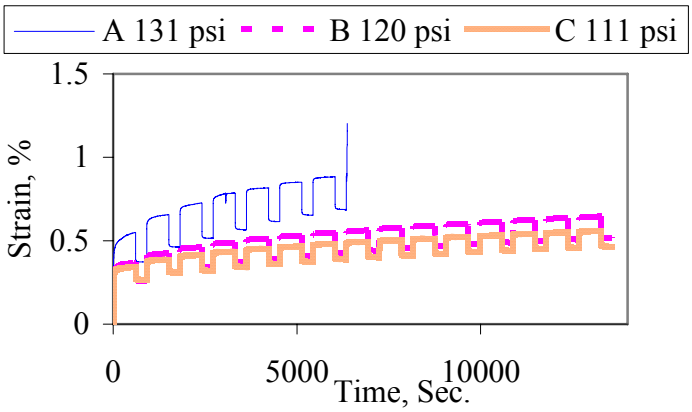

C) 30 psi

Fig. 3.7. Repeated Creep Test Results on Granite Mix at A) 0, B) 15, and C) 30 psi Confinement

One important factor that needs to be considered is the effect of the unloading time (t_1 in Fig. 3.8) on the decomposition of the damage viscoelastic (DVE) and viscoplastic (VP) strain components. Viscoplastic strain increases as a function of time causing permanent changes in the internal structure. Therefore, it is expected that the unloading response will depend on the time t_1 at which the material is unloaded. This raises the concern that the viscoelastic response might not be unique, as it depends on the viscoplastic strain accumulating at t_1. Consequently, it was decided to establish a criterion for t_1, which is the time at which the strain reaches or very close to a "saturation" limit. This saturation limit is defined in this study for a strain rate less than $5\ 10^{-05}$ %/Sec. The preliminary testing conducted in this study showed that a loading time of 10 minutes and unloading time of 5 minutes could achieve this criterion for most of the test specimens within the hardening behavior.

STRAIN DECOMPOSITION APPROACH

Theoretical Framework

It is important to conduct the strain decomposition within theoretical framework. Such a framework is needed to understand the influence of the strain decomposition on the model development and to clearly link the assumptions employed in the decomposition to the model response. To this end, a constitutive model for damage viscoelasticity model is introduced for the purpose of decomposing the total strain to its damage viscoelastic and viscoplastic components.

For a linear viscoelastic material under a constant deviatoric stress, the

compliance can be calculated as:

$$D(t) = \frac{\varepsilon^{dve}(t)}{\overline{\sigma}} \tag{3-24}$$

Solving for strain, the equation is rearranged as follows:

$$\varepsilon^{dve}(t) = D(t)\overline{\sigma} \tag{3-25}$$

where

$$D(t) = D_o + \Delta D(t) \tag{3-26}$$

$\Delta D(t)$ is the transient component of the compliance, and D_o is the initial value of the compliance.

The damage viscoelastic response developed by Schapery (1969) can be described as in Eq. (3-27):

$$\varepsilon^{dve}(t) = g_o D_o \overline{\sigma} + g_1 \int_0^t D(\psi - \psi') \frac{dg_2 \overline{\sigma}}{d\tau} d\tau \tag{3-27}$$

where

$$\psi = \int_0^t dt' / a_\sigma[\overline{\sigma}(t')] \ (a_\sigma > 0) \tag{3-28}$$

$$\psi' = \psi(\tau) = \int_0^\tau dt' / a_\sigma[\overline{\sigma}(t')] \tag{3-29}$$

$g_o, g_1, g_2,$ and a_σ are material constants. g_o, g_1, g_2 are nonlinear or damage parameters, and a_σ is a time-temperature shift factor, and it is considered by Schapery (1969) to include the effect of confinement. The distinction between nonlinear and damage viscoelastic behaviors is discussed in the following chapter.

The nonlinear or damage creep compliance can be calculated as follows:

$$D_n = \frac{\varepsilon^{dve}(t)}{\overline{\sigma}} = g_0 D_0 + g_1 g_2 D\left(\frac{t}{a_\sigma}\right) \tag{3-30}$$

As all tests were performed at one temperature, so a_σ is not influenced by temperature in these tests. The approach followed here differs slightly from that by Schapery (1969) by considering one parameter G_2 which equals to $\left(\frac{g_2}{a_\sigma}\right)$ that captures the influence of confinement a_σ and damage viscoelasticity g_2. As the elastic response has already been included in the viscoelastic component, the first term in the equation vanishes and Eq. (3-30) reduces to:

$$\frac{\varepsilon^{dve}(t)}{\overline{\sigma}} = g_1 G_2 D(t) \tag{3-31}$$

Now we can evaluate the terms ε^{dve1} ,ε^{dve2}, and ε^{dve3} in Fig. 3.8, which illustrates a schematic of a creep test response:

$$\varepsilon^{dve3}(t) = G_2\left[D(t) - D(t-t_1)\right]\overline{\sigma} \tag{3-32}$$

$$\varepsilon^{dve1}(t) = g_1 G_2 D(t)\overline{\sigma} - g_1 G_2 D(t_1)\overline{\sigma} \tag{3-33}$$

$$\varepsilon^{dve2}(t) = g_1 G_2 D(t_1)\overline{\sigma} - G_2 D(t)\overline{\sigma} + G_2 D(t-t_1)\overline{\sigma} \tag{3-34}$$

$$\varepsilon^{dve1}(t) + \varepsilon^{dve2}(t) = g_1 G_2 D(t)\overline{\sigma} - G_2 D(t)\overline{\sigma} + G_2 D(t-t_1)\overline{\sigma} \tag{3-35}$$

$$\varepsilon^{dve}(t-t_1) = g_1 G_2 D(t-t_1)\overline{\sigma} \tag{3-36}$$

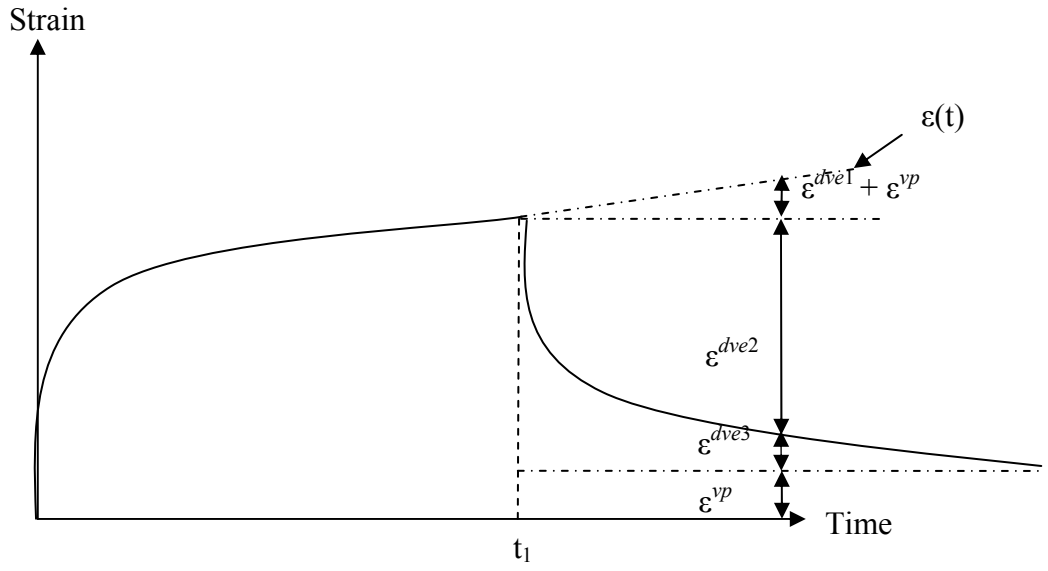

Fig. 3.8. Response to Creep Loading

In damaged viscoelastic materials, the loading part gives g_1 and G_2, as shown in Eq. (3-31), and the unloading part can be used to determine G_2 as shown in Eq. (3-32). However, in this experiment the loading part consists of both damaged viscoelastic and viscoplastic deformations. Hence, the loading portion cannot be used to determine the g_1. It was assumed in this study that g_1 is equal to unity. This assumption translates to assuming g_1 not to be a function of stress. This assumption makes it possible to use the unloading part to calculate G_2 given the creep compliance from the linear viscoelastic analysis. Once the G_2 value is determined, it can be used in Eq. (3-36) to calculate the damage viscoelastic part during loading. Consequently, damage viscoelastic part can also be determined as function of loading time by subtracting the damaged viscoelastic part from the total strain. Examples of the results are shown in Figs. 3.9 and 3.10.

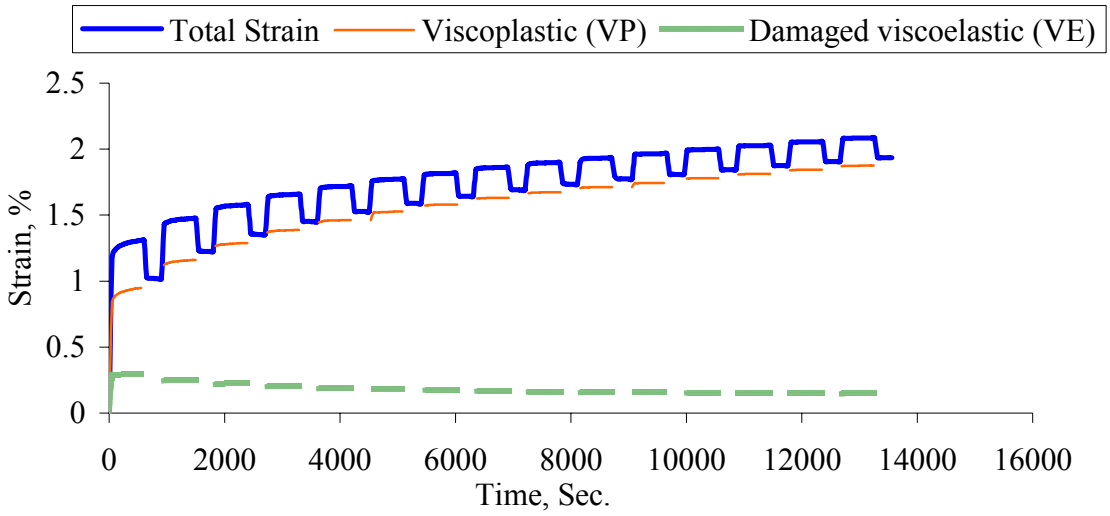

Fig. 3.9. Total, Viscoplastic, and Damaged Viscoelastic Strain at Low Stress Level Test

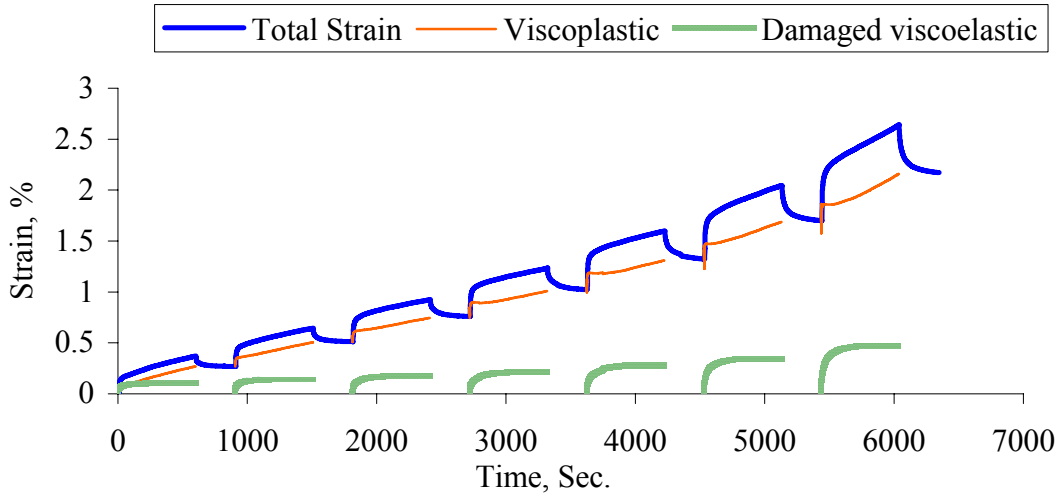

Fig. 3.10. Total, Viscoplastic, and Damaged Viscoelastic Strain at High Stress Level Test

Experimental Observations

Figs. 3.9 and 3.10 present a sample of the repeated creep tests at low and high stress levels with the strain response separated into its components. It is worth noticing that the behavior of the viscoelastic response has changed from low stress level to high stress level from a load cycle to another. The low stress showed that the viscoelastic response decreased with increasing number of cycles, which indicates that the material hardening phenomenon overcame the damage phenomenon. One the other hand, the high stress case showed that the viscoelastic response increased with increasing number of load cycles, which indicates that the material damage phenomenon overcame the hardening phenomenon.

The material response becomes unstable when damage evolution increases rapidly. The onset of unstable behavior should be identified in order to avoid using experimental measurements beyond this point in data analysis. The error beyond this point can be attributed to several factors, such as slippage of experimental devices, or loss of full contact between the specimen and the load cell. As such, the response beyond the failure point might not represent the global material behavior. Therefore, a graphical approach was implemented here to identify this point based on the work by Bhairampally et al. (2000).

As shown in the example results in Fig. 3.11A, the material experiences different behavior as the stress level increases. At low and medium stress levels the material hardening could overcome the damage evolution. On the other hand, at high stress level the material showed that the damage was overcoming the hardening occurring to the material. This behavior was verified using the graphical technique proposed by Bhairampally et al.

(2000) as shown in Fig. 3.11B. This technique relies on fitting a power function as shown in Eq. (3-37) to the accumulated permanent strain:

$$\ln\left\{\frac{\partial[\ln(\varepsilon^{vp})]}{\partial[\ln(n)]}\right\} = \ln(\beta\rho^{\beta}) - \beta \ln N \tag{3-37}$$

Bhairampally et al. (2000) suggested plotting the relationship shown in Fig. 3.11B to identify the damage development of an asphalt mix under repeated loading. A curvature reverse and positive slope of the function in Fig. 3.11B indicate that the material is in a tertiary creep state and the material is damaged. This technique is used to separate experiments in which hardening is overcoming the damage (which will be hereafter called hardening experiments) from others where the damage is overcoming the hardening (which will be hereafter called damage experiments). This information will be valuable in modeling the viscoplastic response as will be shown in the following chapter.

The effect of the repeated cycles compared to a single cycle creep test is presented in Fig. 3.12. It can be seen that the repeated loading generates more deformation compared with a single cycle creep test. This can be attributed to the differences in the microstructure in terms of aggregate orientation and air void size evolution between the two tests. Loading induces anisotropic aggregate distribution of particles where more contacts build up in the vertical direction, and particles' longest dimensions become more oriented in the horizontal direction.

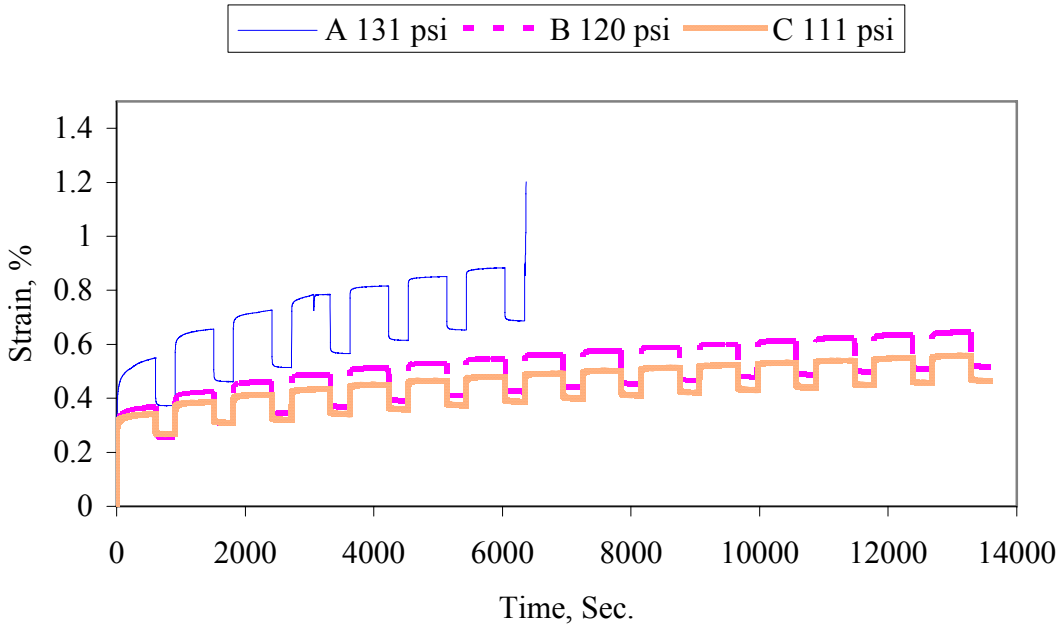

A)

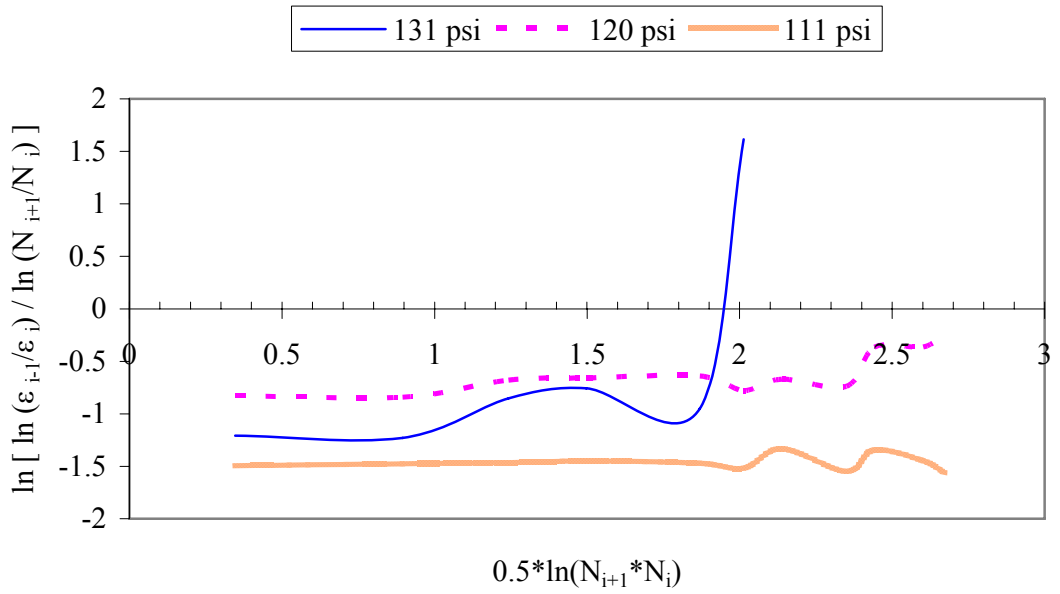

B)

Fig. 3.11. A) Sample Creep Test at Three Different Stress Levels, B) the Corresponding Damage Identification Technique Proposed

This distribution causes a specimen to be stiffer in the direction of the vertical load and assists in reducing deformation (Masad et al. 2005). However, unloading allows particles to "lose" some of the anisotropic distribution microstructure, reducing the stiffness in the vertical direction and promoting more permanent deformation. The reorientation of particles during unloading could also induce some damage (growth of air voids and cracks) that promotes more permanent deformation once load is reapplied.

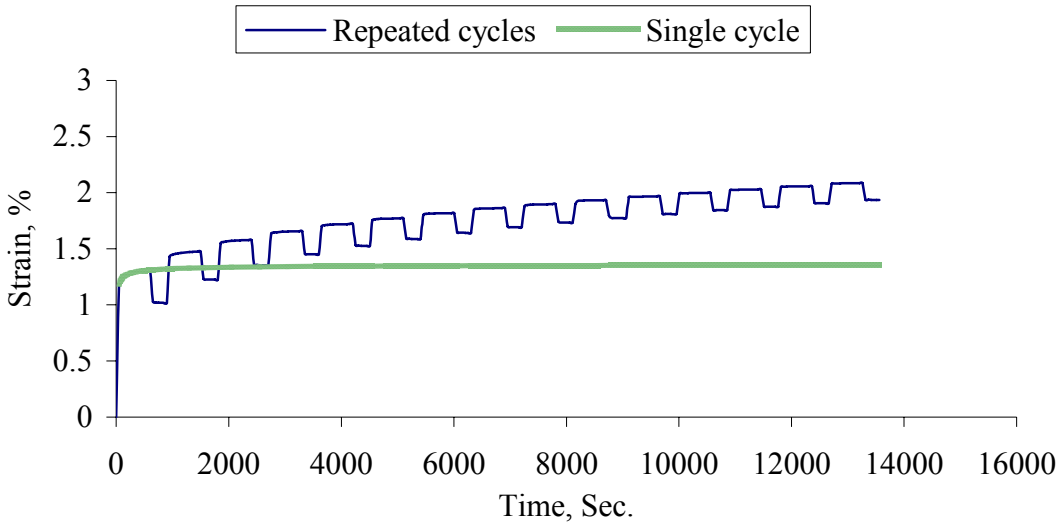

Fig. 3.12. Single Cycle and Repeated Cycles Total Creep Strain

CONCLUSIONS

This chapter presented an experimental approach within a theoretical framework to analyze the HMA response and calculate the damage viscoelastic and viscoplastic responses. The dynamic compression test was used to identify the material response at low

strain level, from which the linear viscoelastic response of the material was determined. The linear viscoelastic properties of the three mixes (gravel, granite, and limestone) were not consistent with the permanent strain measurements using repeated creep tests.

The repeated creep and recovery tests provided a precise response of the material at successive stages of loading and unloading. A damage viscoelasticity theory was employed to analyze the experimental measurements and calculate the damage viscoelastic parameters. This theory was used to calculate the damage viscoelastic response from the unloading response. Once the damage viscoelastic was identified, it was subtracted from the total strain during loading to calculate the viscoplastic strain as a function of loading time.

The damage viscoelastic response can be used as an indication of the material damage condition with increasing number of load cycles. A damage state was associated with an increase in the damage viscoelastic response with increasing number of load cycles, whereas hardening state was identified by a decrease or stabilization in the viscoelastic response with increasing number of load cycles.

CHAPTER IV

DETERMINATION OF DAMAGE VISCOELASTIC-VISCOPLASTIC MODEL PARAMETERS

OVERVIEW

This chapter presents the integration of a damage viscoelastic constitutive relationship with a viscoplastic relationship in order to develop a comprehensive anisotropic damage viscoelastic-viscoplastic model that is capable of capturing HMA response and performance under a wide range of temperatures, loading rates, and stress states. The damage viscoelasticity model developed by Schapery (1969) was used to present the viscoelastic response, and the viscoplasticity model developed at the Texas Transportation Institute (TTI) in the past few years was improved and used to model the viscoplastic and plastic components. The influence of the anisotropic aggregate distribution is accounted for in both the viscoelastic and viscoplastic responses. In addition, this chapter presents a methodology to determine the model's parameters using the repeated creep tests presented in Chapter III.

INTRODUCTION

Several approaches have been adopted for continuum constitutive modeling of HMA. Kim and Little (1990), Kim et al. (1997), and Si et al. (2002) are examples of studies on modeling HMA response using damage viscoelasticity. This approach relies on the characterization of the linear viscoelastic properties and energy dissipated in HMA damage. The linear viscoelastic properties are obtained using monotonic or cyclic tests

using small stress or strain loads that do not induce damage. Then, viscoelastic damage is measured through applying stresses or strains that are high enough to induce damage. This approach has mostly been employed in the characterization of HMA fatigue behavior.

Scarpas et al. (1997) presented a viscoplastic damage model based on Perzyna's formulation and Desai's yield surface to capture the macroscopic response of HMA under different loading conditions. Scarpas et al. (1997) used monotonic compression and tension tests coupled with incremental creep tests at temperatures ranging between 10 °C and 40 °C to determine the model's parameters.

Chehab et al. (2003) and Schwartz et al. (2004) developed a damage elasto-viscoplastic model for the characterization the HMA response at a wide range of temperatures (-30 °C to 40 °C). Chehab et al. (2003) used low-stress dynamic testing to determine the linear viscoelastic properties, constant head rate tests at low temperatures where viscoplastic strain is negligible to determine the damage viscoelastic parameters, and constant head rate tests at higher temperatures to determine the viscoplastic parameters. Schwartz et al. (2004) focused on using uniform time and uniform load creep and recovery tests, at temperatures ranging from 25 °C to 45 °C, to extract the viscoplastic model parameters. Both Chehab et al. (2003) and Schwartz et al. (2004) showed that HMA is a thermologically simple material even at high viscoplastic strains and high temperatures.

Recent efforts at the Texas Transportation Institute have focused on the development of comprehensive damage elasto-viscoplastic model (Tashman 2003, Dessouky 2005). This model was developed to account for the various factors associated with permanent deformation. These factors include friction between the aggregates coated

with binder and interlocking between aggregates, which are responsible for the dilation behavior of some mixes under shear stresses. The amount of dilation is dependent on the aggregate gradation, angularity, and form (flat-elongation) (e.g., Lytton et al. 1993, Sousa et al. 1993, Kaloush 2001). Another important factor that influences permanent deformation is bonding between the binder elements (cohesion) and between the binder and aggregates (adhesion). Microcracks and damage could be caused by stresses that exceed the cohesive and adhesive bonds in the mix. Lytton (2000) referred to microcracks associated with permanent deformation by stating "If an asphalt concrete work-hardens under repeated loads with accumulating plastic strain but does not have microcracks arresters and does not heal rapidly, it will reach a point at which it is stiff enough for microcracks to initiate and grow. This energy that is used up with each load is then parceled out to the growth of microcracks which soften the mix, and to increasing the rate of plastic strain."

OBJECTIVES

The objective of the research documented in this chapter is to further develop the TTI elasto-viscoplastic model. The new developments include:

1. Introducing an anisotropic damage viscoelastic-viscoplastic model. This is considered a major improvement as it allows the model to capture the response at low temperatures and high strain rates where damage viscoelasticity dominates the material response, and to capture the response at high temperature small strain rates where viscoplasticity is significant.

2. Accounting for the anisotropic behavior of the mix in both the viscoelastic and viscoplastic components.

3. Extracting the model's parameters from repeated creep tests, which allow the separation of viscoelastic deformation from viscoplastic deformation.

VISCOELASTIC MODEL

The model that is used to predict the viscoelastic properties is based on Schapery's (1969) theory as described in the previous chapter. The viscoelastic nonlinearity damage parameter G_2 is determined from Eq. (4-1), while g_1 is assumed to be equal to unity as discussed in Chapter III:

$$\varepsilon^{dve}(t-t_1) = g_1 G_2 D(t-t_1)\overline{\sigma} \tag{4-1}$$

where $D(t - t_1)$ is the viscoelastic compliance function determined from dynamic testing of HMA at small strain levels (see Fig. 3.4) and $\overline{\sigma}$ is the deviatoric stress that is modified to account for the material anisotropy (see Eq. [3-18]).

Fig. 4.1 presents the experimental results and the model prediction for the viscoelastic damage response of the three mixes at intermediate stress level and confinement of 30 psi. The results at the other confinement levels (15 psi and 30 psi) are presented in the Appendix. Eq. (4-1) was solved for each loading-unloading cycle to determine G_2. Fig. 4.2 presents example of G_2 values used to fit the model for the limestone mix at zero confinement. The fitting of the damage viscoelastic model to all experimental measured and the calculated G_2 are presented in the Appendix.

The G_2 results in the Appendix show some cases that G_2 increased with time while G_2 was almost constant in some other cases. An increase in G_2 value is an indication of damage. However, a G_2 value that stabilized with loading or reaches a constant value is an indication of nonlinear response without damage. Nonlinear response indicates the compliance from the creep test is different from that determined at small strain under dynamic loading. The constant G_2 clearly shows that the material did not experience damage that would change the microstructure, and G_2.

It is interesting to note that G_2 had a value less than 1 in some cases (see Fig. A. 8C). This can be explained by the linear viscoelastic response being a function of confinement. Recall that the linear viscoelastic compliance was determined with no confinement while some of the creep tests were conducted with confinement. Therefore, the G_2, or $\left(\frac{g_2}{a_\sigma}\right)$, less than one could be due to the effect of the a_σ parameter.

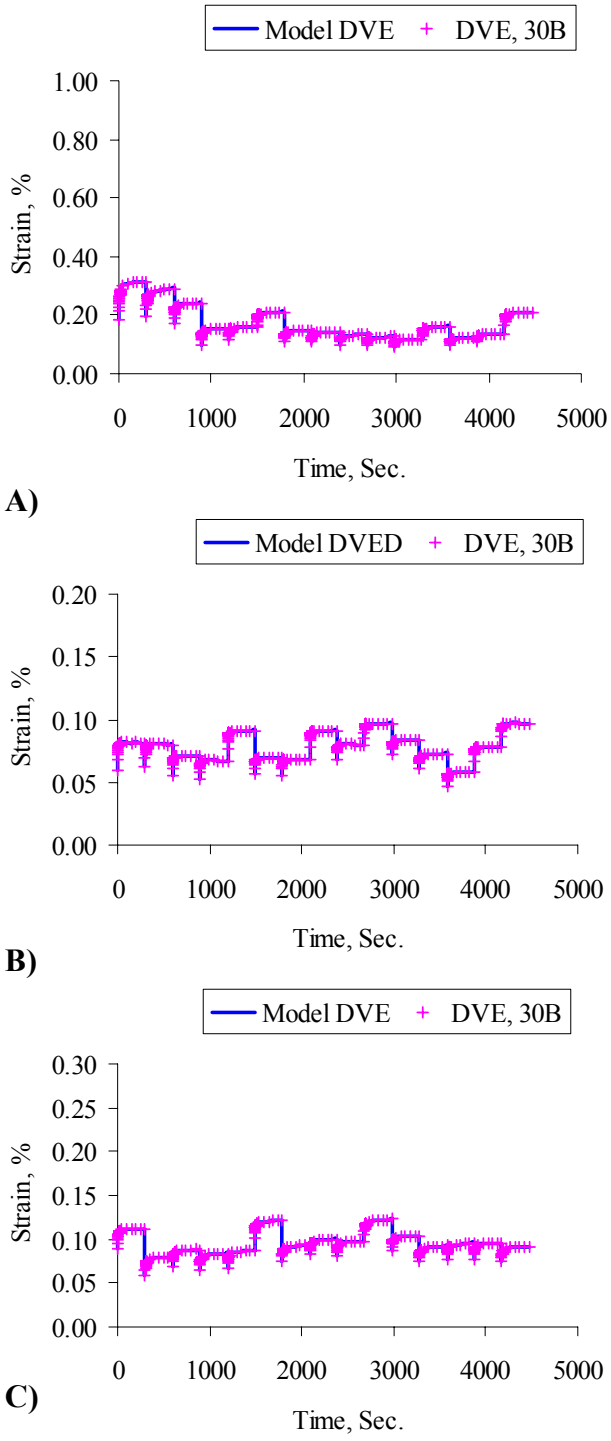

Fig. 4.1. Experimental and Modeled Damage Viscoelastic Strain at 30 psi Confinement and Medium Stress Level for A) Gravel, B) Limestone, and C) Granite Mixes

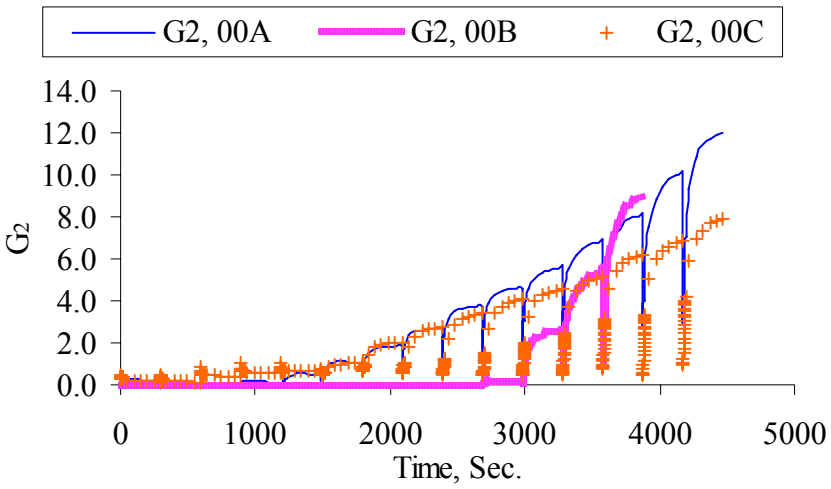

Fig. 4.2. Nonlinearity Damage Parameter for the Limestone Mix at 0 psi Confinement

The results in the Appendix indicate the G_2 value for each mix was much less affected by the applied deviatoric stress compared with the confinement level. Therefore, it was decided to average the G_2 values for the three deviatoric stress levels at each confinement. This averaging approach was followed to allow investigating the influence of confinement on viscoelastic damage. As discussed in Chapter III, the damage parameter G_2 is taken to include the effect of confinement on the material response. A high G_2 value of 55 associated with gravel mix at zero confinement. The increase in confinement reduced the damage parameters for three mixes. This is more pronounced in the gravel mix where the damage parameter values dropped significantly with an increase in confinement.

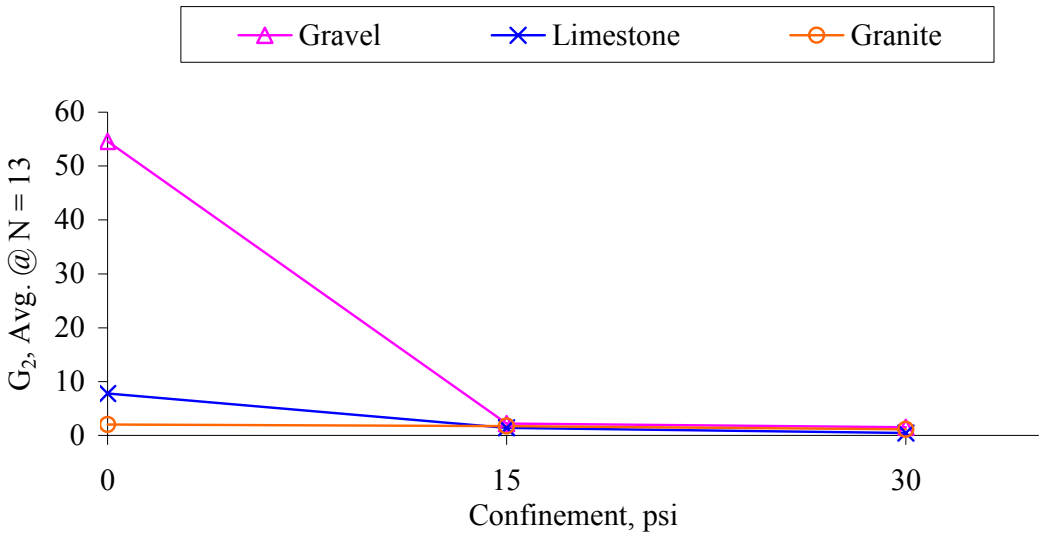

Fig. 4.3. Damage Parameter G_2 at N = 13 for the Three Mixes

The relation between the damage viscoelastic model parameters and the coarse aggregate angularity is presented in Fig. 4.4. It can be seen that at 0 psi confinement gravel that has the lowest angularity had the highest damage parameter value and granite that has the highest angularity had the lowest damage parameter. There is very good correlation between coarse aggregate angularity and G_2 at zero confinement, while there is almost no correlation at the confined tests. This may suggest that the influence of coarse angularity on reducing damage might be less under confined conditions. The coarse aggregate texture showed a similar behavior to the angularity at 0 psi confinement level. As shown in Fig. 4.5, the fine aggregate texture did not correlate to the damage parameter at low confinement level, but it did correlate to the damage parameter at the 15 and 30 psi confinement levels. This suggests that the role of the fine aggregate is more important at higher confinement levels.

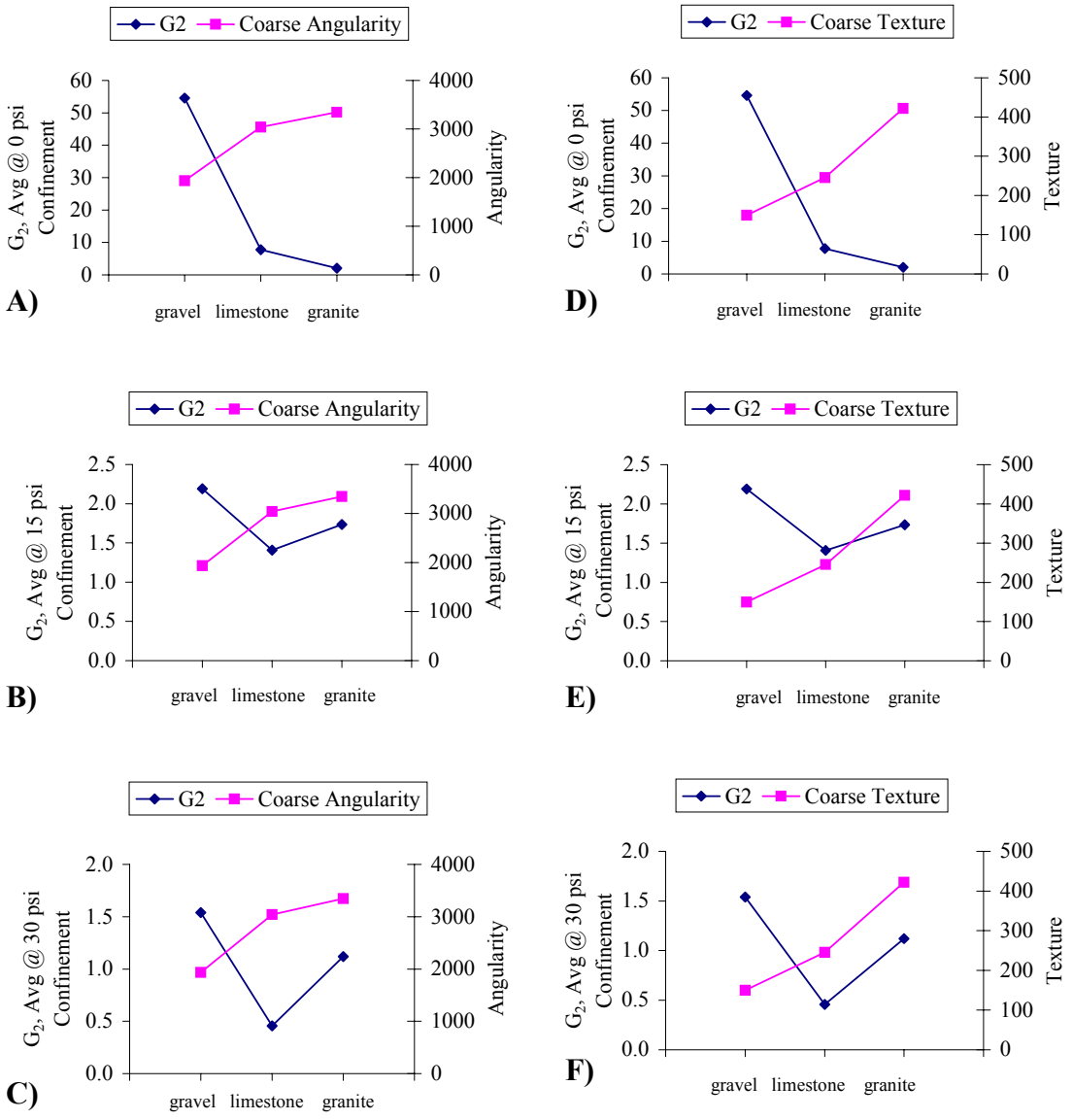

Fig. 4.4. Relation between Nonlinearity Damage Viscoelastic Model Parameter and Coarse Aggregate Angularity and Texture

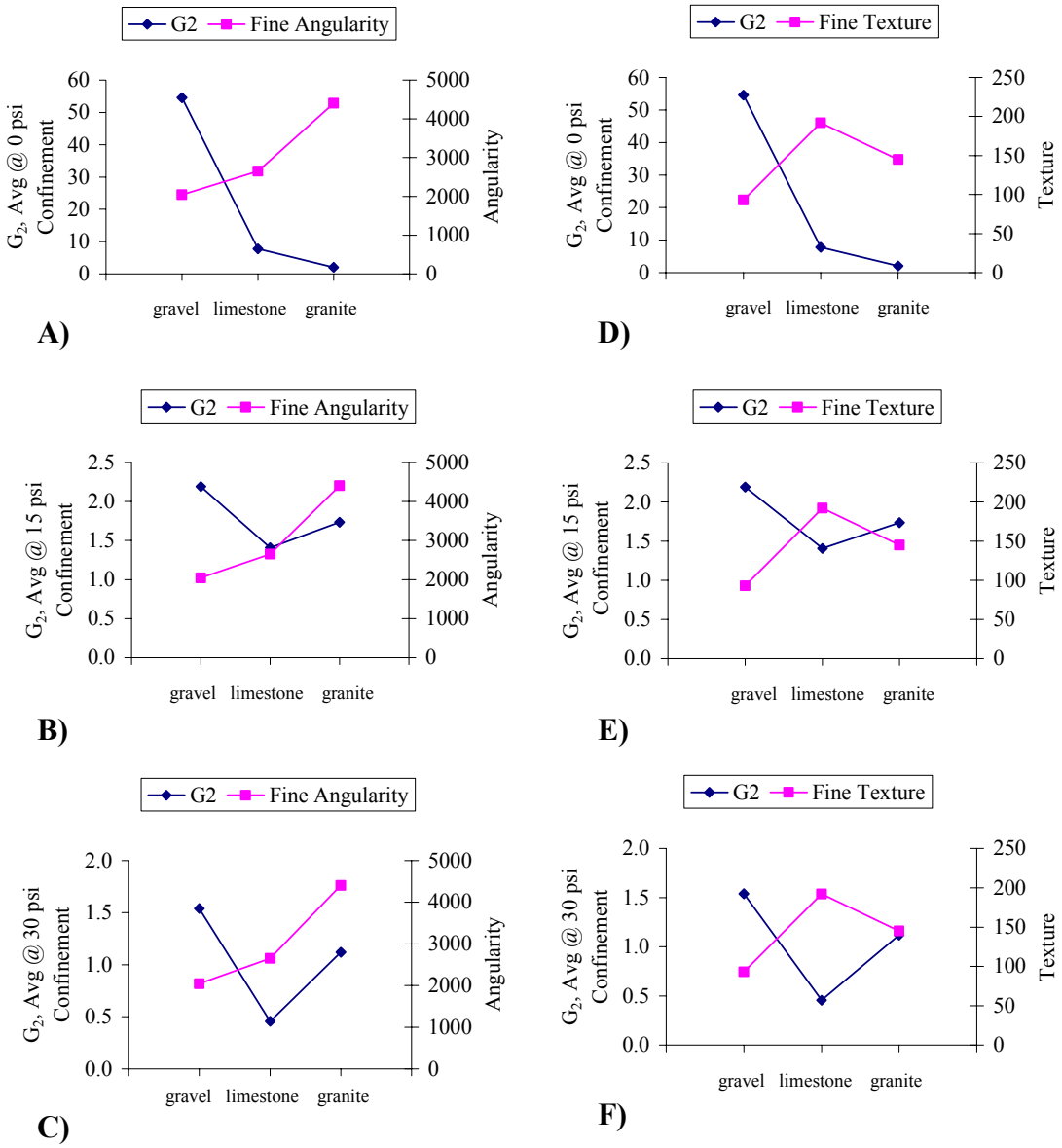

Fig. 4.5. Relation between Nonlinearity Damage Viscoelastic Model Parameter and Fine Aggregate Angularity and Texture

VISCOPLASTIC MODEL

There are several constitutive continuum models that have been established to describe HMA response. However, most of these models do not consider the influence of the microstructure distribution on the material response. Dessouky (2005) addressed this issue by including microstructural characteristics of HMA in a viscoplastic continuum model. This model was further developed in this study, and the model's parameters were determined using the repeated creep test results. The viscoplastic strain rate is defined using the flow rule as follows:

$$\dot{\varepsilon}^{vp} = \Gamma \cdot < \phi(f) > \cdot \frac{\partial g}{\partial \sigma} \tag{4-2}$$

where Γ is the fluidity parameter, which establishes the relative rate of viscoplastic straining, f is the yield function, g is the plastic potential function, $\frac{\partial g}{\partial \sigma}$ is a deviatoric vector in stress space which defines the direction of the viscoplastic flow, and $\phi(f)$ is taken as a power law function of the viscous flow.

The Macauley brackets, < >, are used to indicate the following:

$$< \phi(f) > = \begin{cases} 0, & \phi(f) \le 0 \\ \phi(f) = f^N, & \phi(f) > 0 \end{cases} \tag{4-3}$$

The yield function is taken to have the form in Eq. (4-4):

$$f = F(I_1, J_2, J_3, d, \Delta, \xi) - \kappa = 0 \tag{4-4}$$

where I_1 is the first stress invariant, J_2 is the second deviatoric stress invariant, J_3 is the third deviatoric stress invariant, d is the ratio of yield stress in uniaxial tension to that in uniaxial compression, Δ is an internal parameter that accounts for the effect of the material anisotropy, ξ is an internal parameter that accounts for material softening, and κ is a hardening parameter that describes the growth of the viscoplastic yield surface.

The invariants, I_1, J_2, and J_3 account for the effect of confinement, the dominant shear stress causing the viscoplastic deformation, and the direction of stress. *N* is a parameter characterizing the material rate sensitivity.

A modified formulation of the Drucker-Prager yield function is adopted here with the following form:

$$f = \bar{\tau}^e - \alpha \bar{I}_1^e - \kappa = 0 \tag{4-5}$$

$$\bar{\tau}^e = \frac{\sqrt{\bar{J}_2^e}}{2(1-\xi)}\left[1 + \frac{1}{d} - \left(1 - \frac{1}{d}\right)\frac{\bar{J}_3^e}{\left(\bar{J}_2^e\right)^{3/2}}\right] \tag{4-6}$$

$$\bar{I}_1^e = \frac{1}{1-\xi} \cdot \sigma_{ik} F_{ki} \tag{4-7}$$

$$\bar{J}_2^e = \frac{3}{2} \cdot \frac{1}{(1-\xi)^2} \cdot \bar{S}_{ij} \bar{S}_{ji} \tag{4-8}$$

$$\bar{J}_3^e = \frac{9}{2} \cdot \frac{1}{(1-\xi)^3} \cdot \bar{S}_{ij} \bar{S}_{jk} \bar{S}_{ki} \tag{4-9}$$

The bar '¯' indicates that stresses are modified to account for material anisotropy as defined in Eqs. (3-4, 3-5, and 3-6). σ_{ij} and S_{ij} are the stress tensor and the corresponding deviatoric tensor, respectively, and they are related as:

$$S_{ij} = \sigma_{ij} - \frac{1}{3}\sigma_{kk}\delta_{ij} \tag{4-10}$$

δ_{ij} is kronecker delta, where its components are 1 if $i = j$ and 0 if $i \neq j$. ξ is a softening parameter that account for the effect loading and unloading on changing the microstructure distribution, and for the effect of damage caused by the presence of voids (air voids and cracks). Damage can be measured using X-ray computed tomography of HMA specimens loaded to different strain levels as was done by Masad et al. (2003). The d value is taken to be equal to 0.778 as discussed by Dessouky (2005) to ensure that the yield surface convexity condition is maintained. α is a parameter that reflects the material frictional properties. The hardening parameter κ reflects the combined effect of the cohesion and frictional properties of the material. The plastic potential function, g, is assumed to have the same form as the yield function but with a slope of β, which influences the proportions of the volumetric and deviatoric strains.

Model Calibration

The developed model can be written in an extended form for the creep test as:

$$\dot{\varepsilon}^{vp}{}_{11} = \Gamma\left[\frac{1}{1-\xi(\varepsilon^{vp})}\left[\frac{\bar{\sigma}1-\bar{\sigma}3}{d} - \alpha\left(\bar{\sigma}1+2\bar{\sigma}3\right)\right] - k(\varepsilon^{vp})\right]^{N} \frac{3(1-\Delta)}{3+\Delta}\frac{1}{1-\xi(\varepsilon^{vp})}\left[\frac{1}{d} - \frac{\beta(\varepsilon^{vp})}{3}\right] \tag{4-11}$$

As discussed in Chapter III, the viscoplastic strain can be separated from the total strain and, hence, can be used in Eq. (4-11) to determine the model's parameters.

The applied stress levels were selected such that viscoplastic strain rate is very small and is almost equal to zero at the end of the loading cycle. Therefore, the end points of the loading cycles at the hardening experiments will be used to determine the hardening parameters $k(\varepsilon^{vp})$, α, and $\xi(\varepsilon^{vp})$ by substituting $\dot{\varepsilon}^{vp}=0$ in Eq. (4-11) to obtain Eq. (4-12):

$$0=\frac{1}{1-\xi(\varepsilon^{vp})}\left[\frac{\bar{\sigma}1-\bar{\sigma}3}{d}-\alpha\left(\bar{\sigma}1+2\bar{\sigma}3\right)\right]-k(\varepsilon^{vp}) \tag{4-12}$$

The α value was determined by plotting the modified Drucker-Prager yield surface at different strain levels. Statistical analysis including least-squares method and nonlinear regression using least-squares in Statistical Package for the Social Sciences (SPSS 11) was used to find the $k(\varepsilon^{vp})$, α, and $\xi(\varepsilon^{vp})$ functions. It was found that the α value is almost constant, which is similar to the finding by Dessouky (2005) for monotonic tests. All the experimental results showed that $k(\varepsilon^{vp})$ evolved with loading cycles. Fig. 4.6 presents the experimental fitting of the data.

The evolution law for κ is postulated based on the experimental measurements presented by Masad et al. (2003), and motivated by the work of Dafalias (1990):

$$\kappa=\kappa_o+\kappa_1\left[1-\exp\left(-\kappa_2\bar{\varepsilon}^{vp}\right)\right] \tag{4-13}$$

where $\bar{\varepsilon}^{vp}$ is the effective viscoplastic strain, κ_o defines the initial yield surface, and κ_1 and κ_2 are hardening coefficients. The fitting at the end of all cycles using Eq. (4.12) gave initial estimates of the softening (ξ) function. However, this function was further refined based on fitting the measurements within all cycles.

The fluidity parameter Γ, the rate sensitivity parameter N and the refined softening function $\xi(\varepsilon^{vp})$ were determined by fitting Eq. (4-11) to all experimental measurements within all cycles. At this point an iterative solution was followed to refine the softening function determined from Eqs. (4-11 and 4-12) until convergence was satisfied according to minimizing square error technique and nonlinear regression analysis in SPSS 11 software. The softening evolution function in Eq. (4-14) was found to fit the experimental measurements, while all the model's parameters are shown in Table 4.1.

$$\xi = \xi_0 + \xi_1 * (I_0/3) + \xi_2 * \ln\left[\varepsilon^{vp}\right] * (I_0/3) \tag{4-14}$$

where $\xi_0, \xi_1,$ and ξ_2 are material constants and $(I_o/3)$ is the initial confining pressure. Fig. 4.7 presents the softening parameter ξ for the three mixes.

The model is then taken a further step to extract the dilation parameter for each of the mixes $\beta(\varepsilon^{vp})$. The plastic strain rate ratio (PSRR) can be shown to be equal to Eq. (4-15):

$$PSRR(\varepsilon^{vp}) = \frac{-\dot{\varepsilon}^{vp}_{33}}{-\dot{\varepsilon}^{vp}_{11}} \frac{-\dfrac{\partial g}{\partial \sigma_{33}}}{\dfrac{\partial g}{\partial \sigma_{11}}} = \frac{(1+\Delta)}{(1-\Delta)} \cdot \frac{3+2\cdot d\cdot \beta(\varepsilon^{vp})}{6-2\cdot d\cdot \beta(\varepsilon^{vp})} \tag{4-15}$$

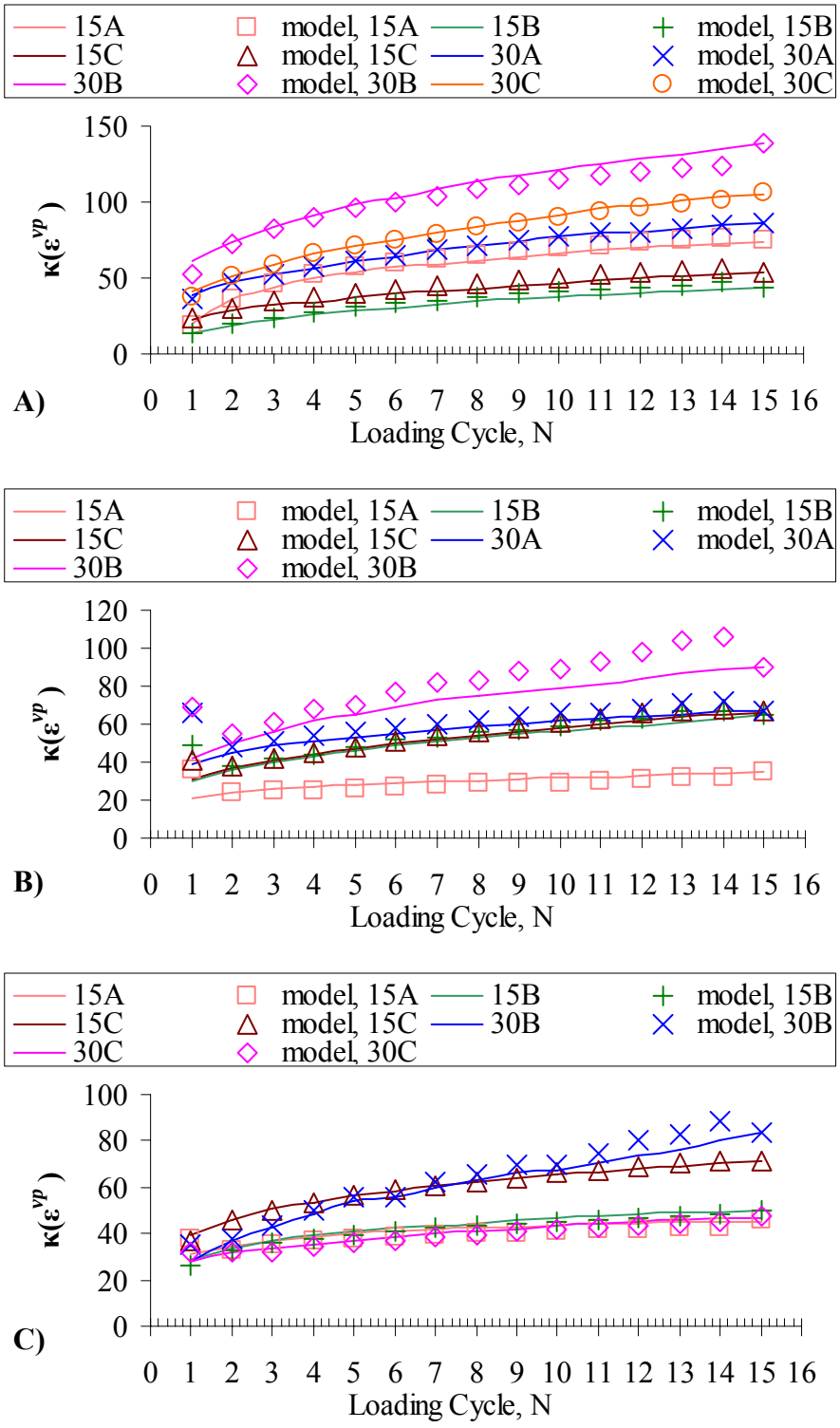

Fig. 4.6. Presentation of the Hardening Function Fitting for A) Gravel, B) Limestone, and C) Granite Mixes

Table 4.1. Model Parameters for the Three Mixes

	Gravel	Limestone	Granite
Δ	0.261	0.436	0.28
α	0.169	0.169	0.169
κ_1	2	2	2
κ_2	363	280	362
κ_3	0.112	0.3	0.3
d	0.778	0.778	0.778
β_1	6.037	-0.10	-0.84
β_2	7.163	2.00	0.74
β_3	0.068	5.00	6.44
Γ	0.0024	0.0001	0.0001
N	2.8	1	1
ξ_0	0.03842	-0.0198	-0.0142
ξ_1	-0.00150	0.0004	0.0017
ξ_2	0.00019	0.0036	0.0022

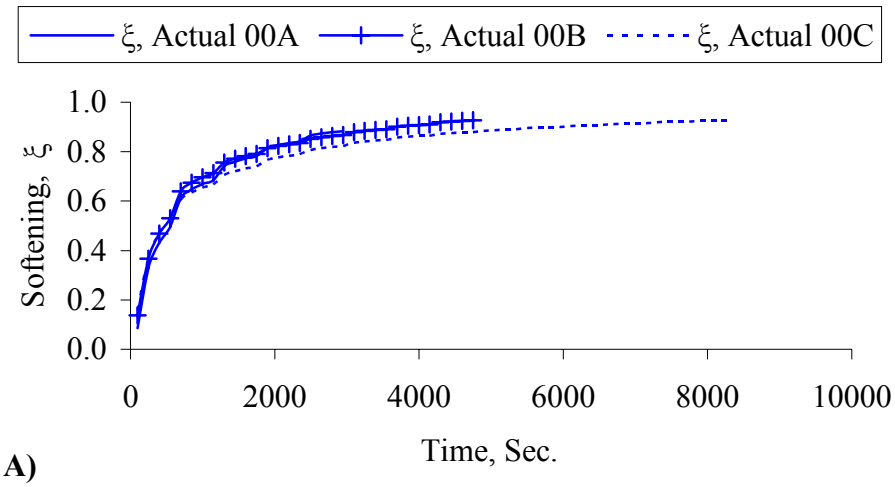

A)

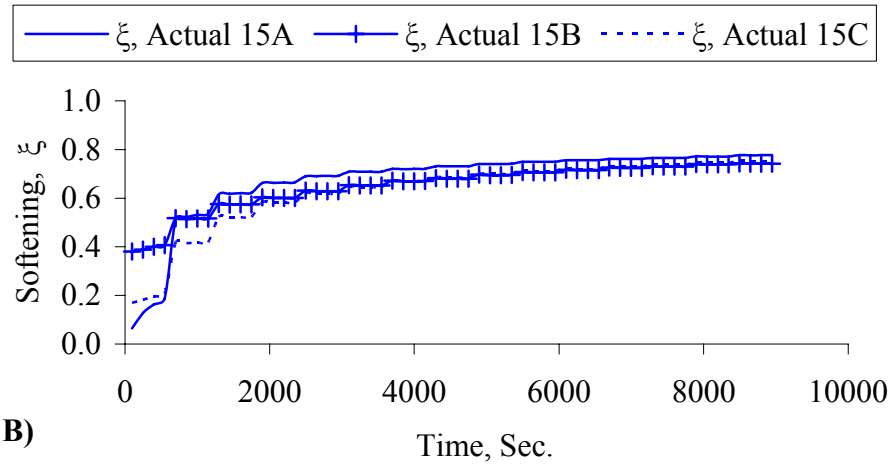

B)

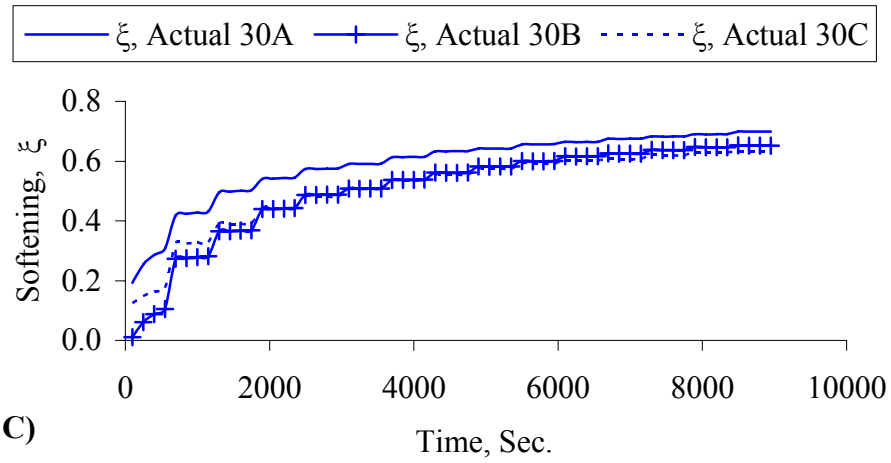

C)

Fig. 4.7. The Softening Parameter ξ for the Gravel Mix at A) 0, B) 15, and C) 30 psi Confinement

Fig. 4.8 presents the PSRR for the gravel, limestone, and granite mixes. It can be seen that gravel and granite mixes exhibited mostly contractive behavior (PSRR < 0.5), whereas the limestone mix was mostly dilating.

It is noted that these mixes were also tested in previous studies by the author of this dissertation using monotonic compression triaxial tests, and the PSRR values (Fig. 4.9) were very different than those obtained under repeated creep loading, as shown in Fig. 4.8. Monotonic tests do not include unloading or rest periods, and consequently, the aggregate structure is under continuous loading. This type of loading could force aggregates to interlock and dilate. However, unloading in creep tests allows the aggregate structure to relax and redistribute itself, which would reduce the interlocking among aggregates and the associated dilation. This observation emphasizes that different loading conditions and stress states could mobilize different deformation mechanisms in HMA mixes.

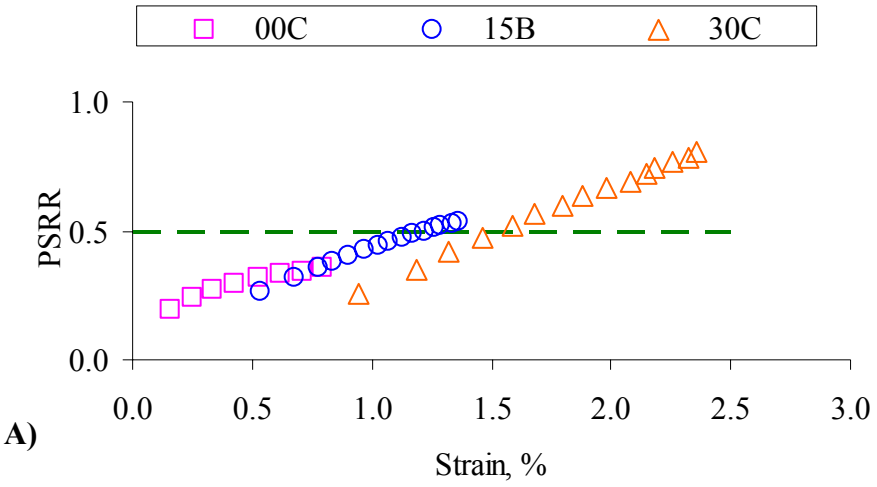

A)

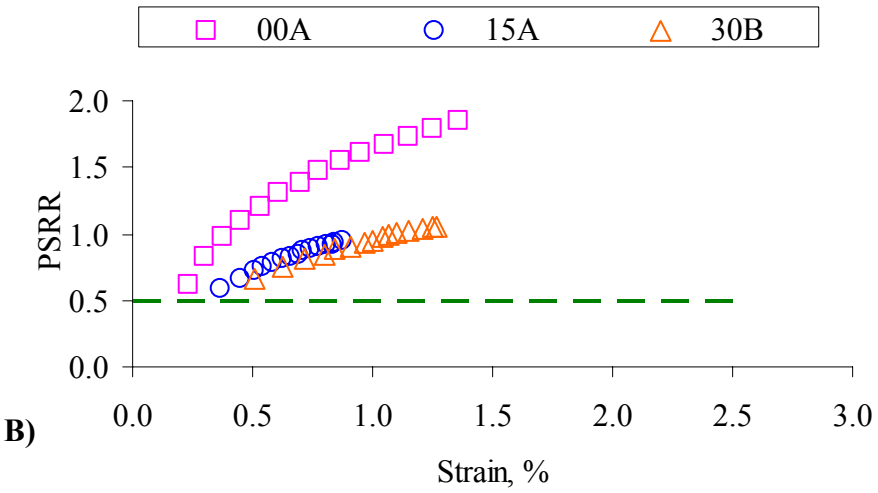

B)

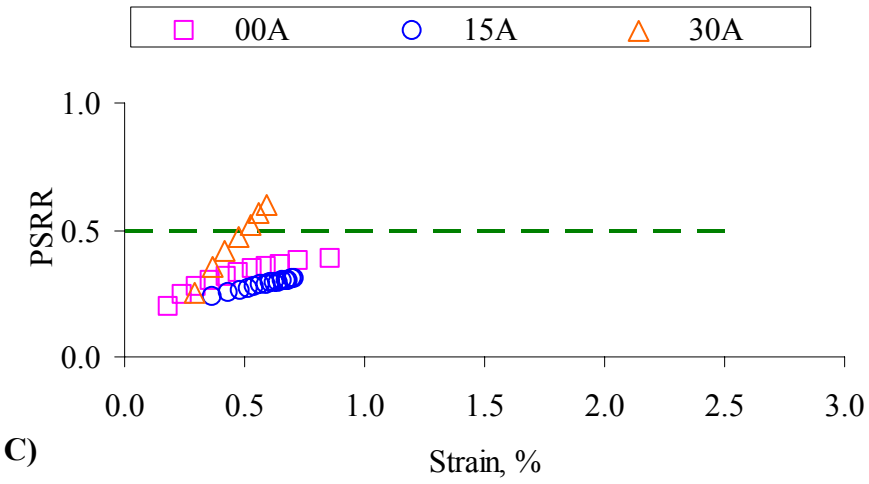

C)

Fig. 4.8. Plastic Strain Rate Ratio for A) Gravel, B) Limestone, and C) Granite Mixes from Repeated Creep Test

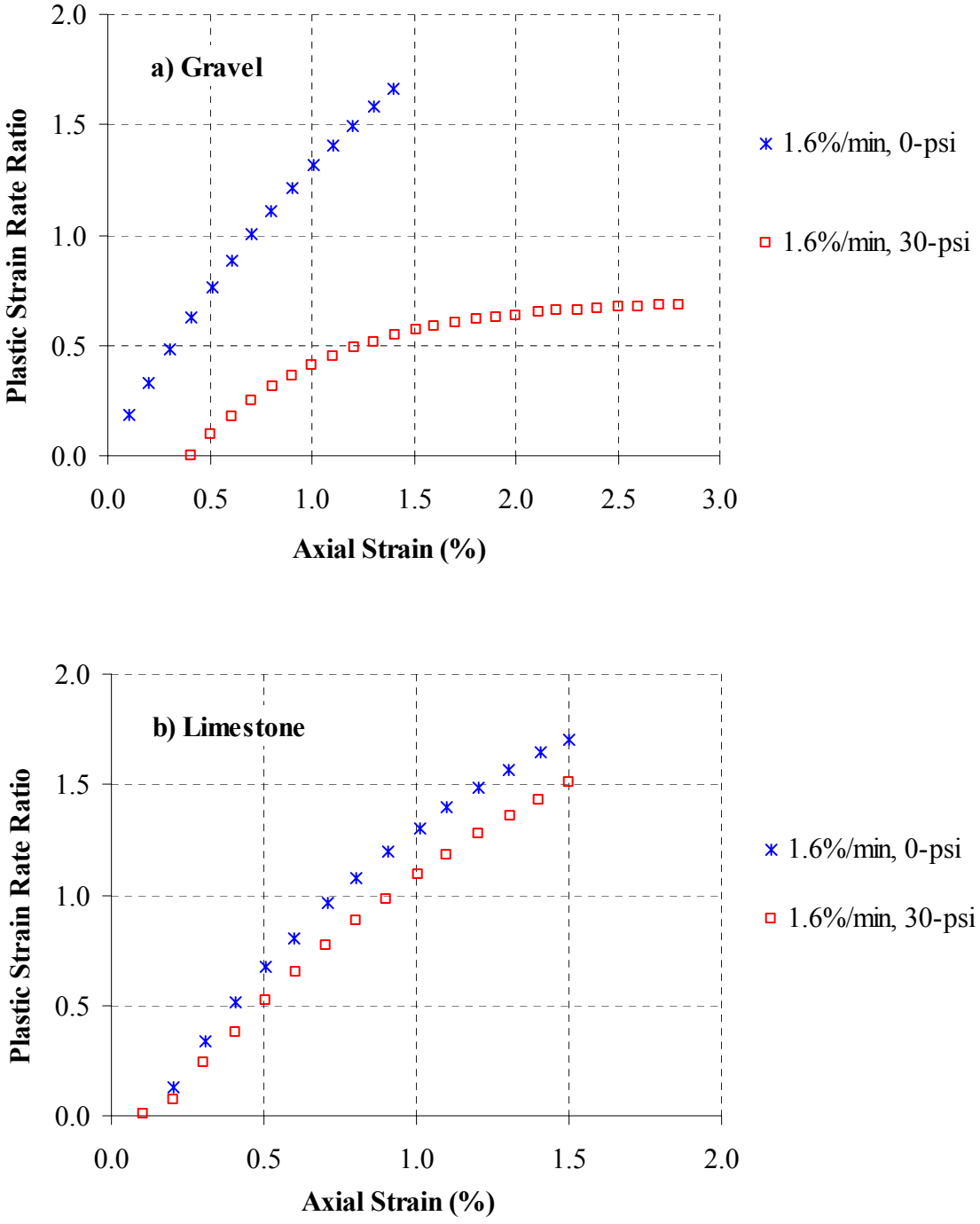

Fig. 4.9. Plastic Strain Rate Ratio for A) Gravel, B) Limestone, and C) Granite Mixes from Monotonic Constant Strain Test

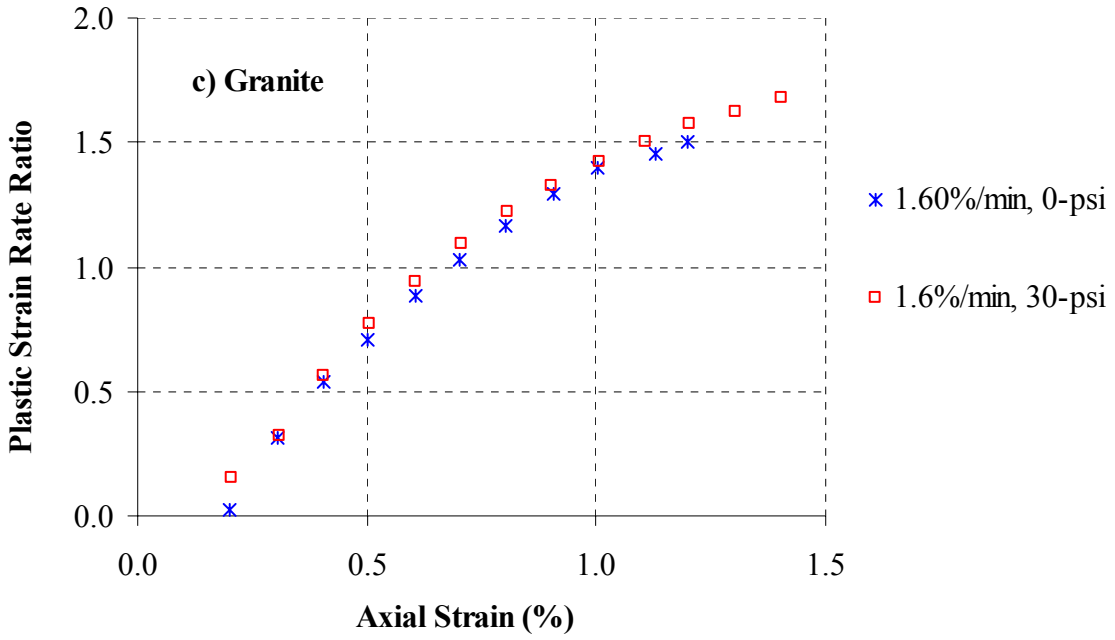

Fig. 4.9. Continued

The PSRR measurements from the creep tests were substituted in Eq. (4-15), and the dilation function $\beta(\varepsilon^{vp})$ was calculated and fitted using the form:

$$\beta(\varepsilon^{vp}) = \beta_1 - \beta_2 e^{-\beta_3 \varepsilon^{vp}} \tag{4-16}$$

Fig. 4.10 presents the fitted dilative potential for the gravel, limestone, and granite mixes. A summary of the model parameters for the three mixes was shown earlier in Table 4.1.

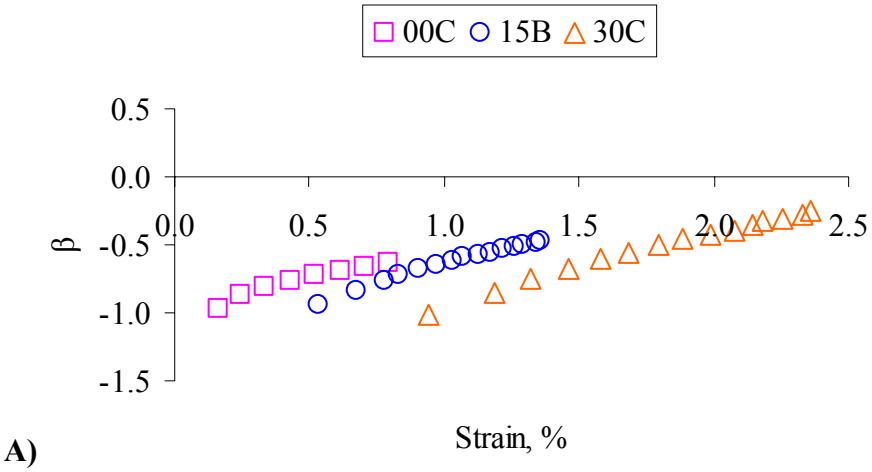

A)

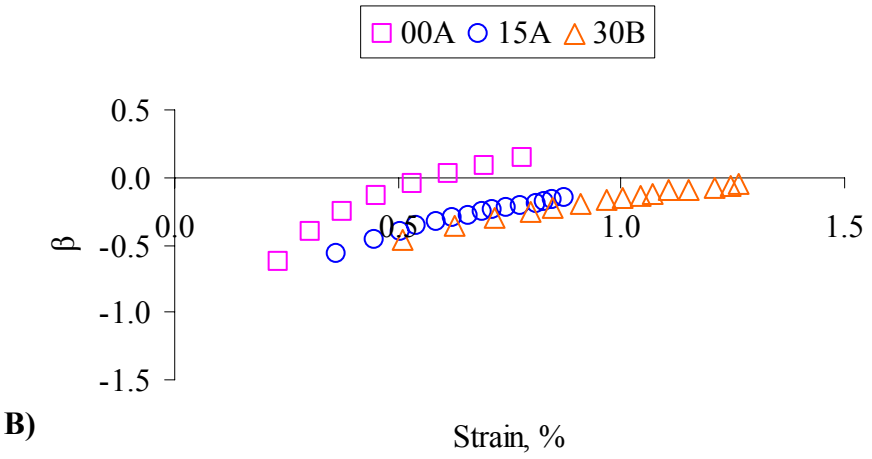

B)

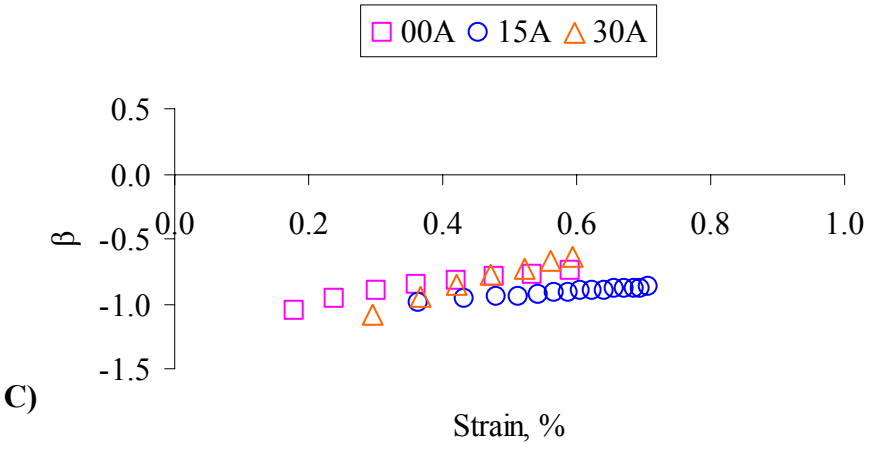

C)

Fig. 4.10. The Dilative Potential $\beta(\varepsilon^{vp})$ for A) Gravel, B) Limestone, and C) Granite Mixes

Relationship of Viscoplastic Model's Parameters to Material Properties

Figs. 4.11 and 4.12 present the experimental strain rate and the model strain rate for the gravel and limestone mixes at different confinement levels and high stress levels. The entire experimental strain rate and the model strain rate figures are presented in the Appendix.

As shown in Figs. 4.11 and 4.12, in some tests hardening was more pronounced than damage. In these tests, the strain rate decreased with increasing number of cycles. However, in cases where damage was more pronounced than hardening, the strain rate increased with increasing number of cycles. In few cases, specimens failed permanently after a few cycles without developing an increasing strain rate. This might be associated with the heterogeneity of these specimens that caused highly localized strains early during the loading process.

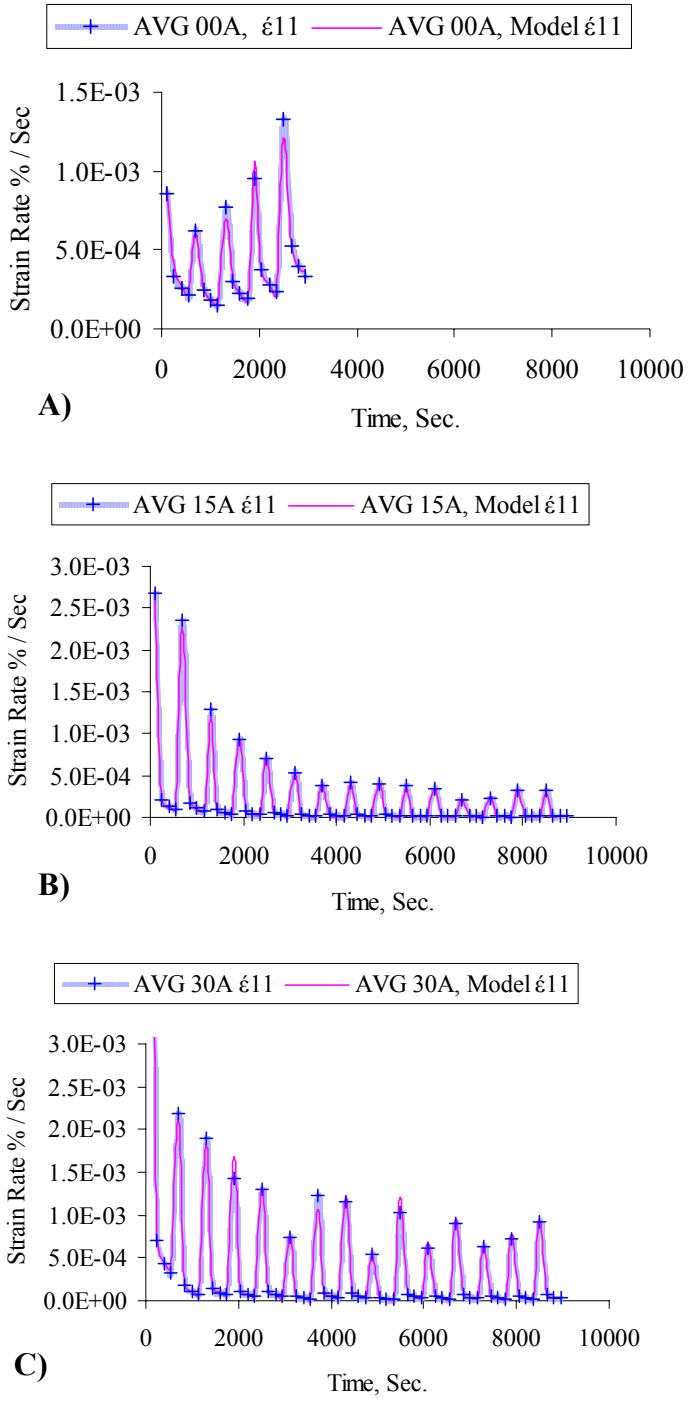

Fig. 4.11. Experimental Strain Rate and Model Strain Rate for the Gravel Mix at A) 0, B) 15, and C) 30 psi Confinement and High Stress Level

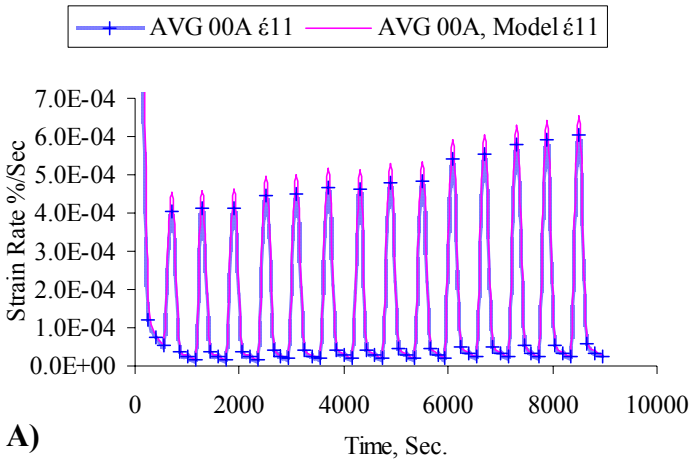

A)

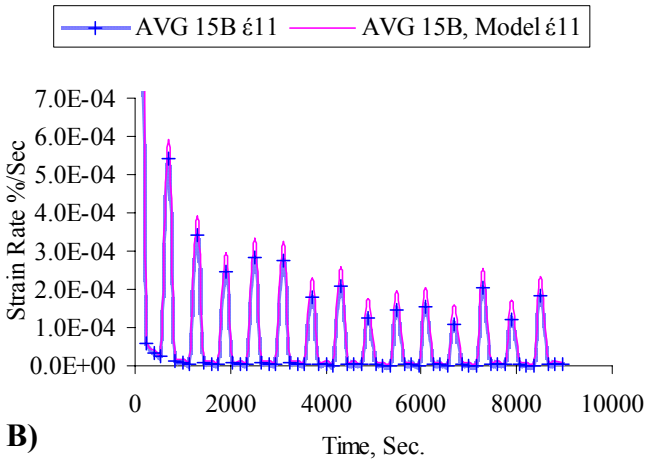

B)

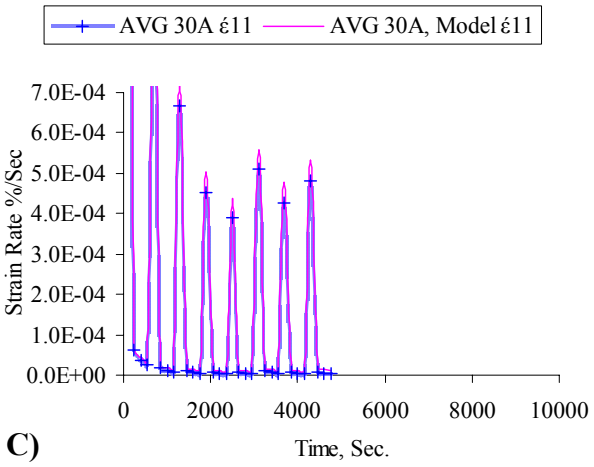

C)

Fig. 4.12. Experimental Strain Rate and Model Strain Rate for the Limestone Mix at A) 0, B) 15, and C) 30 psi Confinement and High Stress Level

The effect of confinement on hardening was more pronounced in the gravel mix. The gravel mix showed significant increases in hardening with increasing confinement (Fig. 4.6). The limestone and granite mixes showed an increase in hardening with increasing confinement but not as significant as that in the gravel mix. The aggregates of these mixes are more angular and textured than the gravel, which might have given these mixes higher hardening properties that is less affected by confinement. This finding is consistent with the results of the analysis of damage viscoelasticity.

Fig. 4.13 presents the hardening function for the three mixes. It can be seen that the granite has the greatest hardening values, whereas the gravel has the lowest hardening values. This can be justified by recognizing that the gravel aggregate is less angular and less textured than the other two mixes, whereas the granite is more angular and more textured than the other two mixes. This is consistent with the results of Dessouky (2005).

The plastic strain rate ratio showed that the material either contracts for a number of loading cycles then starts dilating (PSRR > 0.5) or the material keeps contracting (PSRR < 0.5) (Figs. 4.8 and 4.9). It was found that the cases where the material contracted were associated with mixes that hardened and where the state of the material did not go beyond the secondary creep zone. The other cases where specimens exhibited some dilation were associated with mixes and stress states experiments in which the material exceeded the secondary creep zone to damage.

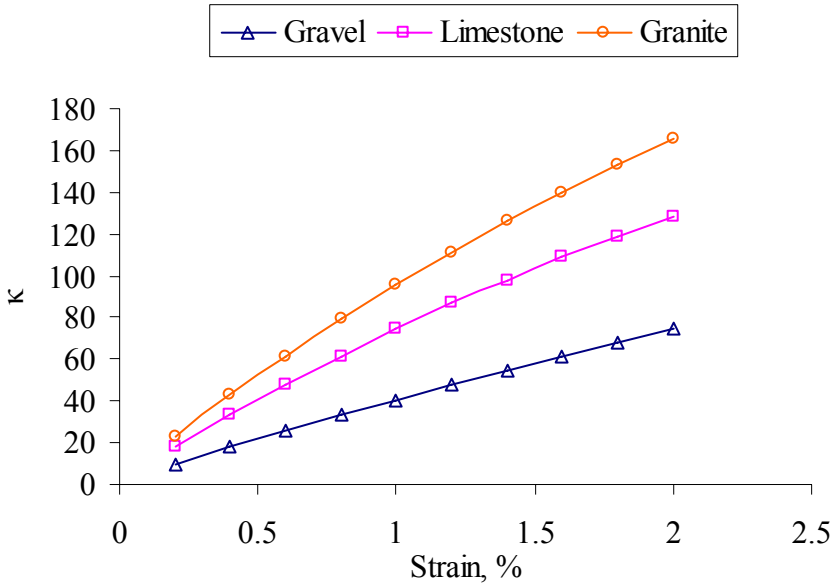

Fig. 4.13. The Hardening Function for the Three Mixes

The softening parameter was found to increase as the confinement decreased in most cases, as shown in Fig. 4.14. In general, within the same confinement, the higher the stress level the higher the softening parameter (Fig. 4.7). The gravel had highest softening parameter values at the zero confinement.

Fig. 4.15 presents the relation between the softening viscoplastic parameter and coarse aggregate angularity. It can be seen that for gravel mix was more affected by confinement than the other two mixes. Also, the correlation between coarse aggregate angularity and softening parameter decreased with an increase in confinement. This suggests that the influence of angularity on reducing softening decreased as confinement increases. The fine texture showed a better correlation with the softening parameter values at higher confinement levels as shown in Fig. 4.16. This suggests that as the

confinement increases the fine aggregate role becomes more significant.

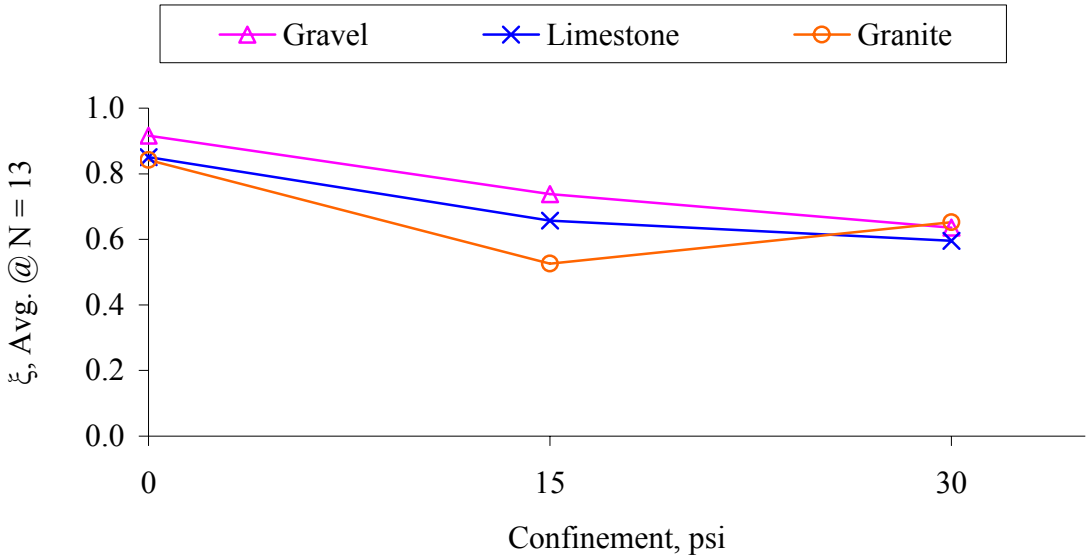

Fig. 4.14. Softening Parameter at N = 13 for the Three Mixes

CONCLUSIONS

An anisotropic damage viscoelastic-viscoplastic model was developed in this chapter. This model is capable of describing the damage viscoelastic response of the mix, which becomes more significant in describing response as temperature decreases and strain rate increases. Also, the model has a viscoplastic component to describe permanent deformation that becomes more significant as temperature increases and strain rate decreases.

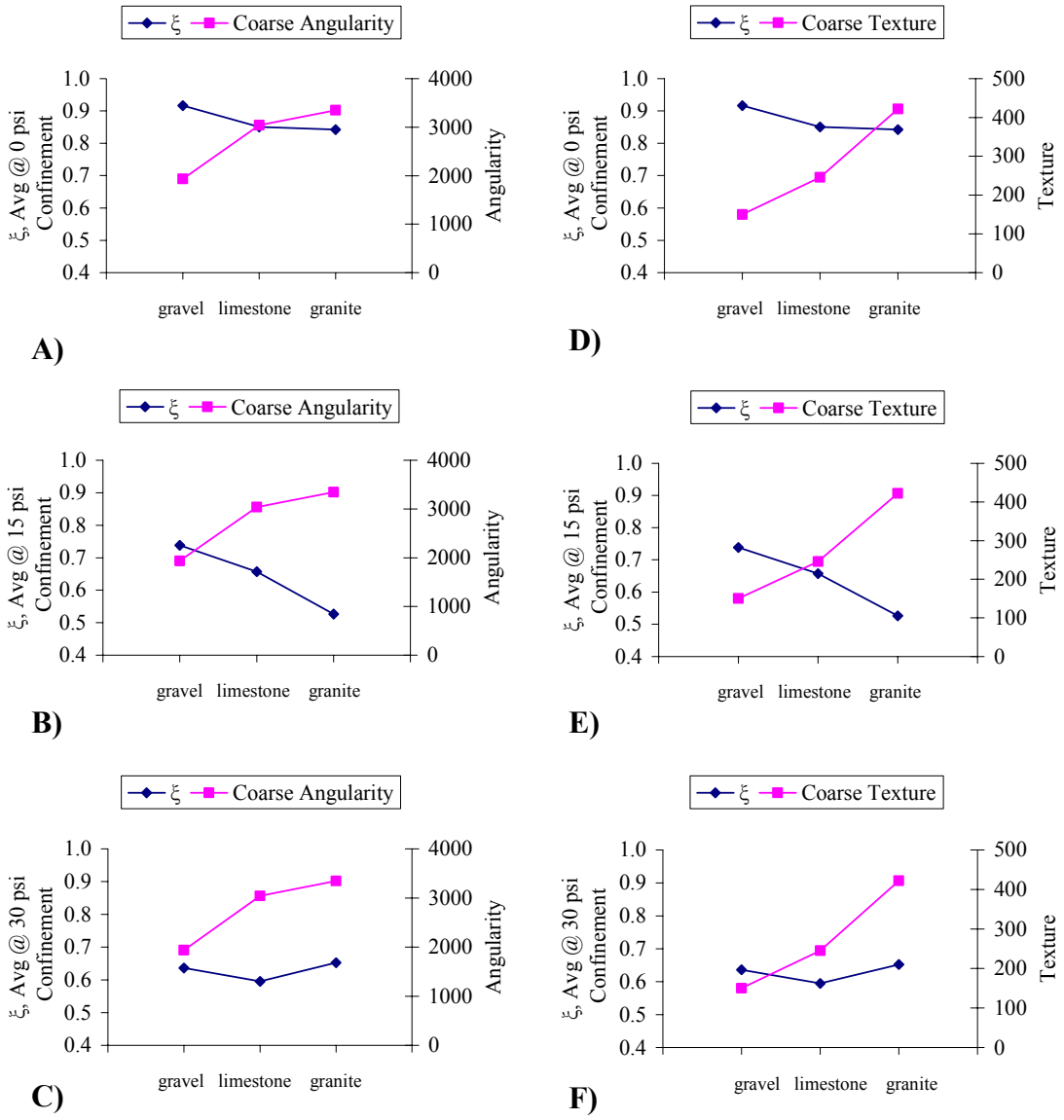

Fig. 4.15. Relation between Viscoplastic Model Softening Parameter and Coarse Aggregate Angularity and Texture

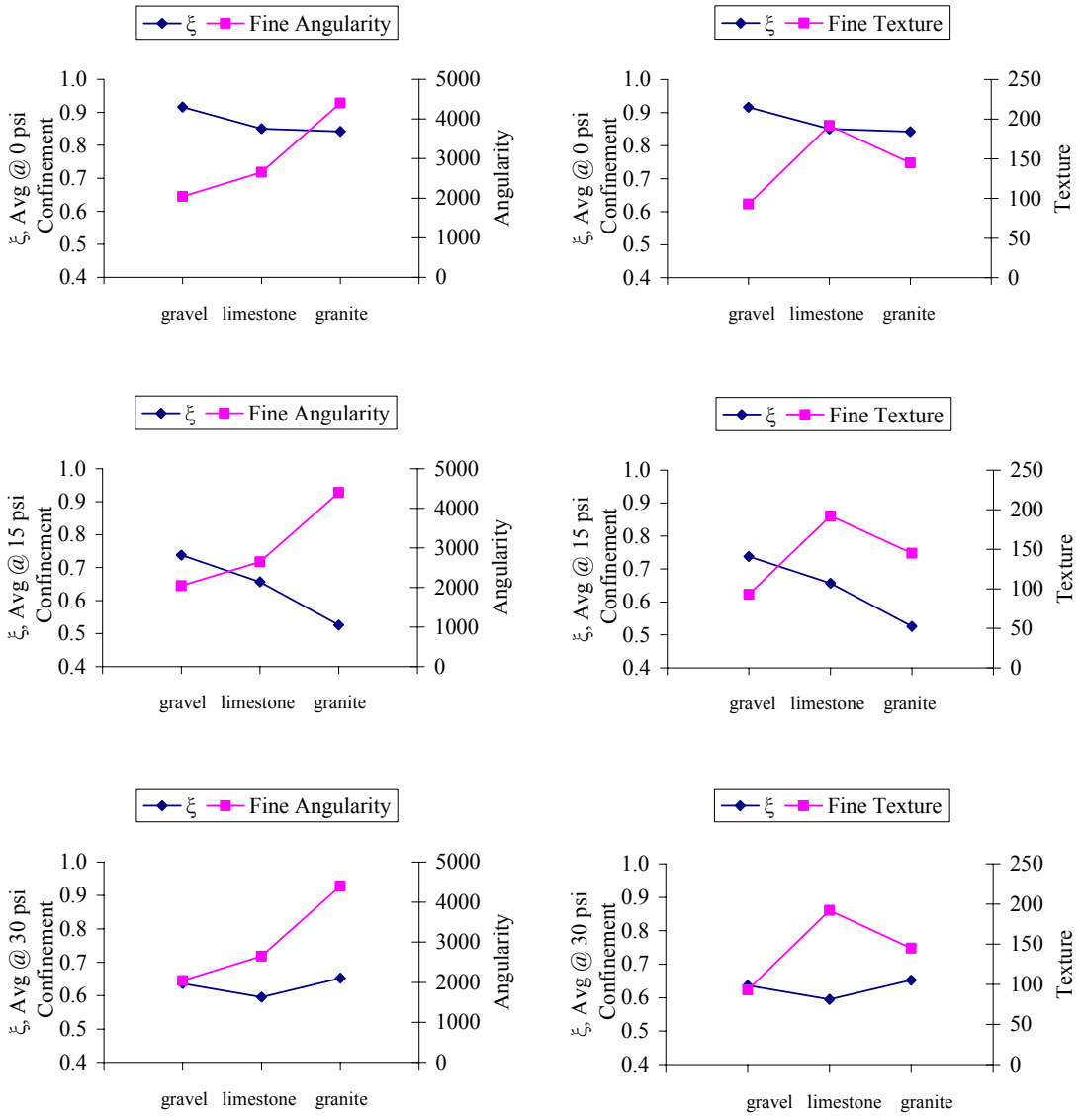

Fig. 4.16. Relation between Viscoplastic Model Softening Parameter and Fine Aggregate Angularity and Texture

The anisotropic damage viscoelastic-viscoplastic model offers a theoretical framework to analyze experimental measurements and characterize the HMA viscoelastic and viscoplastic responses. The deviation of HMA response from linear

viscoelasticity was quantified using the damage viscoelastic parameter G_2. The damage viscoelastic response in the repeated creep test could be used as indicator of the material damage state. An increase in viscoelastic strain rate is an indication of damage. The damage viscoelastic parameter G_2 of the gravel mix was more influenced by confinement than the G_2 of the other two mixes. Also, the correlation of coarse aggregate angularity and texture to G_2 was evident at low confinement while the correlation of fine aggregate texture to G_2 was evident at high confinement.

The experimental program offered a unique identification of the material viscoelastic response that helped calibrating the viscoplastic part of the model. The effect of aggregate properties used in each mix had clear influence on in the viscoplastic model's parameters. This has been well pronounced in the case of the hardening, dilation, and softening parameters of the viscoplastic model. As the angularity and texture increased, the effect of confinement on hardening, dilation, and softening decreased. The relationships between the model's parameters and aggregate characteristics offer the potential to predict these parameters based on characterization of aggregate characteristics.

CHAPTER V

MICROSTRUCTURE CHARACTERIZATION OF HOT MIX ASPHALT IN REPEATED CREEP TEST USING X-RAY COMPUTED TOMOGRAPHY

OVERVIEW

This chapter presents the results of an experiment aimed at capturing and characterizing the three-dimensional distribution of aggregate orientation and air voids in hot mix asphalt (HMA) specimens. The objective is to compare the microstructure distribution in specimens loaded to similar average strain but using different loading conditions and stress states. Specimens were scanned using X-ray computed tomography (CT) before and after being subjected to triaxial repeated creep and recovery tests as well as monotonic constant strain rate tests. The image analysis techniques (IAT) introduced by Tashman (2003) were used to characterize the distribution of voids (air voids and cracks). In addition, three-dimensional X-ray CT images were constructed using the Blob 3D program and the orientations of the maximum length axes of aggregates were quantified.

INTRODUCTION

HMA microstructure distribution is a manifestation of material properties, mix design, compaction method, and loading conditions. The microstructure distribution in this chapter focuses on voids distribution and aggregate orientation due to their significant influence on HMA performance. Voids distribution has been linked to damage in HMA, which is believed to begin with the nucleation of microcracks that later propagate, grow,

and coalesce to form macrocracks as the material is subjected to loading (Kim et al. 1997). It is noted that the term voids is used herein to refer to both air voids that exist in the specimen prior to loading and cracks that develop during loading.

The topic of damage and its influence on HMA response has been addressed by many researchers (Sousa et al. 1993, Park et al. 1996, Kim et al. 1997, Little et al. 1999, and Lytton 2000). Damage in these approaches has been characterized through quantifying changes in mechanical properties with respect to a damage-free reference state. It was not until recently that researchers developed experimental and analytical methods to characterize voids distribution and their influence on HMA mechanical properties and performance (Wang et al. 2001, Masad et al. 1999, Tashman et al. 2004).

Aggregate directional distribution is also analyzed in this chapter due to its influence on HMA anisotropic behavior. Masad et al. (2001) demonstrated the influence of aggregate orientation on HMA mechanical properties through theoretical modeling and finite element simulations. Tashman et al. (2001) and Saadeh (2002) presented experimental measurements illustrating the effect of aggregate orientation in HMA on mechanical properties.

The objective of this chapter is to experimentally capture and characterize the microstructure distribution in HMA as the material undergoes permanent deformation under different loading conditions. This objective is achieved by measuring changes in the microstructure in three mixes before and after testing and by studying the effect of stress state (repeated creep versus monotonic constant strain rate) on the microstructure distribution. The analysis results have implications on modeling HMA as it offers

understanding of the effect of loading conditions, used to determine models' parameters, on microstructure distribution. It also examines the extent of induced anisotropy that develops under loading compared with inherent anisotropy that develops after compaction of HMA. X-ray CT, three-dimensional image analysis software (Blob 3D), and IAT were used to capture and characterize the HMA microstructure.

EXPERIMENT

Three specimens from each of the limestone, granite, and gravel mixes were compacted to about 7% air voids using a Superpave gyratory compactor. Each specimen had a diameter of about 100 mm and a height of around 156 mm. Two specimens from each mix were then loaded to about 1% permanent strain using creep recovery tests. One specimen was loaded using no confinement, while the second specimen was loaded using 30 psi confinement. A summary of the specimens analyzed is presented in Table 5.1. The mix design, aggregate, and binder properties for these specimens are presented in Chapter III.

Another three specimens from the limestone mix were tested using a triaxial compression setup at a constant displacement rate of 2.5 mm/min. Two replicates were loaded to about 1% strain level under a constant confining pressure of 30 psi. The other limestone specimen was loaded to about 1% strain level under 0 psi confining pressure. All tests were conducted at a temperature of 130 °F.

All 12 specimens were scanned using the X-ray CT system. The system had a 420 kV X-ray source and a linear detector. X-ray CT offers a nondestructive method to

obtain digital information on the microstructure of the specimens while the specimens are still intact and capable of being subjected to further mechanical testing (Tashman 2003).

Directing planar X-rays that pass through the specimen along several different paths in several different directions produces a set of two-dimensional images along the specimen's height. These generated CT images are typically referred to as slices. The intensity of X-rays is measured before they enter the specimen and after they pass through it. Scanning of a slice is complete after collecting the intensity measurements for a full rotation through the specimen. The specimen is then shifted vertically by a fixed amount (the slice thickness), and the entire procedure is repeated to generate another segment of slices (Tashman 2003).

In this study, the image horizontal resolution was around 200 μm per pixel, while two-dimensional images (slices) of the microstructure of the HMA specimens were captured every 1 mm across the height of a specimen with a slice thickness of 1 mm.

IMAGE ANALYSIS AND RESULTS

Three-Dimensional Orientation of Aggregates

Researchers at the X-ray CT center at The University of Texas at Austin developed the Blob 3D program, which is capable of extracting basic morphological information about aggregate particles constructed from CT images (Ketcham and Shashidhar 2001). The program was written using interactive data language (IDL). Blob 3D consists of three modules: segmentation, separation, and extracting. The segmentation module identifies the

voxels belonging to each aggregate. However, the user is allowed to make manual adjustments to the three-dimensional visualization in order to make sure that the aggregates are separated in the separation module.

Table 5.1. Summary of Analyzed Specimens

Specimen ID	Mix	Deviatoric Stress	Confinement	Initial Air Voids
		psi	psi	%
G00A	Gravel	7	0	6.58
G30A	Gravel	126	30	7.33
G-Undeformed	Gravel	N/A	N/A	6.81
L30A	Limestone	130	30	6.21
L30B	Limestone	118	30	6.21
L-Undeformed	Limestone	N/A	N/A	6.46
T00B	Granite	15	0	7.12
T30C	Granite	131	30	7.02
T-Undeformed	Granite	N/A	N/A	6.90
LMD1	Limestone	N/A (Constant Strain Rate)	0	7.40
LMD17	Limestone	N/A (Constant Strain Rate)	30	7.17
LMD18	Limestone	N/A (Constant Strain Rate)	30	6.68

The data are extracted in the extracting module. The software is capable of providing data on the microstructure components such as center position, volume, surface area, maximum axis length, maximum axis orientation, minimum axis length, minimum axis orientation, and the length of the three axes of the best-fit ellipse. In this study, Blob 3D was used to measure the maximum aggregate orientation. Fig. 5.1 presents sample of three-dimensional reconstruction of limestone mix specimen by the Blob 3D program.

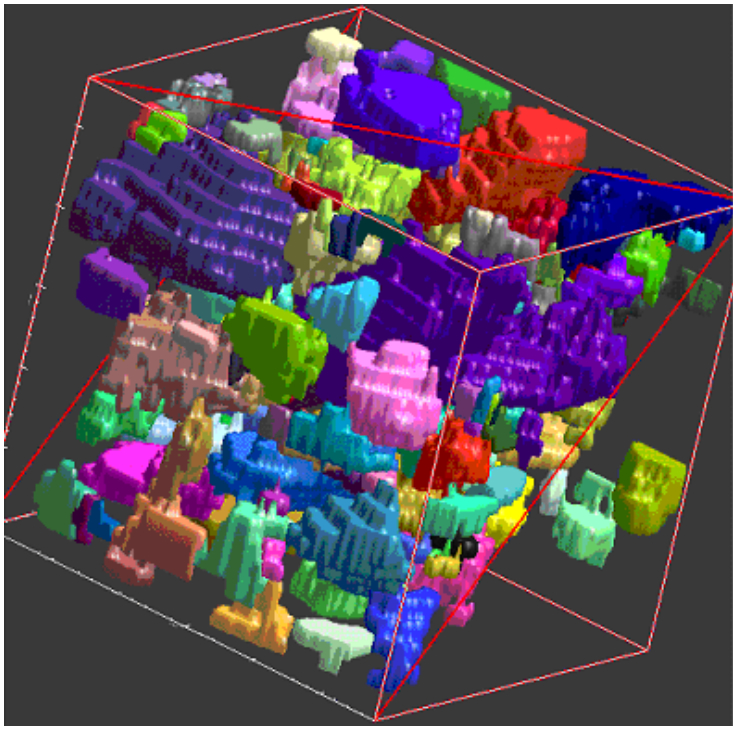

A)

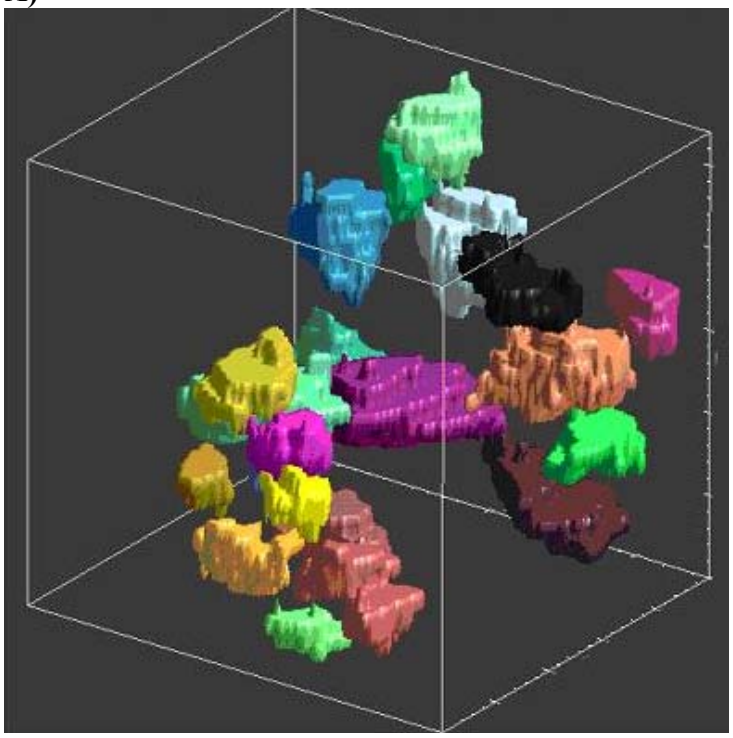

B)

Fig. 5.1. Blob 3D Reconstructed Aggregates A) Subvolume B) Separated Aggregates

Three limestone specimens (L30A, L30B, and L-Undeformed) were analyzed using the Blob 3D program. The maximum axis orientation was measured for the three specimens. The maximum axis orientation was identified in terms of its directional cosines. The analysis results confirmed the transversally anisotropic distribution of aggregate orientation, as there were very small differences in the preferred orientation in the horizontal plane. The directional cosine with the vertical axis (since compacted HMA exhibits transversally anisotropic distribution) was obtained. Fig. 5.2 presents the percentages of limestone aggregate particles with their longest dimensions oriented from the vertical axis at the angles shown in this figure.

It can be seen that the angle with the vertical direction tended to increase after deformation, indicating that the aggregates' maximum axis orientation became closer to the horizontal axis. This can be seen by observing the difference (Angle [Deformed] – Angle [Undeformed]) between the deformed and undeformed specimens is mostly negative at small angles and mostly positive at higher angles. It is evident that stress-induced anisotropy developed for the limestone mix under creep loading.

Fig. 5.3 presents the percentages of aggregate particles with their longest dimensions oriented from the vertical axis at the angles shown in this figure for the limestone specimen loaded using monotonic test (LMD1). It can be seen that there is a slight change depicted for specimens from repeated creep tests. The LMD1 specimen showed the highest percentages of particles for the undeformed specimen oriented at 90° indicating the inherent anisotropy. However, the distribution stayed similar or exhibited less anisotropic distribution after loading.

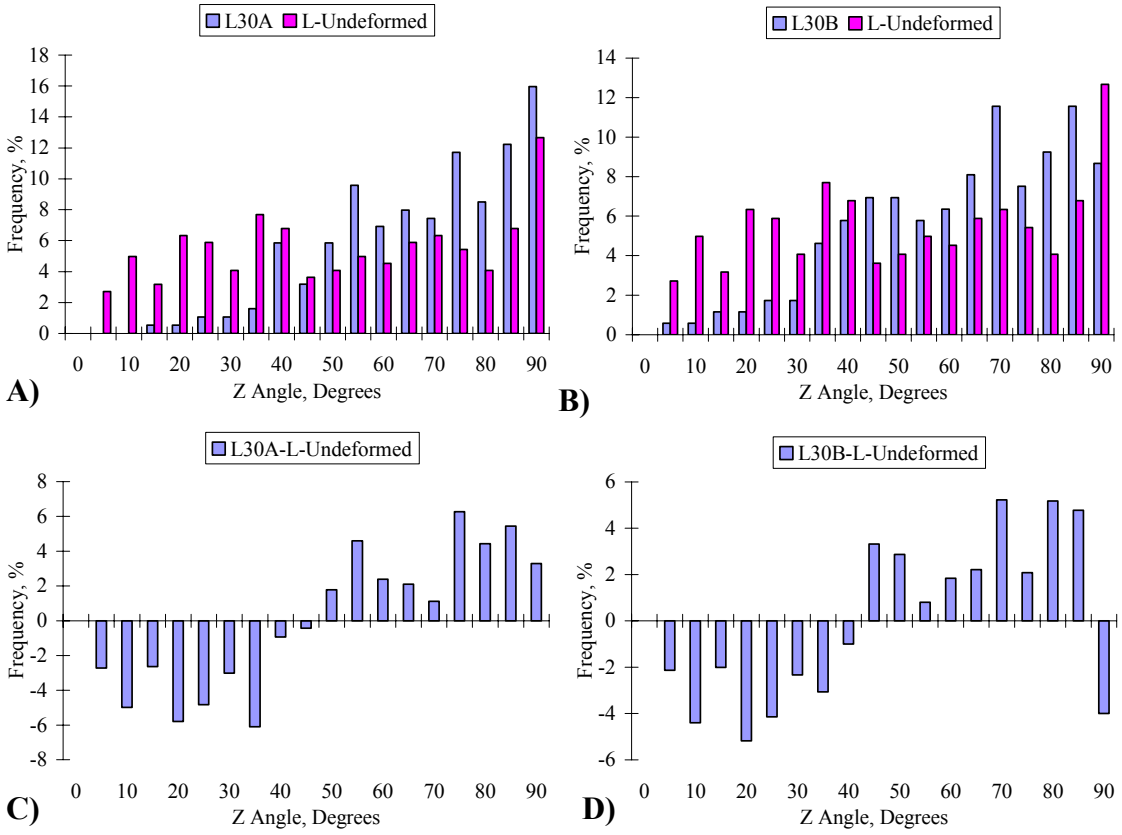

Fig. 5.2. The Percentage of Aggregate Particles with Different Orientations from the Vertical Direction Clustered at Increments of 5° for A) Comparison between Specimen L30A and L-Undeformed, B) Comparison between L30B and L-Undeformed, C) Difference in Angles (the Undeformed Subtracted from L30A Percentages), D) Difference in Angles (the Undeformed Subtracted from L30B Percentages)

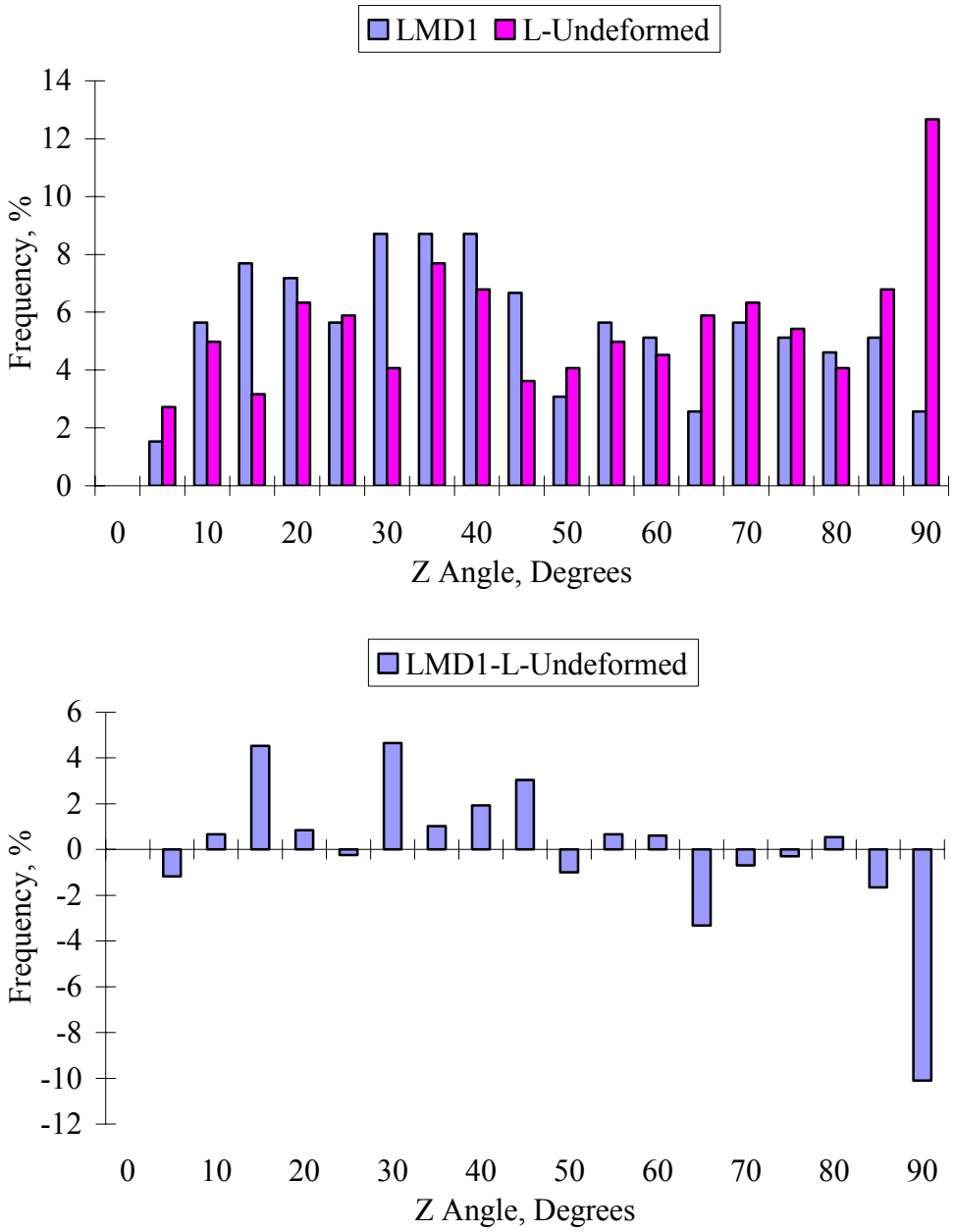

Fig. 5.3. The Percentage of Aggregate Particles with Different Orientations from the Vertical Direction Clustered at Increments of 5° for A) Comparison between Specimen LMD1 and L-Undeformed and B) Difference in Angles (the Undeformed Subtracted from LMD1 Percentages)

The gravel and granite specimens exhibited different behavior than the limestone mix. The particles did not show a clear increase in the percentage of particles oriented toward the horizontal direction with loading as shown in Fig. 5.4 and Fig. 5.5. This might be due to the fact that the gravel and granite aggregate are less flat and elongated than the limestone aggregate, as confirmed by the form indices in Table 3.2. For the granite mix, the high angularity and texture of this aggregate could have contributed to the resistance to re-orientation.

The model presented in this dissertation considers the inherent anisotropy only. However, the experimental measurements during the creep recovery tests gave evidence of aggregate orientation. As was discussed in Chapter III, the viscoplastic strain rate increased after each unloading period. It is possible that particles tend to become more oriented toward the horizontal direction during the loading period. This induced anisotropy increased the mix stiffness in the vertical direction (Masad et al. 2005). However, the level of anisotropy could decrease during the unloading period and the recovery of the viscoelastic strain. This reduction in anisotropy is associated with reduction in vertical stiffness. Consequently, the following loading cycle would experience less stiffness in the vertical direction compared with the stiffness at the end of the previous loading period. As such, the viscoplastic strain rate would be higher at the beginning of the loading cycle than at the end of the previous cycle.

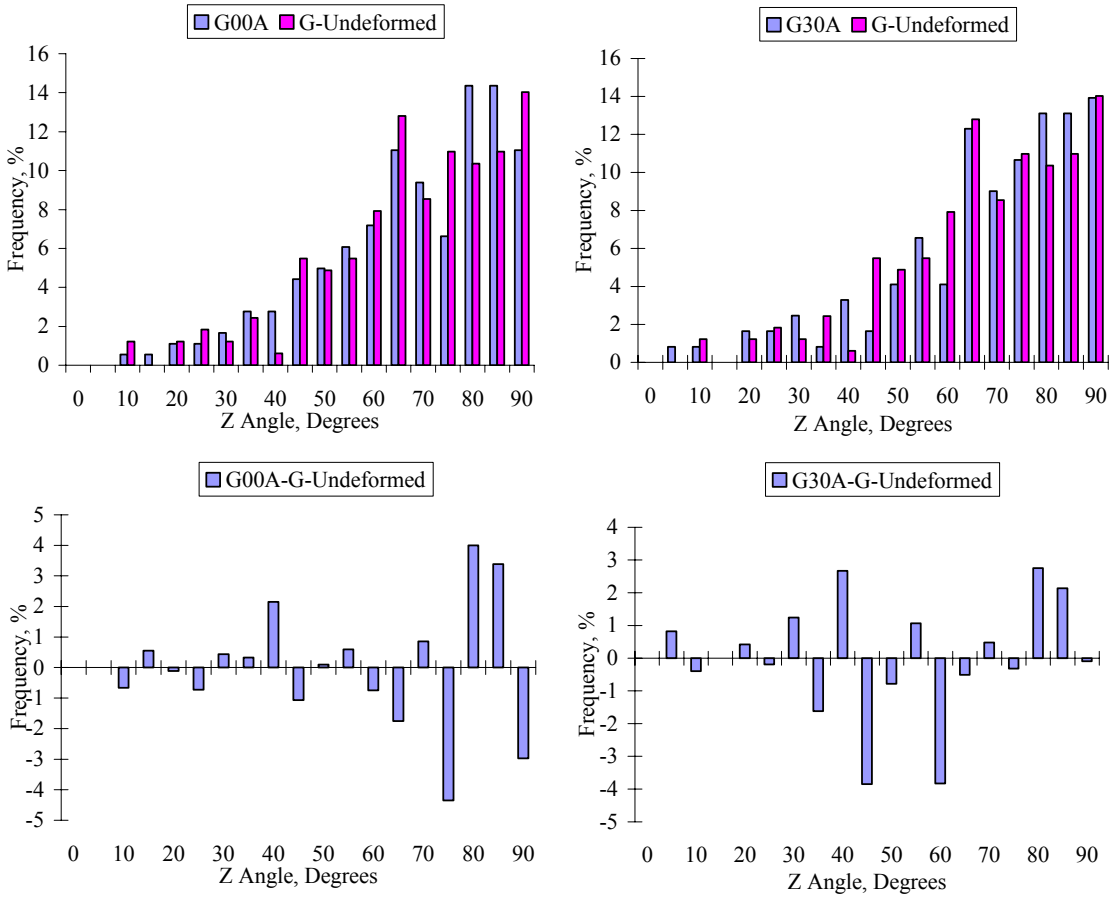

Fig. 5.4. The Percentage of Aggregate Particles with Different Orientations from the Vertical Direction Clustered at Increments of 5° for A) Comparison between Specimen G00A and G-Undeformed, B) Comparison between G30A and G-Undeformed, C) Difference in Angles (the Undeformed Subtracted from G00A Percentages), D) Difference in Angles (the Undeformed Subtracted from G30A Percentages)

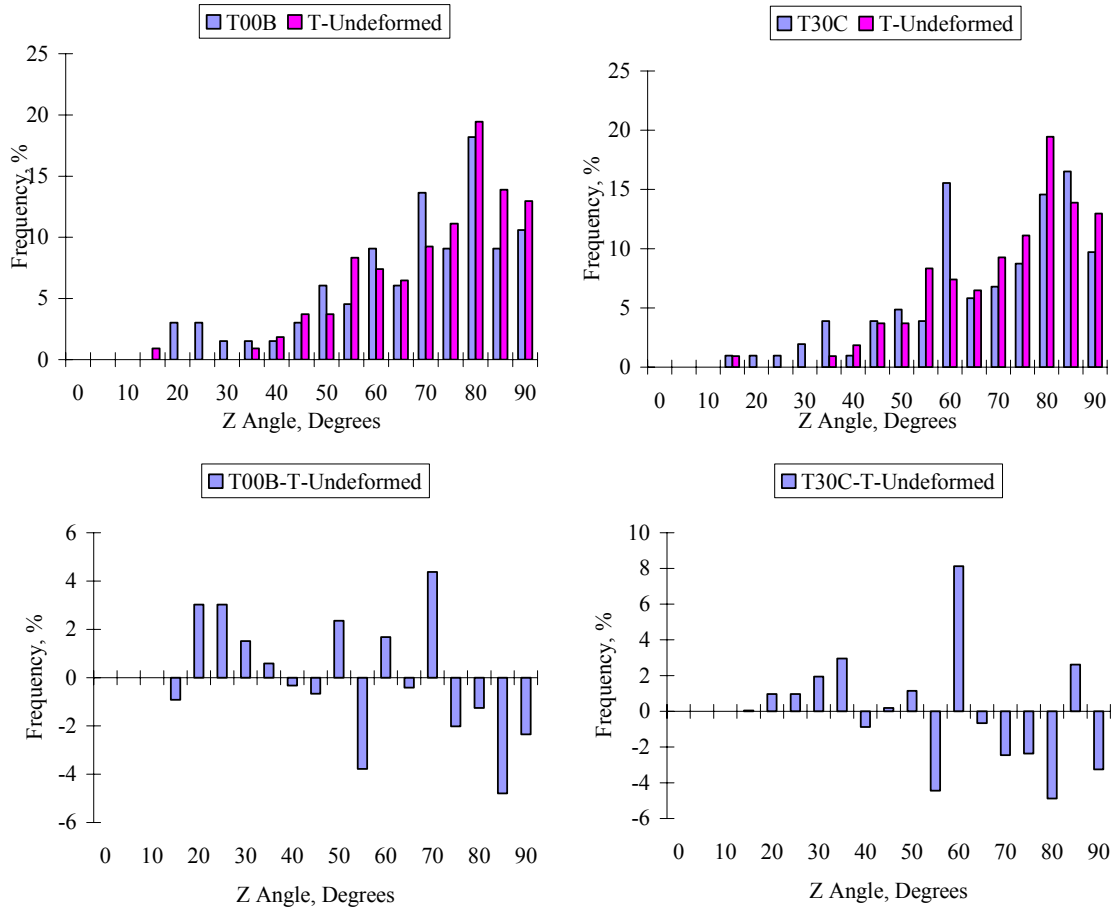

Fig. 5.5. The Percentage of Aggregate Particles with Different Orientations from the Vertical Direction Clustered at Increments of 5° for A) Comparison between Specimen T00B and T-Undeformed, B) Comparison between T30C and T-Undeformed, C) Difference in Angles (the Undeformed Subtracted from T00B Percentages), D) Difference in Angles (the Undeformed Subtracted from T30C Percentages)

Image Analysis Technique

The digital images (two-dimensional slices) were analyzed using IAT to characterize different aspects of the void properties including the void content and size (void surface area),

$$Void\ Content = \frac{\sum_{M} V}{A} \tag{5-1}$$

where V is the area of a void in an image (slice); M is the total number of voids in a slice; and A is the slice cross-sectional area. The void content gives the ratio of the total voids in a slice to the cross-sectional area of that slice. The surface area is measured by calculating the perimeter of the void multiplied by the thickness of the slice.

Image analysis techniques were used to calculate the void content and the surface area of voids for all the specimens in Table 5.1. Fig. 5.6 shows that the very first and last few slices possessed high void contents due mainly to the direct contact with the gyratory plates causing restriction in the mobility of the aggregates and reducing the efficiency of the kneading action there (Tashman et al. 2001). As pointed out by Tashman et al. (2004), the distribution in Fig. 5.6 is remarkably different than the distribution reported in a number of previous studies for 150 mm diameter and 100 mm height specimens, where the middle of the specimen was more compacted than the top and bottom portions (Masad et al. 1999, Tashman et al. 2001).

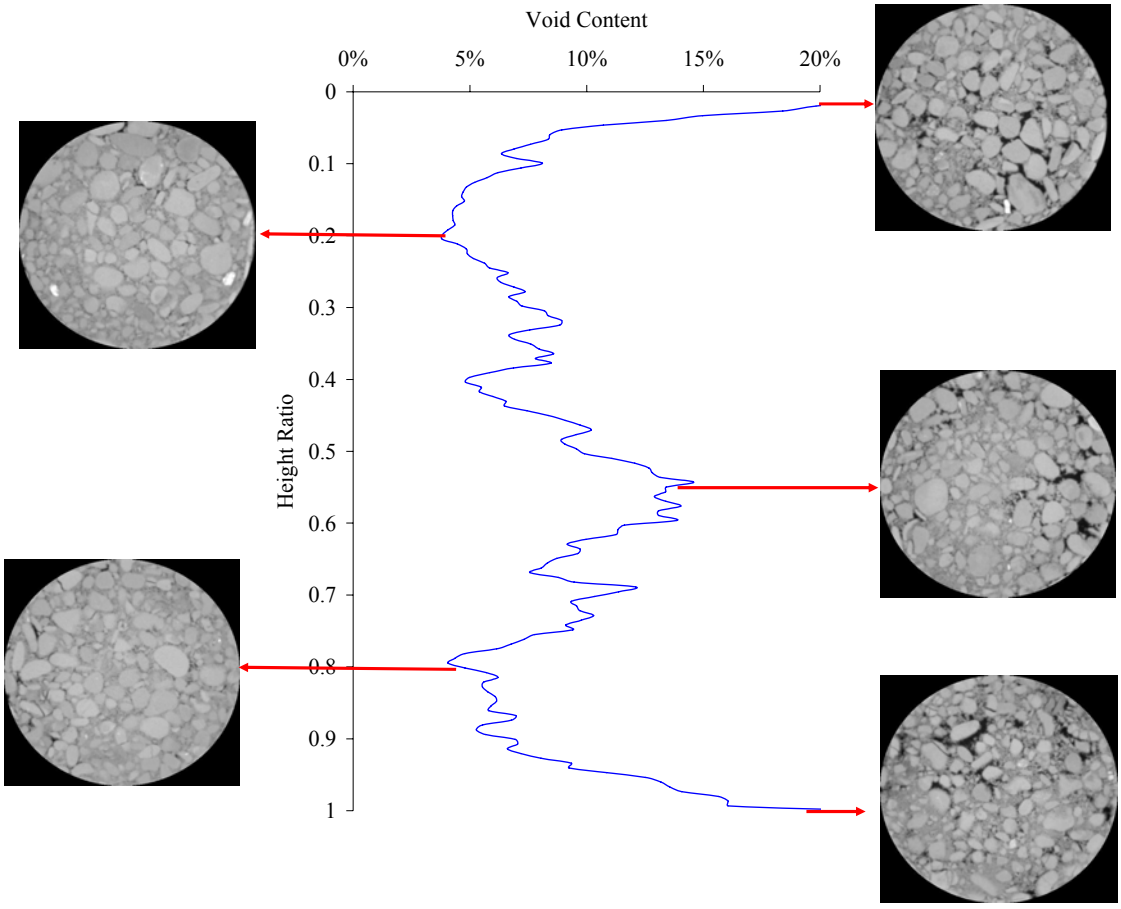

Fig. 5.6. Illustration of the Void Content in the X-ray CT Images with the Measured Air Void Content

Fig. 5.7 presents the void content and the void surface area of the gravel specimens. The height ratio along the y-axis is defined as the ratio of the vertical distance of a slice from the top of the specimen to the total height of the specimen. It was decided to use the height ratio instead of the actual depth because the deformed specimens had varying heights. It can be noticed that the void content and the void surface area are higher for the deformed tested specimens, indicating an increase in

voids content. This is in agreement with the plastic strain rate ratio as shown for the G00A specimen presented in Fig. 5.8, since the gravel would start to dilate (increase in voids volume) at a PSSR higher than 0.5, which corresponds to a viscoplastic strain of approximately 0.5. The void content in the deformed specimen at 30 psi confinement was higher than the dilation in the unconfined specimen.

Fig. 5.9 presents the void content and the void surface area for the limestone specimens tested using creep and monotonic tests. It can be seen that specimens that were tested by repeated creep test had less dilation than the one tested using monotonic constant strain rate test. This might be justified by the stress states in these two tests. The monotonic constant strain rate tests stays in contact with the specimen throughout the test, not allowing the developed cracks to heal, which results in higher dilation. Also, this test applied higher deviatoric stress compared to the repeated creep test. A higher deviatoric stress could also be responsible for dilation. The repeated creep test included rest periods were the developed cracks were allowed to heal during the rest periods. Also, monotonic tests induce continuous deformation, which causes aggregates to roll, passing each other, and encourage dilation on increase in volume. However, the rest or unloading periods in creep tests promote aggregate rearrangement and reduce aggregate structure dilation.

Fig. 5.10 presents the void content and the void surface area for the granite specimens. The deformed unconfined specimen had voids distribution similar to the undeformed specimen. In regard to the specimen deformed at 30 psi, it can be seen that the air void content behaved differently through the height of the specimen. For a height

ratio up to 0.25, there was void contraction and then it showed dilation throughout the remaining height. The PSRR presented in Chapter IV indicated that a PSSR value of 0.5 corresponded to a strain of 0.5%. This indicates that the specimens should be starting to dilate. This might be the reason why the upper height showed contraction while the lower showed contraction.

SUMMARY

This chapter utilized X-ray CT, three-dimensional image analysis software (Blob 3D), and image analysis techniques to capture and characterize the microstructure distribution.

The three-dimensional distribution of aggregate orientation was analyzed by quantifying changes in the percentage of particles oriented in different directions. As HMA specimens deformed, particles tended to have their orientation closer to the horizontal direction. This result supported that stress-induced anisotropy occurs in HMA. Particles became more oriented toward the horizontal direction with loading in the creep tests.

The change in the aggregate orientation varied for specimens tested by repeated creep from those tested by monotonic constant strain test. This evidences that the change in the internal microstructure is affected by the stress state.

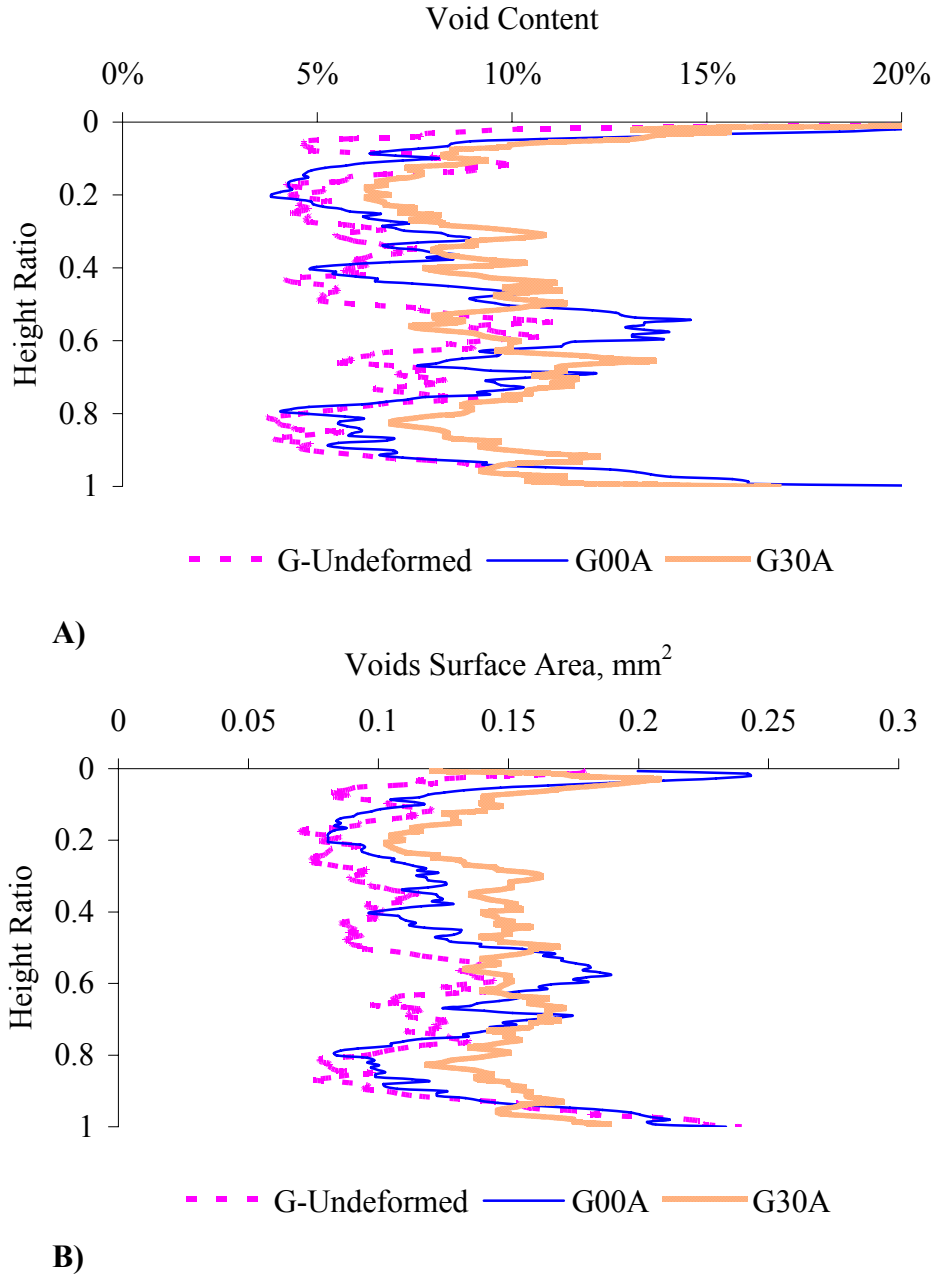

Fig. 5.7. A) Void Content and B) Void Surface Area for the Gravel Specimens

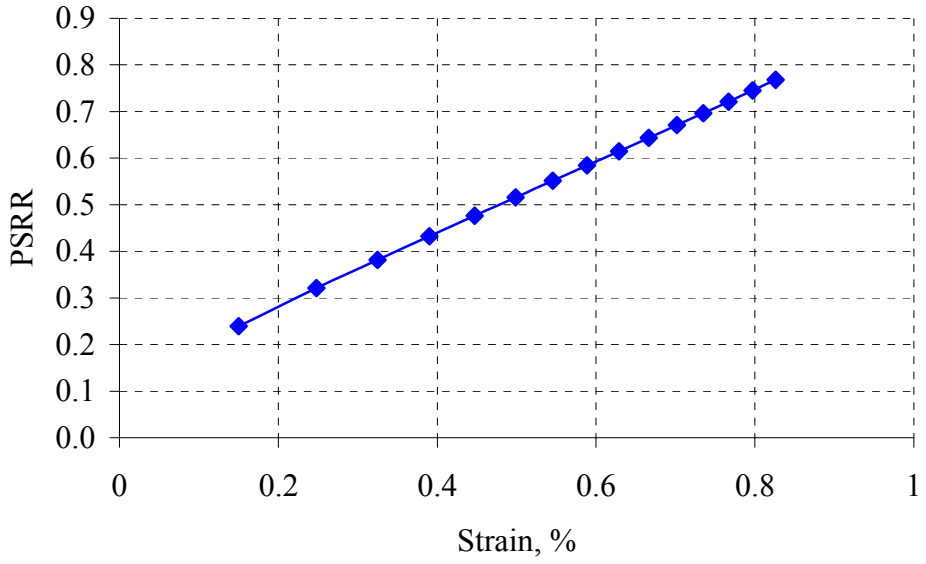

Fig. 5.8. PSRR for the G00A Specimen

The measured stress-induced anisotropy can be supported by experimental observations during creep and recovery tests. The model presented in this dissertation considers only the inherent anisotropy. As discussed in Chapter III, the viscoplastic strain rate increased after each unloading period. This was explained by the increase in anisotropy during the loading period, and consequently, an increase in mix stiffness in the vertical direction. During the unloading period, the level of anisotropy could decrease due to the recovery of the viscoelastic strain and decrease the vertical stiffness. As such, the beginning of a loading cycle would experience less stiffness and higher viscoplastic strain rate in the vertical direction compared with the stiffness at the end of the previous loading period.

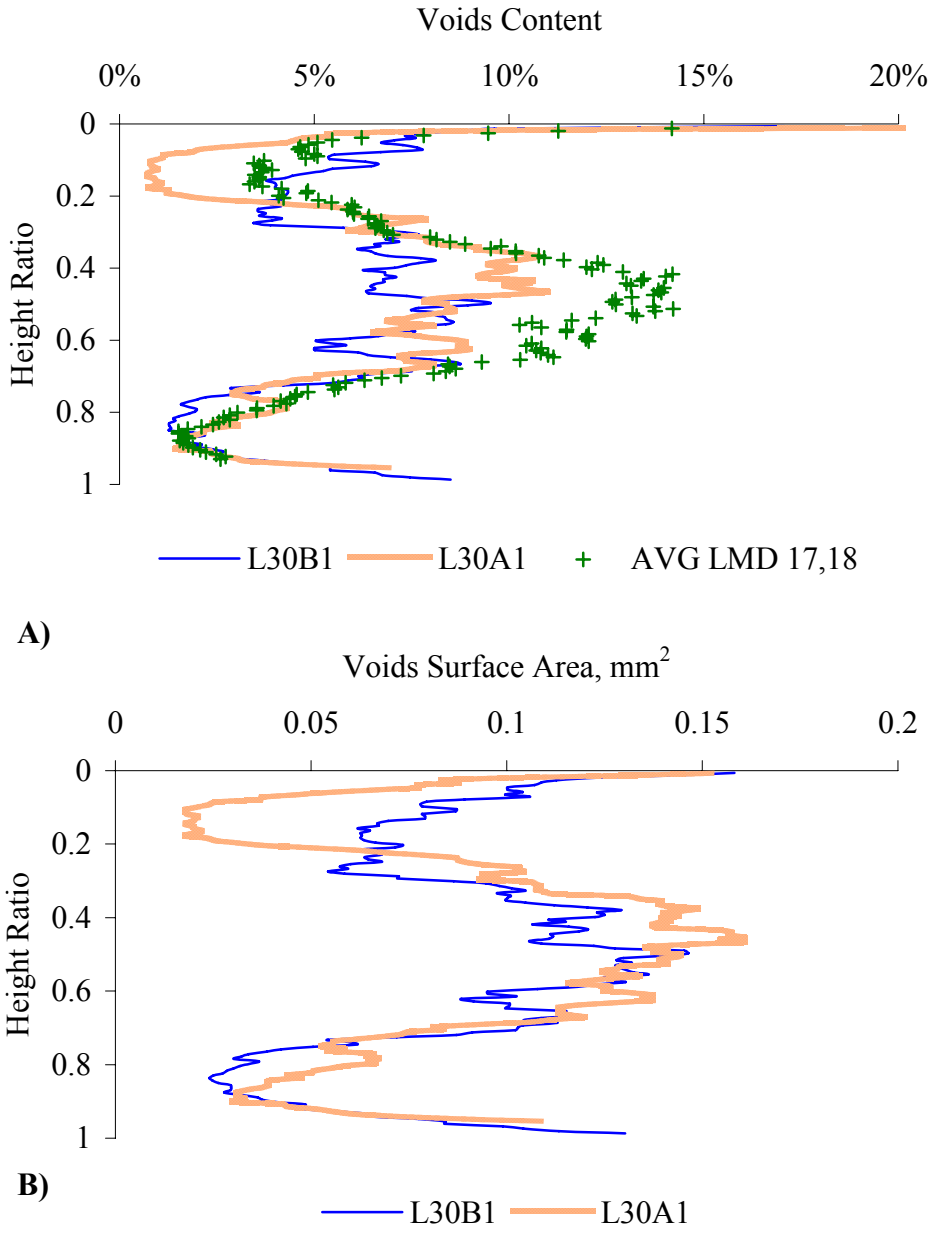

Fig. 5.9. A) Void Content and B) Void Surface Area for the Limestone Specimens

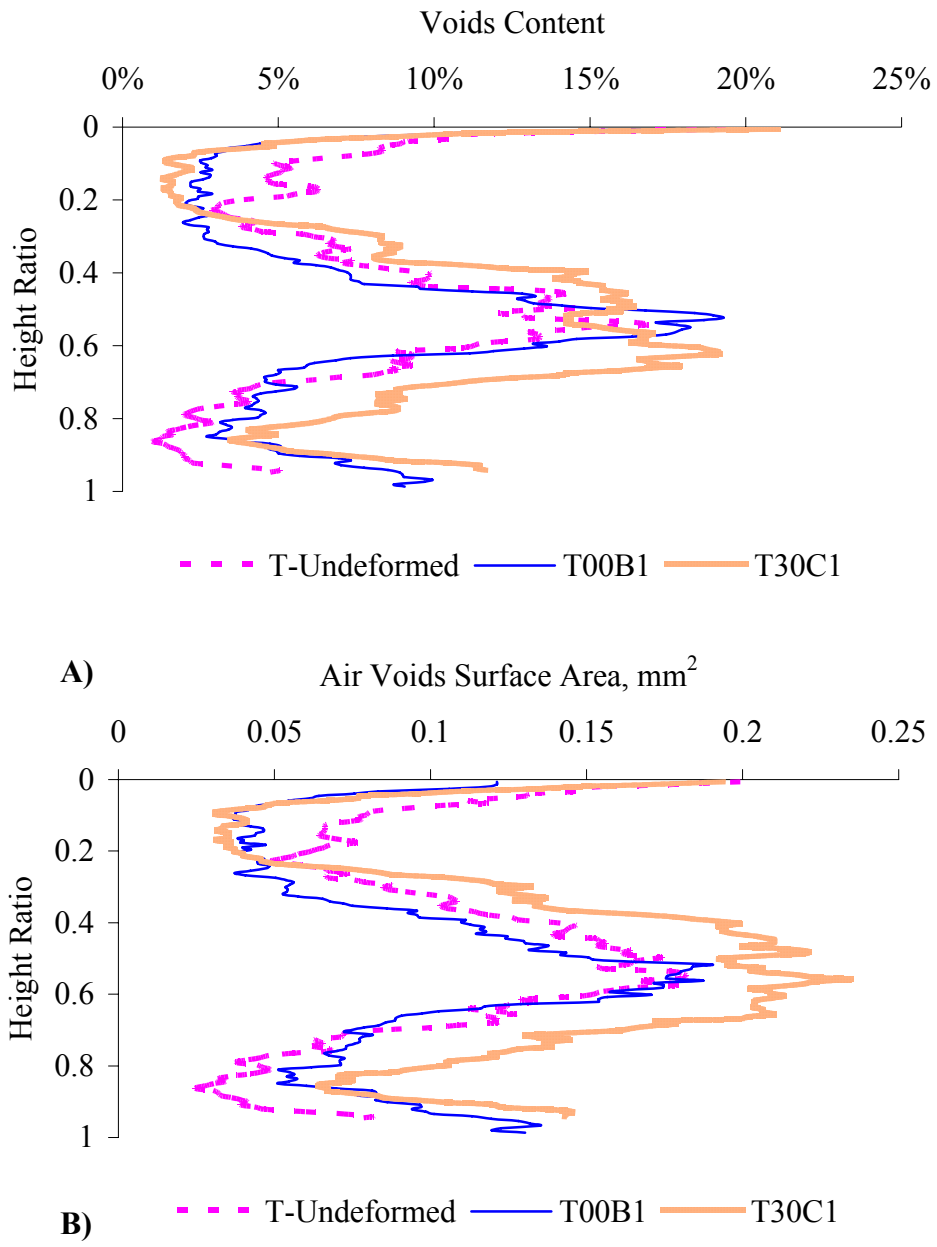

Fig. 5.10. A) Void Content and B) Void Surface Area for the Granite Specimens

The analysis of void content involved measuring percent air voids and size of air voids across a specimen thickness. Gravel specimens from repeated creep tests showed dilation at a strain level of 1%. Limestone specimens also exhibited dilation, but the dilation under repeated creep recovery tests was less than under monotonic constant strain rate tests. This indicates that the microstructure distribution is not only affected by the viscoplastic deformation but also by the stress path associated with this viscoplastic deformation. The monotonic tests do not allow for particle rearrangement and this test could induce more dilation than the creep tests that allow for particle rearrangement, during the rest period. The granite specimens exhibited contraction in the top 25% height of a specimen, while the remaining portion exhibited dilation behavior.

CHAPTER VI

CONCLUSIONS AND RECOMMENDATIONS

CONCLUSIONS

The main outcome of this study is the development of an anisotropic damage viscoelastic-viscoplastic model. This model was developed through the integration of a damage viscoelastic constitutive relationship with a viscoplastic relationship in order to capture hot mix asphalt (HMA) response and performance under a wide range of temperatures, loading rates, and stress states. The nonlinear/damage viscoelasticity model developed by Schapery (1969) was employed to present the recoverable response, and the viscoplasticity model developed at the Texas Transportation Institute (TTI) (Tashman 2003, Dessouky 2005) was improved and used to model the irrecoverable component.

This study also included the development of an experimental program capable of quantifying and decomposing HMA response. This experimental approach was used to analyze the response of HMA mixtures with different aggregate characteristics. The dynamic compression test was used to identify the material response at low strain level, from which the linear viscoelastic response of the material was determined. The linear viscoelastic properties of the three mixes (gravel, granite, and limestone) were not able to rank the three mixes based on their resistance to permanent deformation.

The repeated creep and recovery tests provided a precise response of the material at successive stages of loading and unloading. The parameters of the damage viscoelasticity component of the model were obtained from the mix response during the

unloading period. The deviation of HMA response from linear viscoelasticity was quantified using the nonlinear damage viscoelastic parameter G_2. The damage viscoelastic response in the repeated creep test could be used as an indicator of the material damage state. An increase in G_2 value is an indication of damage, while a constant G_2 value higher than 1 is an indication of the nonlinear response. The nonlinearity damage viscoelastic response was found to be more influenced by confinement for the mix with the gravel aggregates that have low angularity and texture. Also, the relationship of angularity and texture to G_2 was evident at low confinement and degraded at higher confinement levels.

The nonlinear viscoelastic response was subtracted from the total strain during loading to calculate the viscoplastic strain as a function of loading time. The effects of aggregate properties used in each mix were reflected in the viscoplastic model's parameters. This has been well pronounced in the case of the hardening, dilation, and softening parameters of the viscoplastic model. As the angularity and texture increased, the effect of confinement on hardening, dilation, and softening decreased. The relationships between the model's parameters and aggregate characteristics offer the potential to predict these parameters based on characterization of aggregate characteristics.

X-ray computed tomography (CT), three-dimensional image analysis software (Blob 3D), and image analysis techniques were shown to be powerful tools to capture and characterize HMA microstructure distribution. The characterization focused on voids

distribution and aggregate orientation due to their significant influence on HMA damage and anisotropic behavior.

The three-dimensional distribution of aggregate orientation was analyzed by quantifying changes in the percentage of particles oriented in different directions. As HMA specimens deformed, particles in the limestone mix tended to have their orientation closer to the horizontal direction. However, there was no evidence of stress induced anisotropy for the gravel and granite mixes. This result supported that stress-induced anisotropy occurs in some HMA mixes.

The measured stress-induced anisotropy can be supported by experimental observations during creep and recovery tests. The model presented in this dissertation considers only the inherent anisotropy. The viscoplastic strain rate increased after each unloading period. This was explained by the increase in anisotropy during the loading period, and consequently, an increase in mix stiffness in the vertical direction. During the unloading period, the level of anisotropy could decrease due to the recovery of the viscoelastic strain and decrease in vertical stiffness. As such, the beginning of a loading cycle would experience less stiffness and higher viscoplastic strain rate in the vertical direction compared with the stiffness at the end of the previous loading period.

The analysis of void content involved measuring percent air voids and size of air voids across a specimen thickness. It was found that mix dilation under creep and recovery tests was less than under monotonic constant strain rate tests. This indicates that the microstructure distribution is not only affected by the viscoplastic deformation but also by the stress state associated with this viscoplastic deformation.

RECOMMENDATIONS

The presented model included an anisotropic parameter to account for the directional distribution of the microstructure. The vector magnitude, which is a measure of anisotropy of the HMA, is introduced in the model to modify the stresses to reflect the influence of the direction of loading on material response. As well, its definition explains the different mixes' behaviors according to their anisotropy level. The internal microstructure analysis presented in Chapter V showed that as some HMA specimens deformed, particles tended to have their orientation closer to the horizontal direction. As a result, the stiffness in the vertical direction increased. Therefore, it is suggested to quantify the evolution of this parameter by performing an experiment in which the HMA specimens are scanned by X-ray CT before and after testing at different strain levels. Consequently, the evolution of the parameter can be incorporated in the model.

The repeated creep test provided a very good experimental method for HMA response identification. The model is calibrated in this study using the results from this test. However, the model reliability would increase if it shown that it is capable of predicting the response from different loading conditions. It is suggested to use the model parameters obtained from repeated creep tests to predict its performance under different loading conditions.

The experimental program relies on the assumption that the viscoelastic response is recovered with the same rate as it developed. This was reflected on the damage viscoelastic model by taking the g_1 parameter to be equal to unity. It is suggested to perform an experiment that would verify the validity of this assumption. This is done by

performing a creep test on HMA specimens at increasing loading intervals. Then, the viscoelastic response at each interval can be recorded and compared to the viscoelastic response of a specimen tested until the maximum strain is achieved.

The continuum model developed in this study can be easily implemented in finite element (FE). Implementing the model in FE would allow predicting the performance of pavement sections constructed using different materials and structures. In addition, it would be interesting to study the effect of the HMA material properties at the microstructural level on continuum model response at the macrostructural level.

REFERENCES

Abdulshafi, A., and Majidzadeh, K. (1984). "Combo viscoelastic-plastic modeling and rutting of asphaltic mixtures." *Transp. Res. Rec.,* 968*,* Transportation Research Board, Washington, DC, 19-31.

Bhairampally, R. K., Lytton, R. L., and Little, D. N. (2000). "Numerical and graphical method to assess permanent deformation potential for repeated compressive loading of asphalt mixtures." *Transp. Res. Rec.*, 1723, Transportation Research Board, Washington, DC, 150-158.

Bonnier, P. G. (1993). "Testing modeling and numerical analysis of the mechanical behavior of bituminous concrete." Ph.D. dissertation, Delft University of Technology, Delft, Netherlands.

Boresi P., and Schmidt R. J., (2003). *Advanced mechanics of materials*, 6th ed. John Wiley & Sons, New York.

Chehab, G. R., Kim Y. R., Schapery R. A., Witczack, M., and Bonaquist R. (2003). "Characterization of asphalt concrete in uniaxial tension using a viscoelastoplastic model" Presented at the *Association of Asphalt Paving Technologists 78th Annual Meeting* (CD ROM), Lexington, KY.

Curray, J. R. (1956). "Analysis of two dimensional orientation data." *J. of Geology*, 64, 117-131.

Dafalias, Y. F. (1990). "The plastic spin in viscoplasticity." *Int. J. Solids Struct.*, 26, 149.

Desai, C. S. (1990). *Modeling and testing: implementation of numerical models and their application in practice*. CISM Courses and Lectures, 311, Springer Verlag, New York.

Desai, C. S., Somasundaram, S., and Frantziskonis, G. (1986). "A hierarchical approach for constitutive modeling of geologic materials." *Int. J. Numer. Analy. Meth. Geomech.*, 10, 225-257.

Desai, C. S., and Zhang, D. (1987). "Viscoplastic model for geologic materials with generalized flow rule." *Int. J. Numer. Analy. Meth. Geomech.*, 11, 603-620.

Dessouky, S., (2005). "Multiscale approach for modeling hot mix asphalt" PhD dissertation, Texas A&M University, College Station, TX.

Ferry, J. D.(1980). *Viscoelastic properties of polymers*, 3rd ed., Wiley, New York.

Kachanov, L. M. (1958). "On creep fracture time." *Izv. Akad. Nauk USSR Otd. Tekh.* 8, 26-31 (in Russian).

Kaloush, K. (2001). "Simple performance test for permanent deformation of asphalt mixtures," Ph.D. dissertation, Arizona State University, Tempe, AZ.

Ketcham, R. A., and Shashidhar, N. (2001). "Quantitative analysis of 3-D images of asphalt concrete," Paper No. 01-0321. *Transportation Research Board 80th Annual Meeting*. Transportation Research Board, Washington, DC.

Kim, Y. R., Lee, H. -J., and Little, D. (1997). "Fatigue characterization of asphalt concrete using viscoelasticity and continuum damage theory." *J. Assoc. Asphalt Paving Technologists*, 66, 520-569.

Kim, Y. R., and Little, D. N., (1990). "One-Dimensional constitutive modeling of asphalt concrete." *J. Eng. Mech.*, 116, 751-772.

Landis, E., and Keane, D. (1999). "X-ray microtomography for fracture studies in cement-based materials." *Int. Soc. Optical Eng.*, 3772, 105-113.

Lee, H. J. and Kim, Y. R. (1990). "A viscoelastic continuum damage model of asphalt concrete with healing." *J. Eng. Mech.*, 124, 1-9.

Little, D., Lytton, R., Williams, D., and Kim, Y. R. (1999). "An analysis of the mechanism of microdamage healing based on the application of micromechanics first principles of fracture and healing." *J. Assoc. Asphalt Paving Technologists*, 68, 501-542.

Lytton, R. (2000). "Characterizing asphalt pavements for performance." *Transp. Res. Rec.* 1723*,* Transportation Research Board, Washington, DC, 5-16.

Lytton, R., Uzan, J., Fernando, E. G., Roque, R., Hiltunen, D., Stoffels, S. M. (1993). "Development and validation of performance prediction models and specifications for asphalt binders and paving mixes." *The Strategic Highway Research Program Report No. SHRP-A-357*, National Research Council, Washington, DC.

Masad, E. (2003). The Development of a Computer Controlled Image Analysis System for Measuring Aggregate Shape Properties. *NCHRP-IDEA Project 77 Final Report*, Transportation Research Board, Washington, DC.

Masad, E. (2004). "X-ray computed tomography of aggregates and asphalt mixes." *Mater. Eval. J., Am. Soc. Nondestructive Testing,* 62, 775 – 783.

Masad, E., Jandhyala, V. K., Dasgupta, J., Somadevan, N., and Shashidhar, N. (2002a). "Characterization of air void distribution in asphalt mixes using X-ray CT." *J. Mat. Civil Eng.*, 14, 122-129.

Masad, E., Little, D., Tashman, L., Saadeh, S., Al-Rousan, T., and Sukhwani, R. (2003). "Evaluation of aggregate characteristics affecting HMA concrete performance." *Research Report ICAR 203-1*, Texas Transportation Institute, College Station, TX.

Masad, E., Muhunthan, B., Shashidhar, N., and Harman T. (1999). "Internal structure characterization of asphalt concrete using image analysis." *J. Comput. Civil Eng. (Special Issue on Image Processing*), 13, 88-95.

Masad, E., Tashman, L., Little, D., and Zbib, H. (2005). "Viscoplastic modeling of asphalt mixes with the effects of anisotropy, damage and aggregate Characteristics." *J. Mech. Mat.*, 37, 1242-1256.

Masad, E., Tashman, L., Niranjanan, S., and Little, D. (2002b). "Micromechanics-based analysis of stiffness anisotropy in asphalt mixtures," *J. Mat. Civil Eng.*, 14, 374 - 383.

Moore, D. F. (1993). *Viscoelastic machine element*. Butterworth-Hienmann, New York.

Park, S. W., Kim, Y. R., and Schapery, R. A. (1996). "A viscoelastic continuum damage model and its application to uniaxial behavior of asphalt concrete." *Mech. Mat.*, 24, 241-255.

Perl, M., Uzan, J., and Sides, A. (1983). "Visco-elasto-plastic constitutive law for bituminous mixture under repeated loading." *Transp. Res. Rec.,* 911, Transportation Research Board, Washington, DC, 20-26.

Saadeh, S. (2002). "Comparative analysis of axial and shear moduli of asphalt mixes," M. S. Thesis, Washington State University, Pullman, WA.

Scarpas, A., Al-Khoury, R., Van Gurp, C., and Erkens, S. M. (1997). "Finite element simulation of damage development in asphalt concrete pavements." *Proc. 8th Int. Conf. Asphalt Pavements*, University of Washington, Seattle, 673-692.

Schapery, R. A. (1969). "On the characterization of non-linear viscoelastic materials." *Polymer Eng. Science*, 9(4), 295-310.

Schapery, R. A. (1984). "Correspondence principles and a generalized J integral for large deformation and fracture analysis of viscoelastic media." *Int. J. Fracture*, 25, 195-223.

Schapery, R. A. (1999). "Nonlinear viscoelastic and viscoplastic constitutive equations with growing damage." *Int. J. Fracture*, 97, 33-66.

Schwartz, C. W., Gibson, N. H., Schapery, R. A., and Witczak, M. W. (2004). "Viscoplasticity modeling of asphalt concrete behavior." *Geotech. Spec. Publ.*, 123, 144-159.

Shi, B., Murakami, Y., Wu, Z., Chen, J., and Inyang, H. (1999). "Monitoring of internal failure evolution in soils using computerization x-ray tomography." *J. Eng. Geol.*, 54(3-4), 321-328.

Si, Z., Little, D. N. P. Lytton, R. L. P. (2002). "Characterization of microdamage and healing of asphalt concrete mixtures." *J. Mat. Civil Eng.*, 14, 461-470.

Sides, A., Uzan, J., and Perl, M. (1985). "A comprehensive visco-elastoplastic characterization of sand-asphalt under compression and tension cyclic loading." *J. Testing Eval.*, 13, 59-59.

Slaughter, W. S., (2002). *The linearized theory of elasticity*, Brikhauser, Boston.

Sousa, J. B., and Weissman, S. (1994). "Modeling permanent deformation of asphalt concrete mixtures." *J. Assoc. Asphalt Paving Technologists*, 63, 224-257.

Sousa, J. B., Weissman, S., Sackman, J., and Monismith, C. L. (1993). "A nonlinear elastic viscous with damage model to predict permanent deformation of asphalt concrete mixtures." *Transp. Res. Rec.*, 1384, Transportation Research Board, Washington, DC, 80-93.

Synolakis, C. E., Zhou, Z., and Leahy, R. M. (1996). "Determination of internal deformation field in asphalt cores using X-ray computer tomography." *Transp. Res. Rec.*, 1526, Transportation Research Board, Washington, DC, 135-141.

Tashman, L. (2003). "Microstructure viscoplastic continuum model for permanent deformation in asphalt pavements." Ph.D. Dissertation, Texas A&M University, College Station, TX.

Tashman, L., Masad, E., Little, D., and Lytton, R. (2004). "Damage evolution in triaxial compression tests of HMA at high temperatures." *J. Assoc. Asphalt Paving Technologists*, 73, 53 - 81.

Tashman, L., Masad, E., Peterson, B., and Saleh, H. (2001). "Internal structure analysis of asphalt mixes to improve the simulation of Superpave gyratory compaction to field conditions." *J. Assoc. Asphalt Paving Technologists*, 70, 605-645.

Tobita, Y., and Yanagisawa, E. (1988). "Contact tensor in constitutive model for granular materials." *Micromech. Granular Mat.*, Elsevier Science Publishers, Amsterdam, 263-270.

Tschoegl, N.W. (1989). *The phenomenological theory of linear viscoelastic behavior*, Berlin, Springer-Verlag.

Uzan, J. (1996). "Asphalt concrete characterization for pavement performance prediction." *J. Assoc. Asphalt Paving Technologists*, 65, 573-607.

Wang, L. B., Frost, J. D., and Shashidhar, N. (2001). "Microstructure study of Westrack mixes from X-ray tomography images." *Transp. Res. Rec.*, 1767, Transportation Research Board, Washington, DC, 85-94.

Witczak, M. W., and Pellinen, T. (2000). "E*-dynamic complex modulus and ed-dynamic pulse wave velocity tests." NCHRP Project 9-19, Task C. Team Report SPT-ALF-2(J-K) ALF Experiment, Arizona State University, Tempe.

Young, J. F., Mindess, S., Gary, R., and Bentur, A. (1998). *The science and technology of civil engineering materials*, Prentice-Hall, Inc., New Jersey.

APPENDIX

DAMAGE VISCOELASTIC AND VISCOPLASTIC MODEL FIGURES

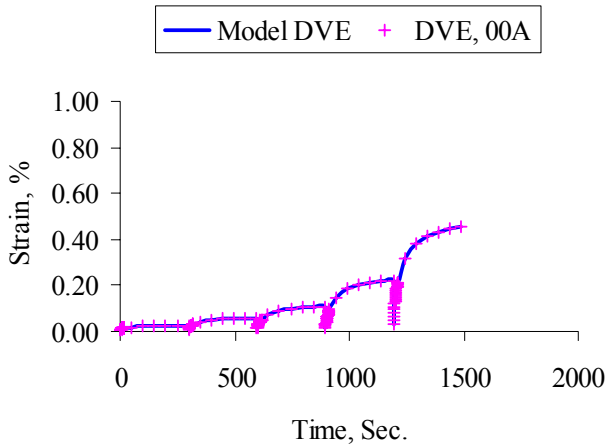

A)

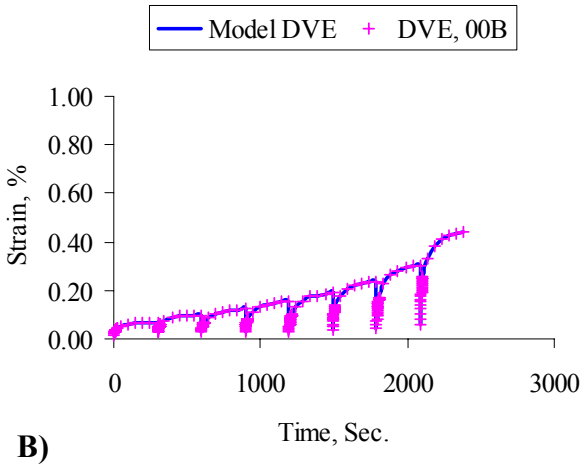

B)

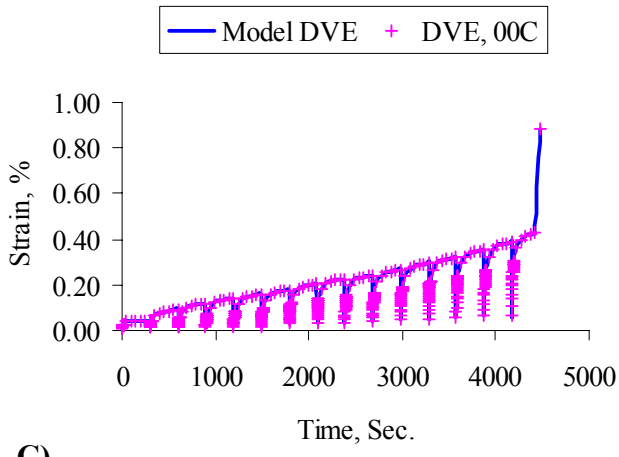

C)

Fig. A.1. Experimental and Modeled Damage Viscoelastic Strain for Gravel Mix at A) High, B) Medium, and C) Low Axial Stress Level and 0 psi Confinement

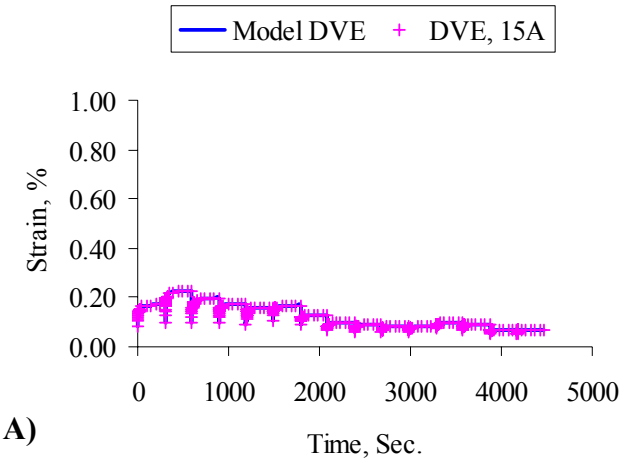

A)

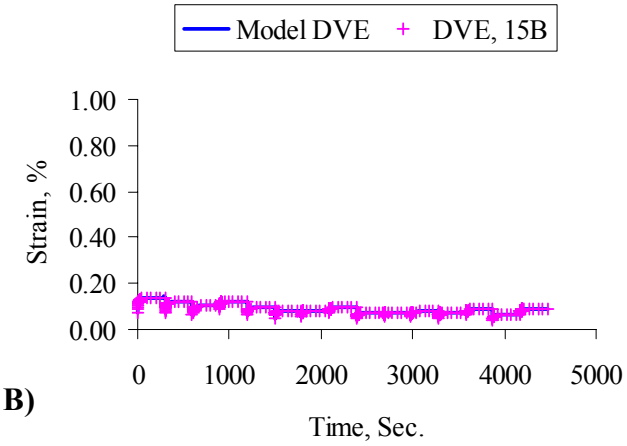

B)

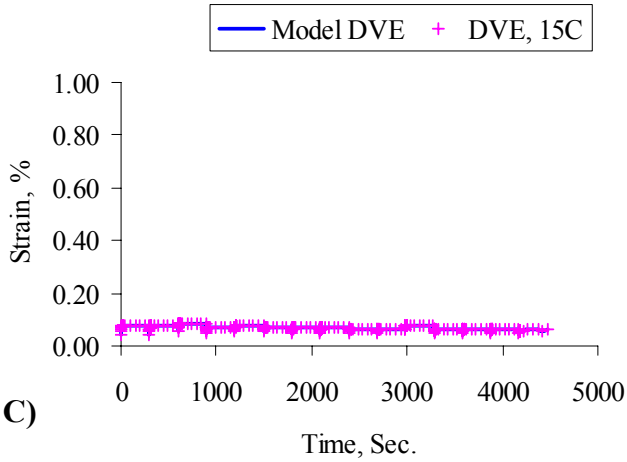

C)

Fig. A.2. Experimental and Modeled Damage Viscoelastic Strain for Gravel Mix at A) High, B) Medium, and C) Low Axial Stress Level and 15 psi Confinement

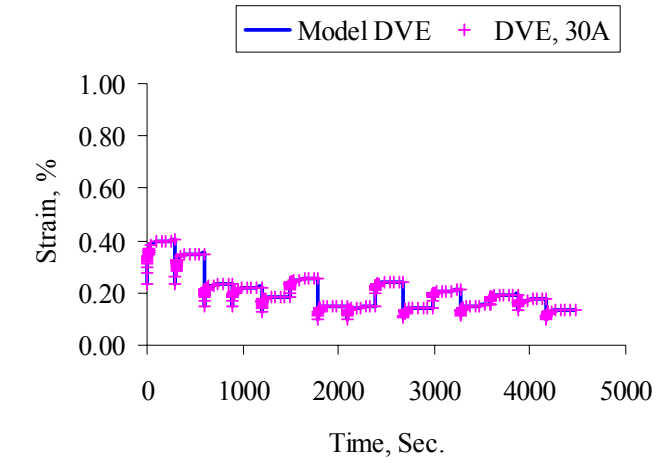

A)

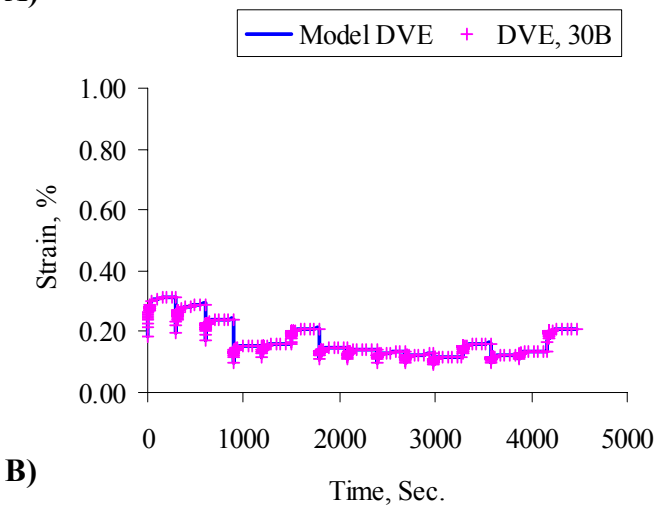

B)

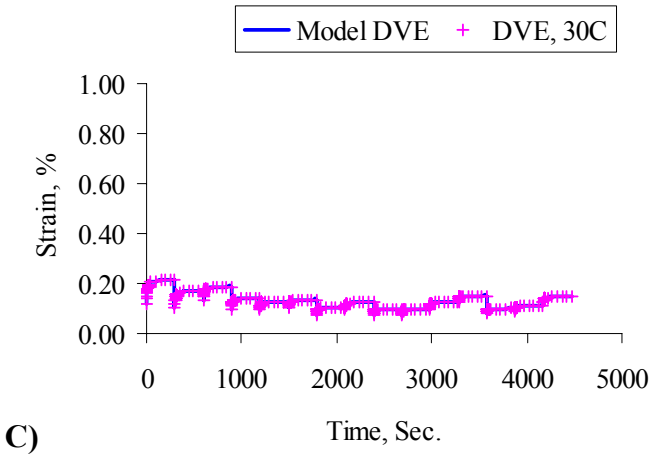

C)

Fig. A.3. Experimental and Modeled Damage Viscoelastic Strain for Gravel Mix at A) High, B) Medium, and C) Low Axial Stress Level and 30 psi Confinement

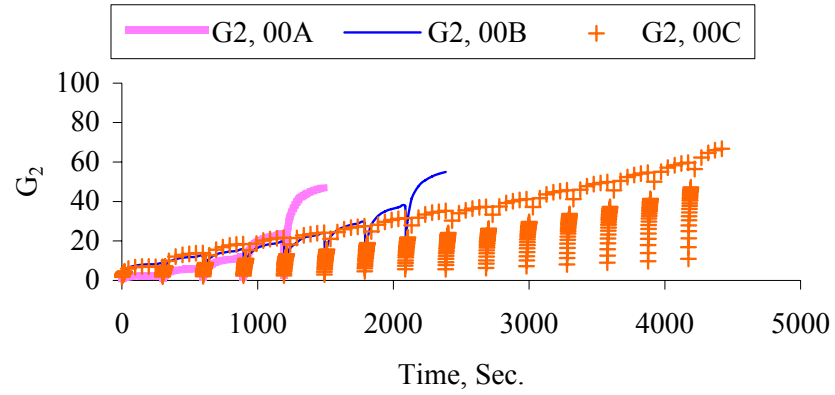

A)

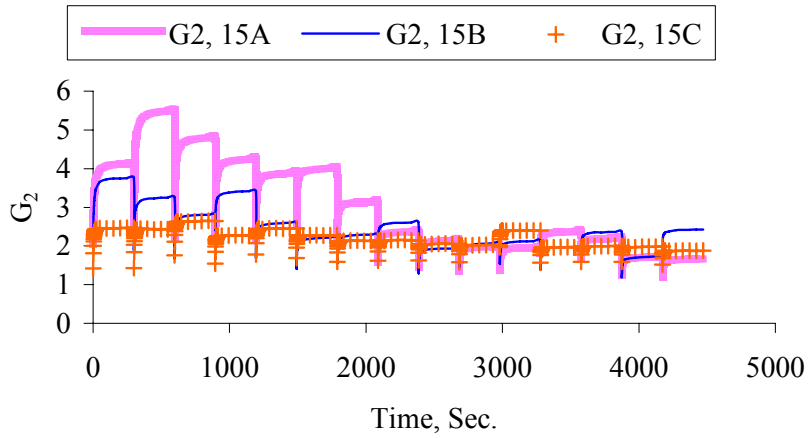

B)

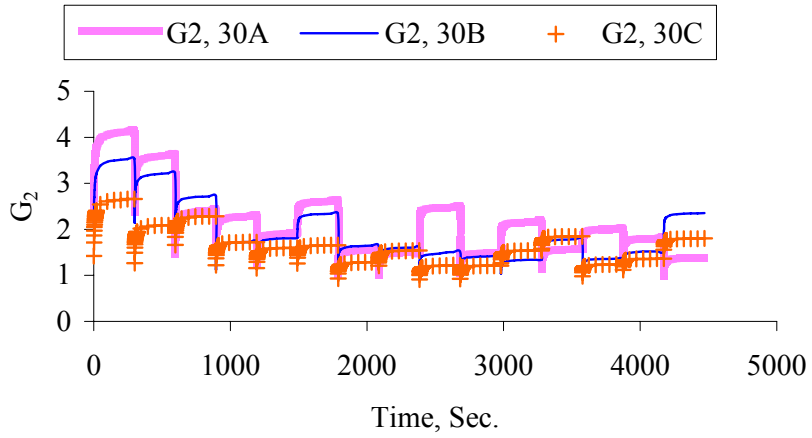

C)

Fig. A.4. Nonlinearity Damage Parameter for the Gravel Mix at A) 0, B) 15, and C) 30 psi Confinement

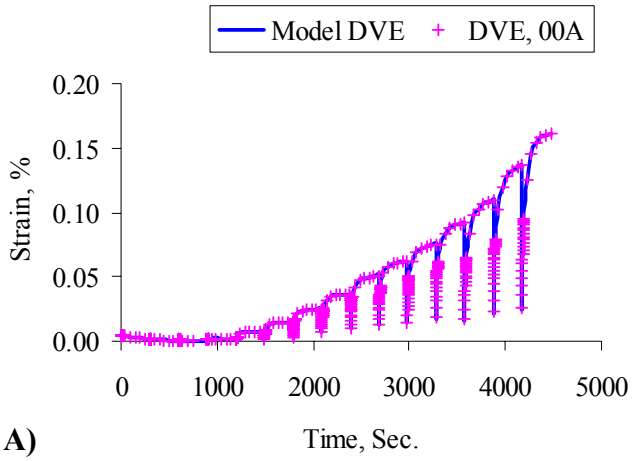

A)

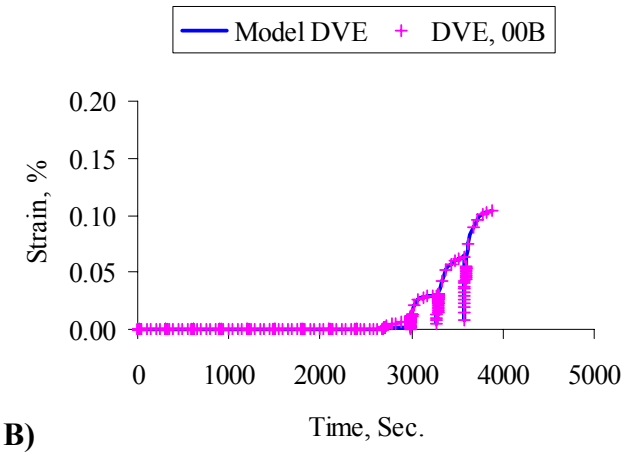

B)

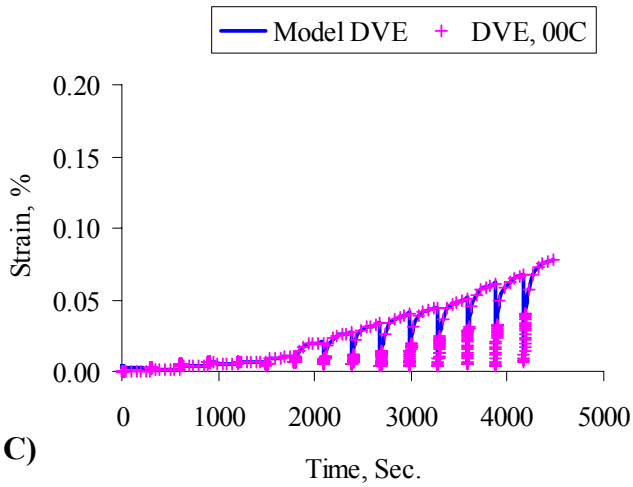

C)

Fig. A.5. Experimental and Modeled Damage Viscoelastic Strain for Limestone Mix at A) High, B) Medium, and C) Low Axial Stress Level and 0 psi Confinement

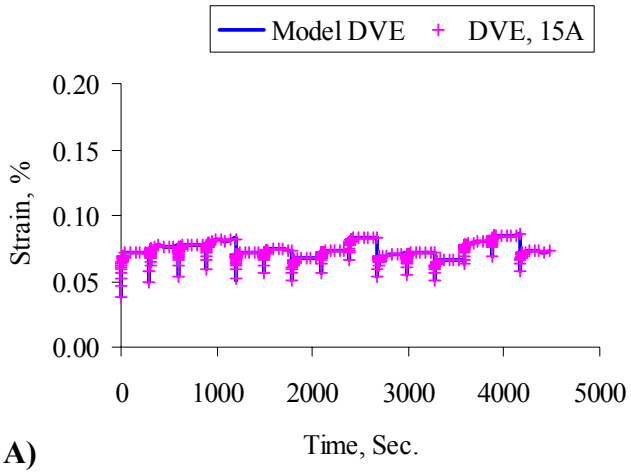

A)

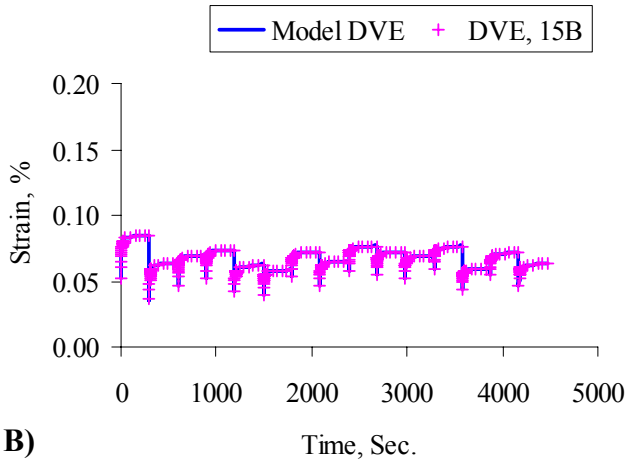

B)

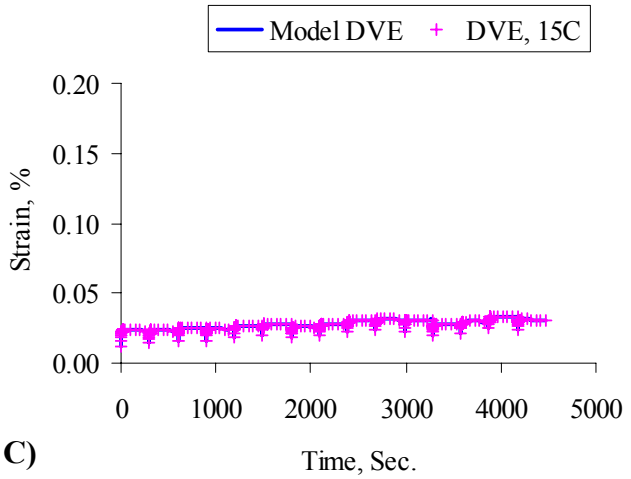

C)

Fig. A.6. Experimental and Modeled Damage Viscoelastic Strain for Limestone Mix at A) High, B) Medium, and C) Low Axial Stress Level and 15 psi Confinement

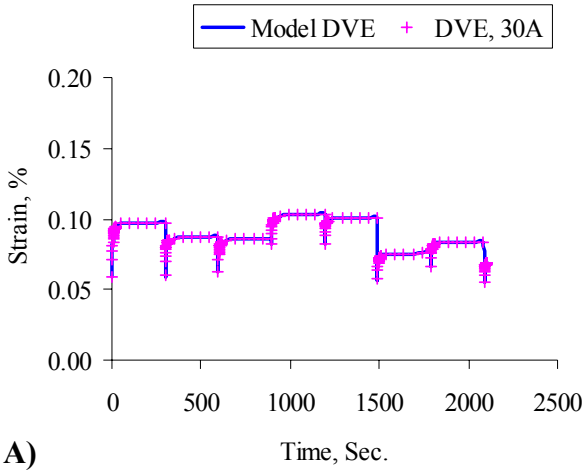

A)

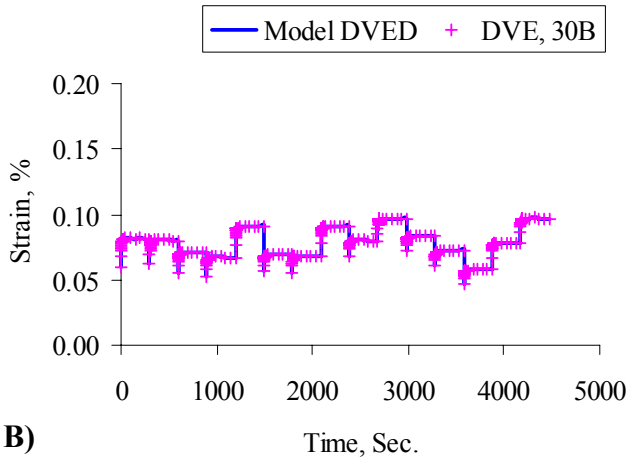

B)

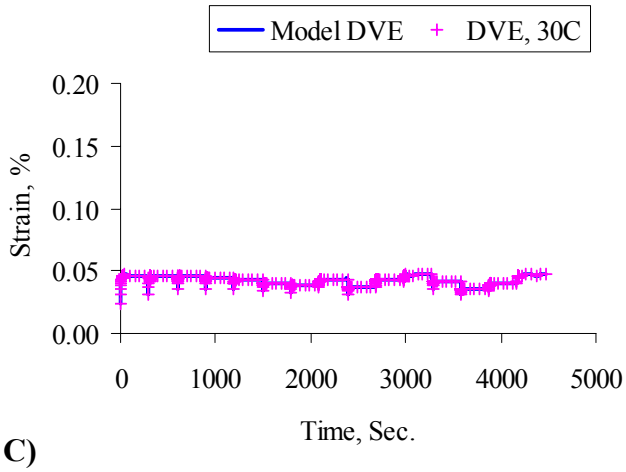

C)

Fig. A.7. Experimental and Modeled Damage Viscoelastic Strain for Limestone Mix at A) High, B) Medium, and C) Low Axial Stress Level and 30 psi Confinement

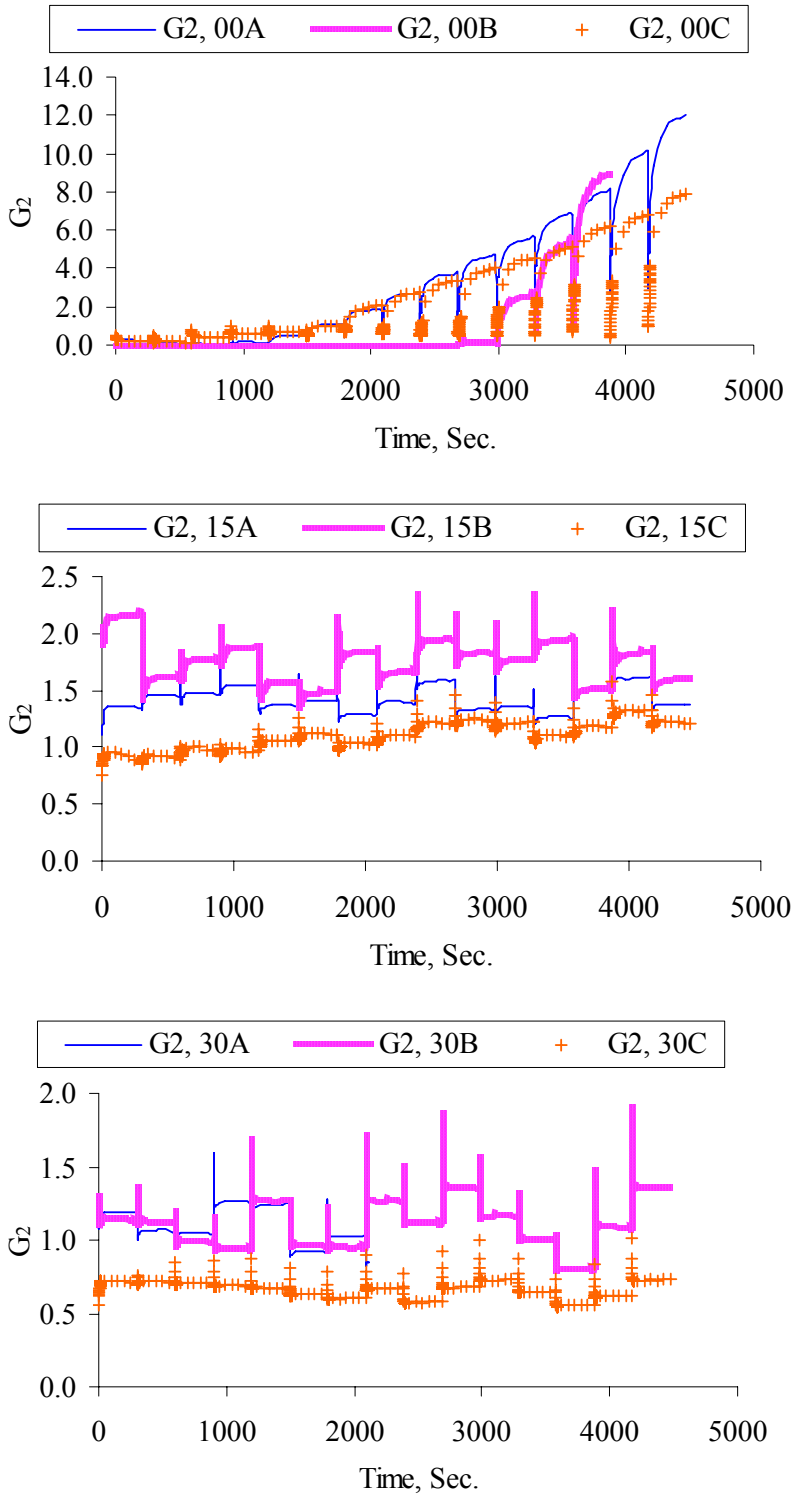

Fig. A.8. Nonlinearity Damage Parameter for the Limestone Mix at A) 0, B) 15, and C) 30 psi Confinement

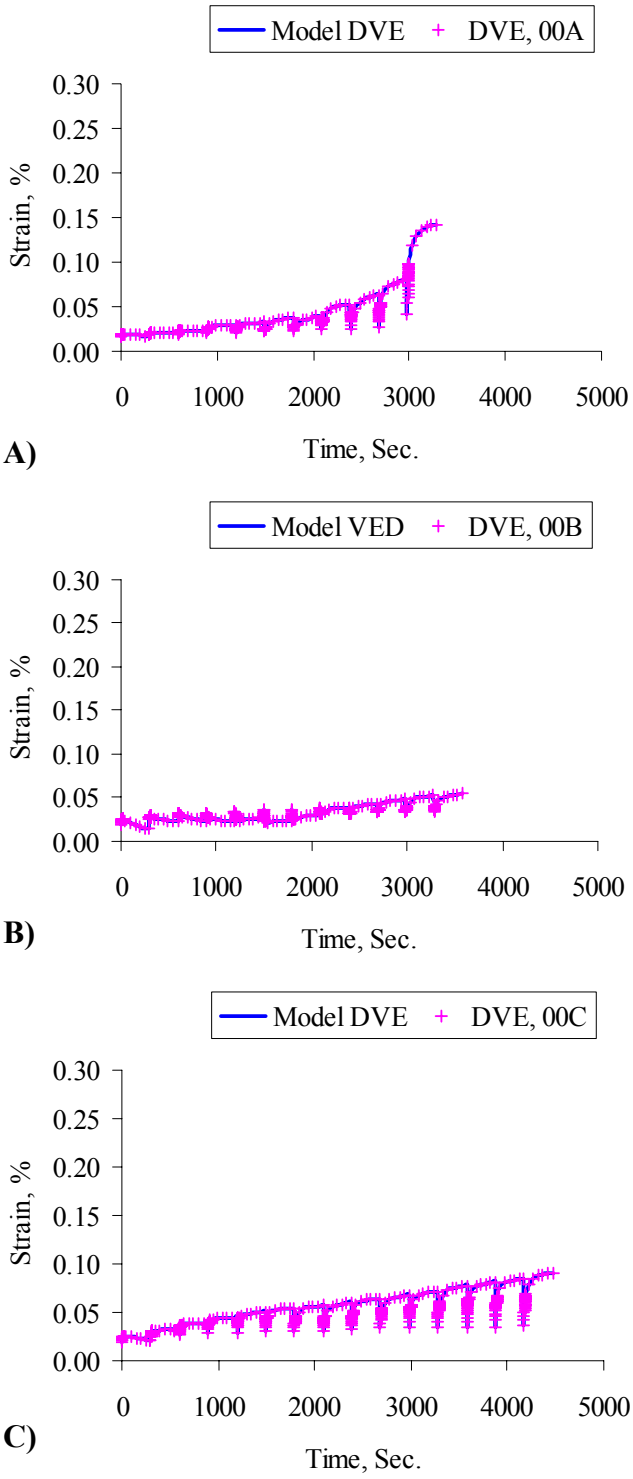

Fig. A.9. Experimental and Modeled Damage Viscoelastic Strain for Granite Mix at A) High, B) Medium, and C) Low Axial Stress Level and 0 psi Confinement

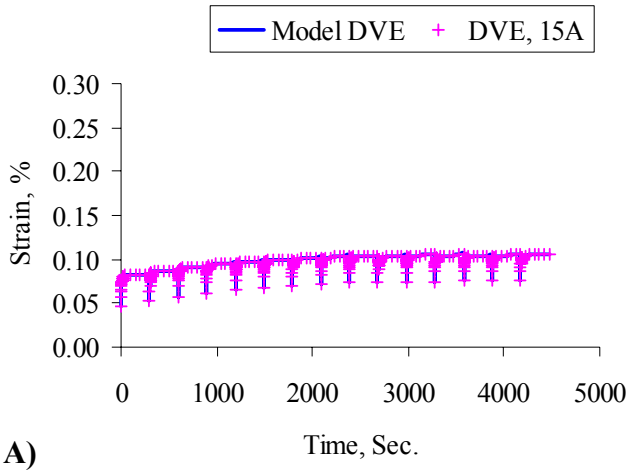

A)

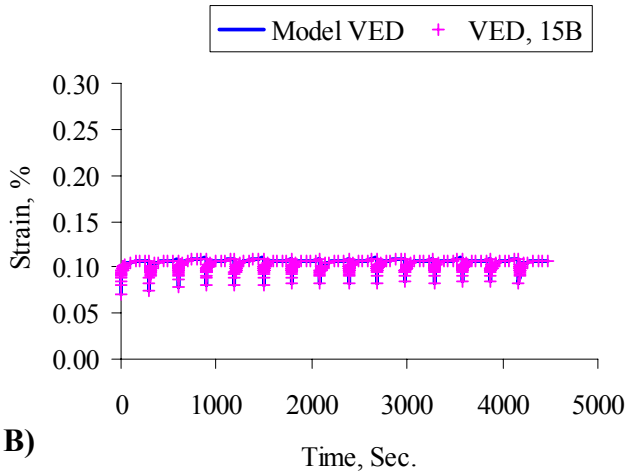

B)

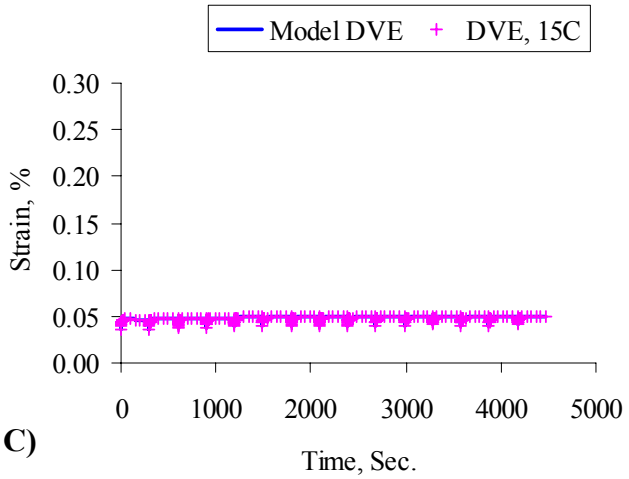

C)

Fig. A.10. Experimental and Modeled Damage Viscoelastic Strain for Granite Mix at A) High, B) Medium, and C) Low Axial Stress Level and 15 psi Confinement

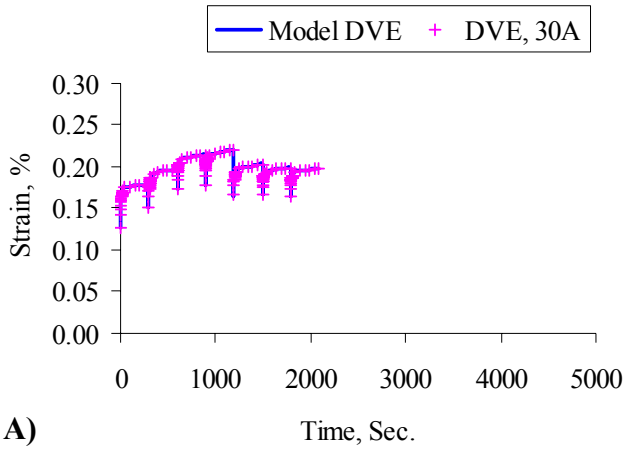

A)

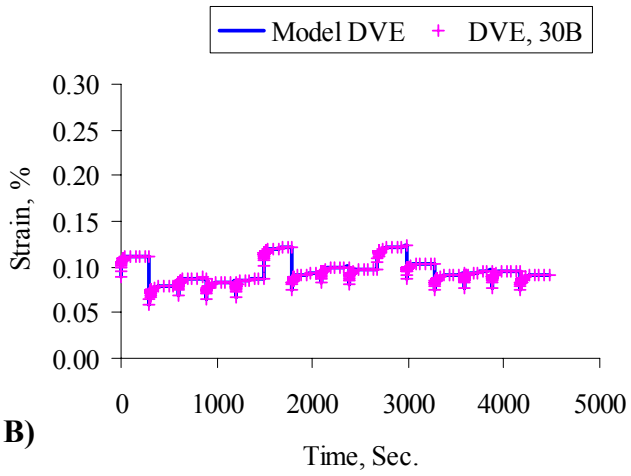

B)

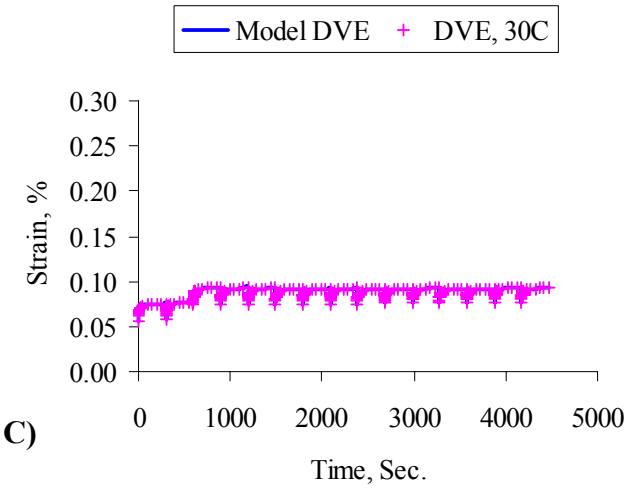

C)

Fig. A.11. Experimental and Modeled Damage Viscoelastic Strain for Granite Mix at A) High, B) Medium, and C) Low Axial Stress Level and 30 psi Confinement

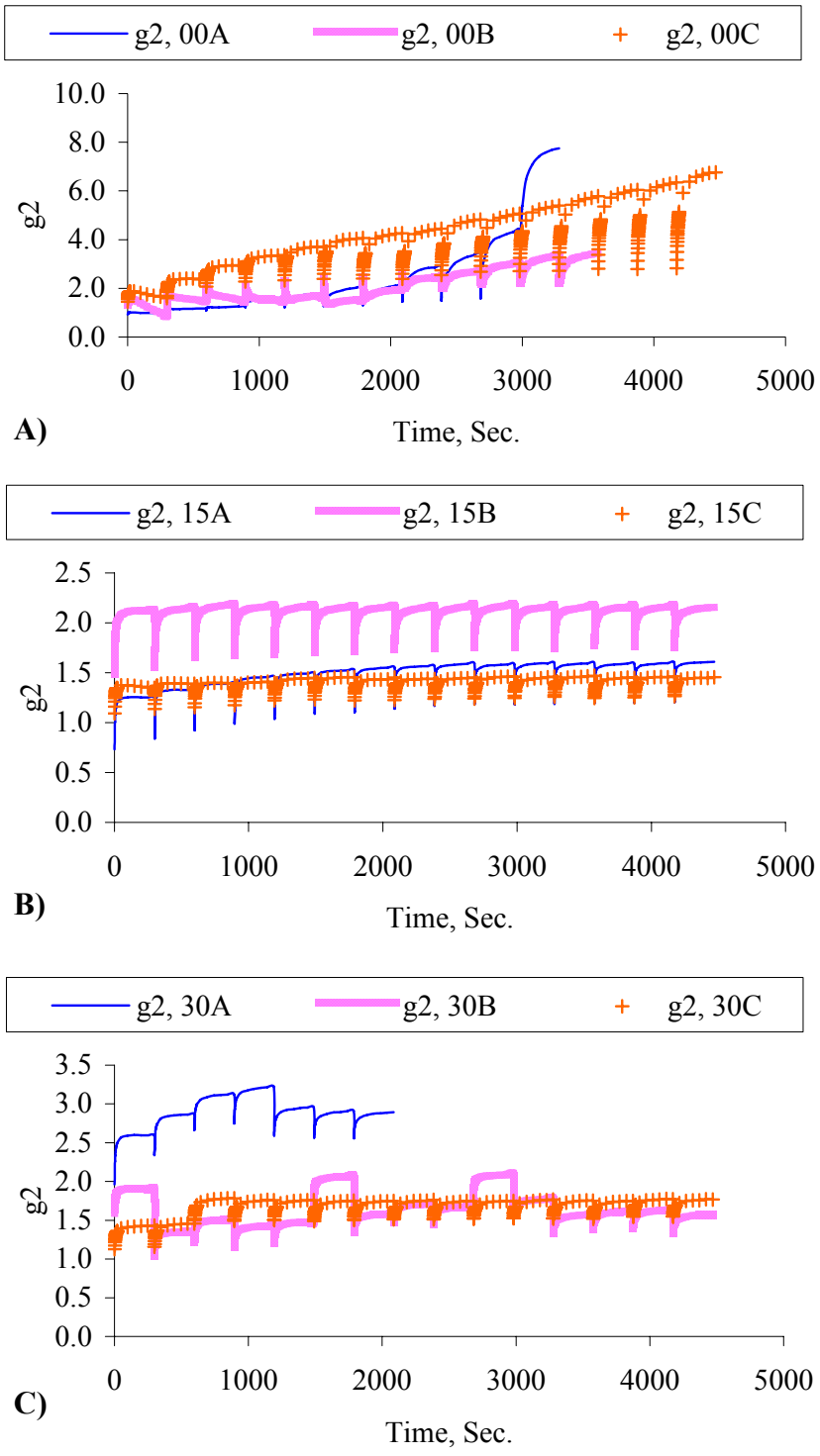

Fig. A.12. Nonlinearity Damage Parameter for the Granite Mix at A) 0, B) 15, and C) 30 psi Confinement

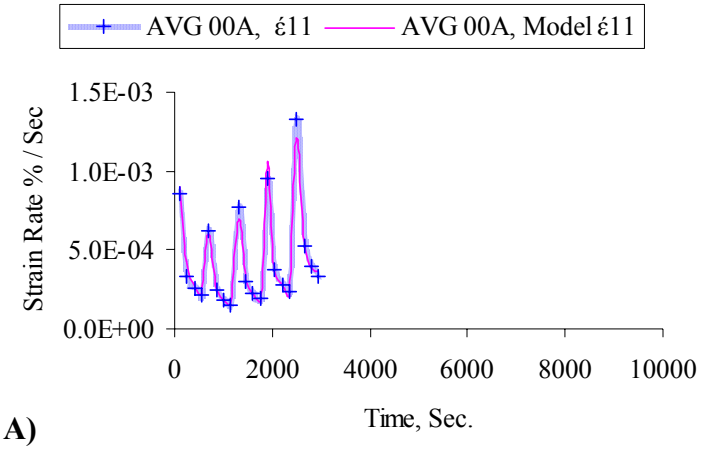

A)

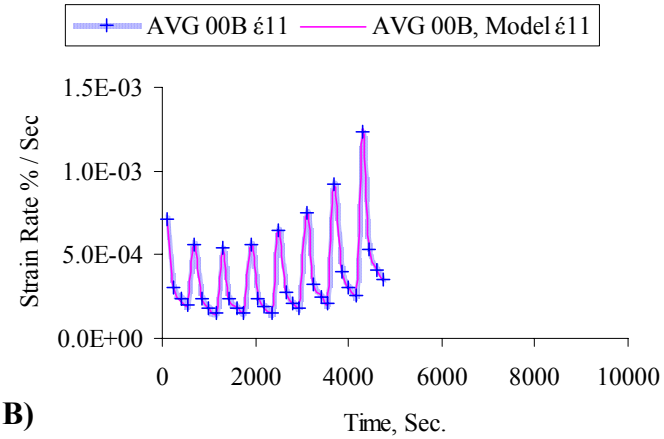

B)

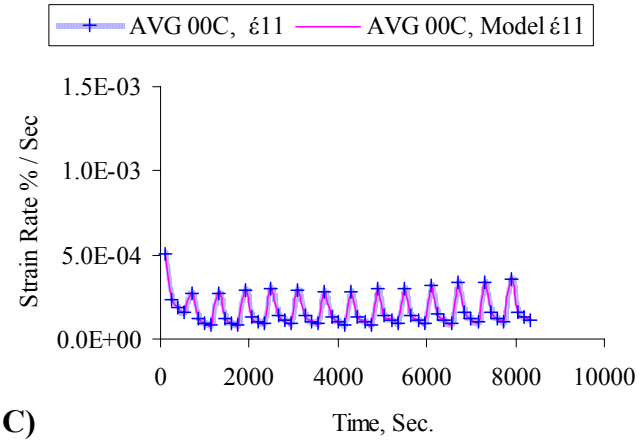

C)

Fig. A.13. Experimental Strain Rate and Model Strain Rate for the Gravel Mix at A) High, B) Medium, and C) Low Stress Levels and 0 psi Confinement

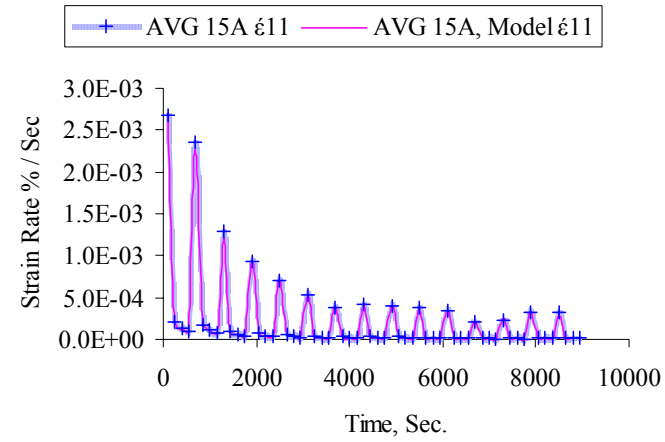

A)

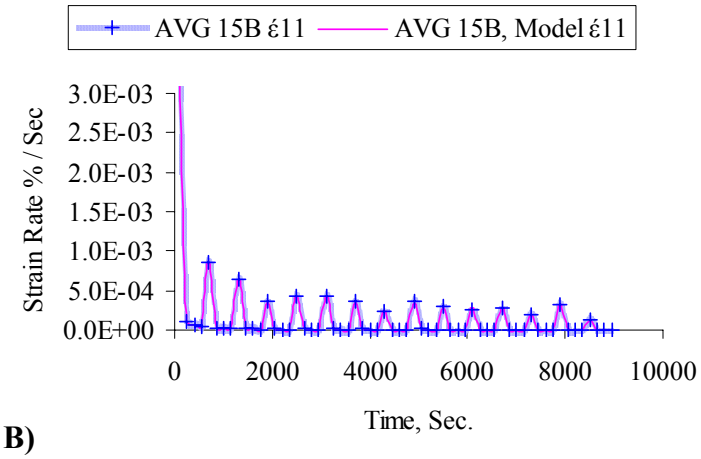

B)

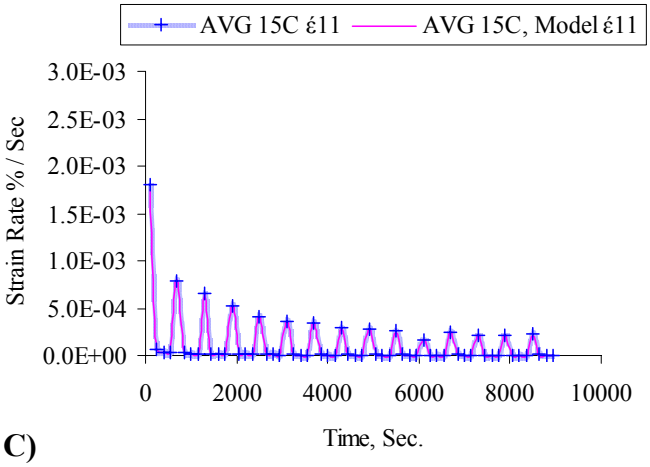

C)

Fig. A.14. Experimental Strain Rate and Model Strain Rate for the Gravel Mix at A) High, B) Medium, and C) Low Stress Levels and 15 psi Confinement

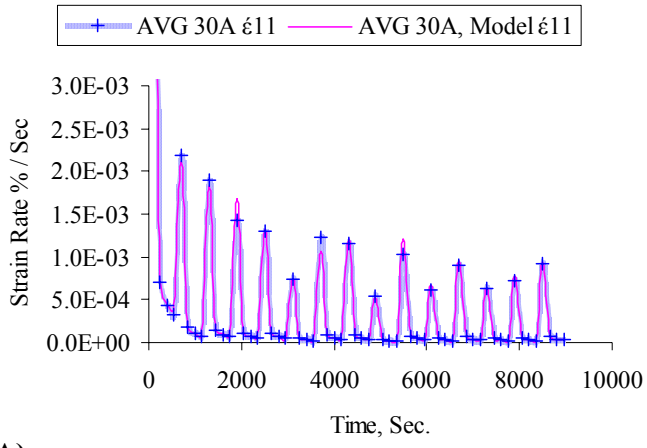

A)

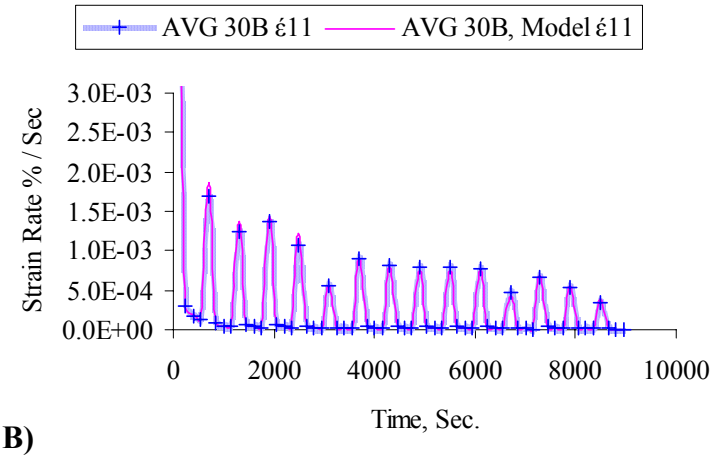

B)

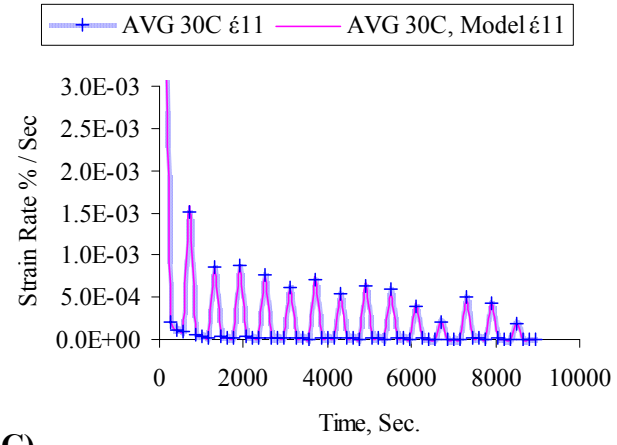

C)

Fig. A.15. Experimental Strain Rate and Model Strain Rate for the Gravel Mix at A) High, B) Medium, and C) Low Stress Levels and 30 psi Confinement

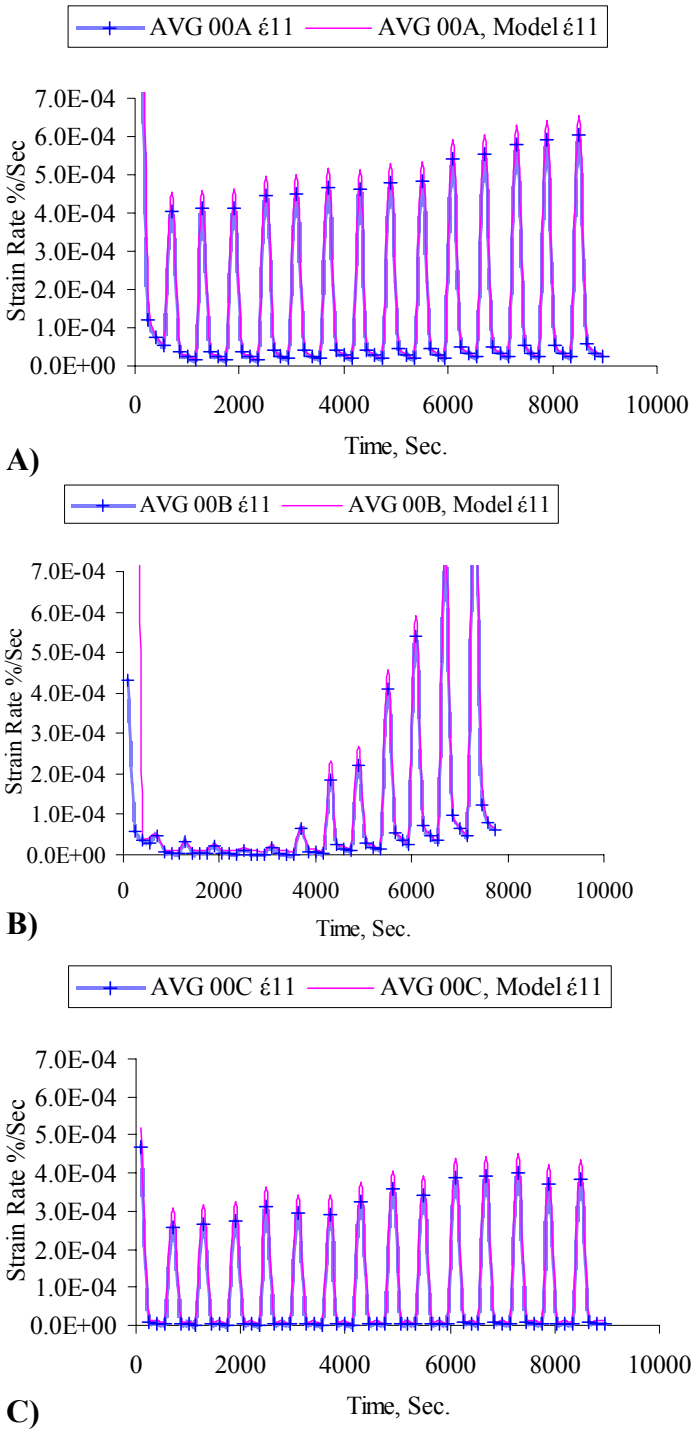

Fig. A.16. Experimental Strain Rate and Model Strain Rate for the Limestone Mix at A) High, B) Medium, and C) Low Stress Levels and 0 psi Confinement

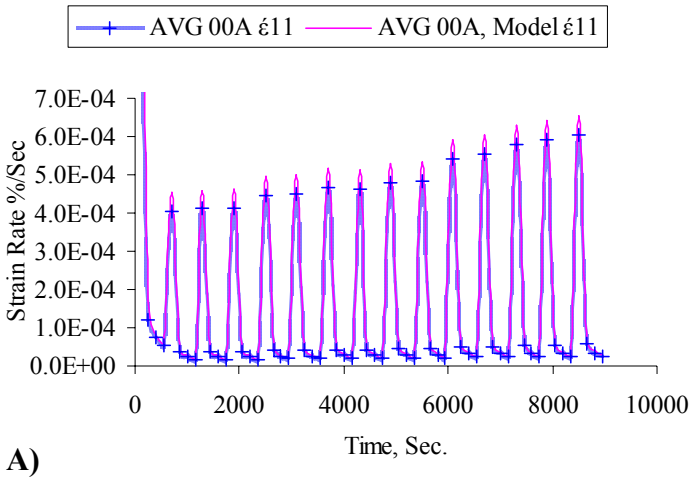

A)

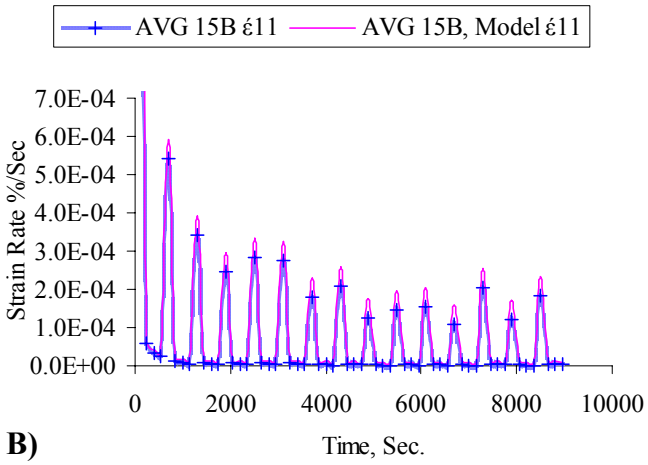

B)

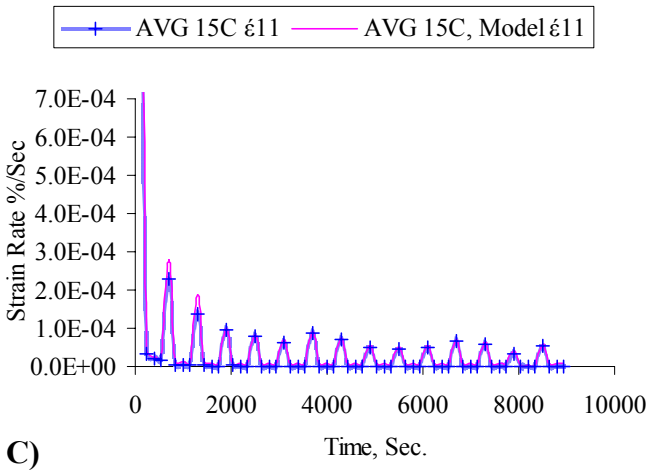

C)

Fig. A.17. Experimental Strain Rate and Model Strain Rate for the Limestone Mix at A) High, B) Medium, and C) Low Stress Levels and 15 psi Confinement

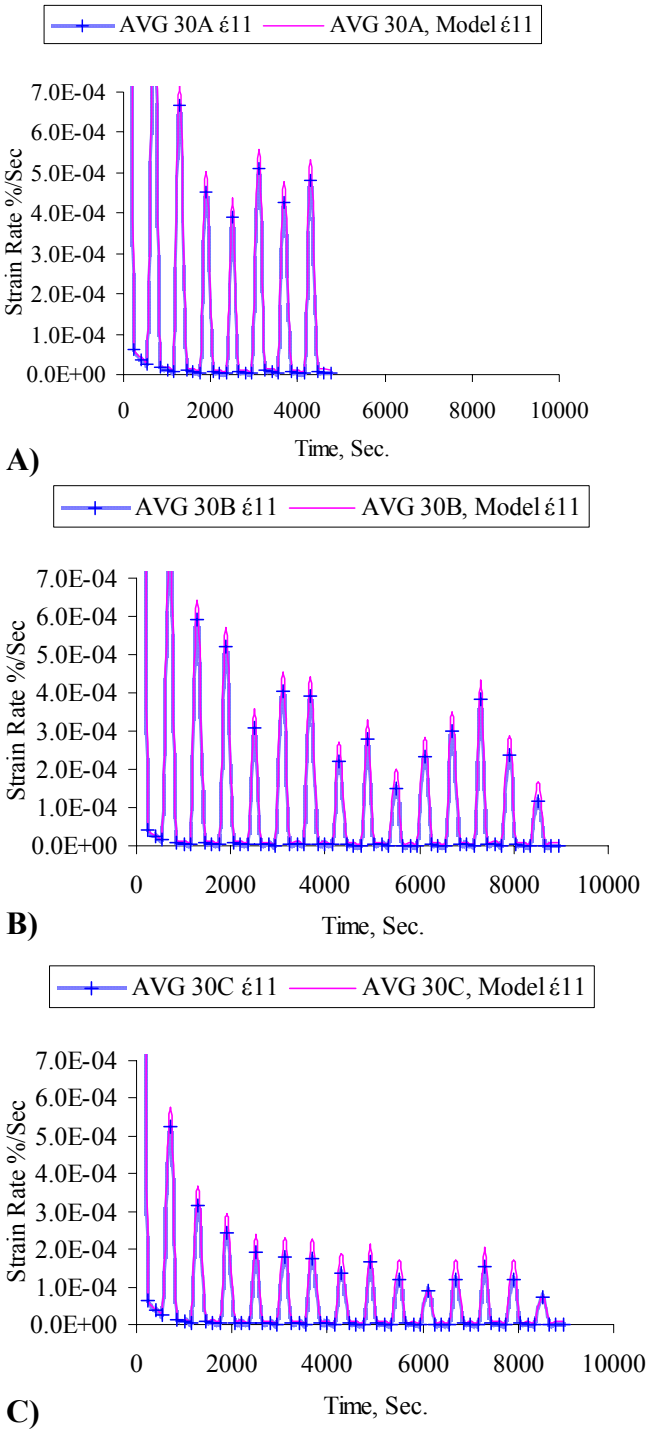

Fig. A.18. Experimental Strain Rate and Model Strain Rate for the Limestone Mix at A) High, B) Medium, and C) Low Stress Levels and 30 psi Confinement

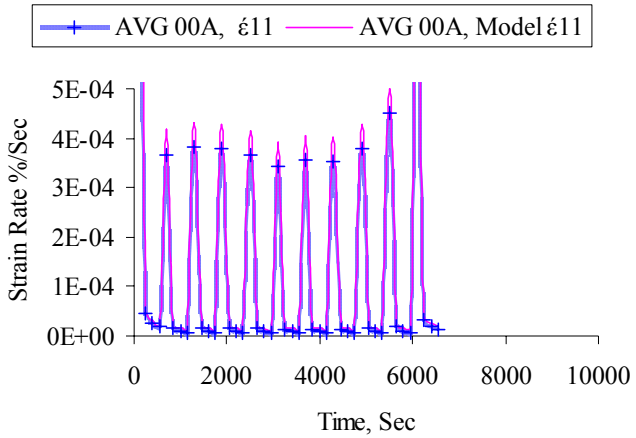

A)

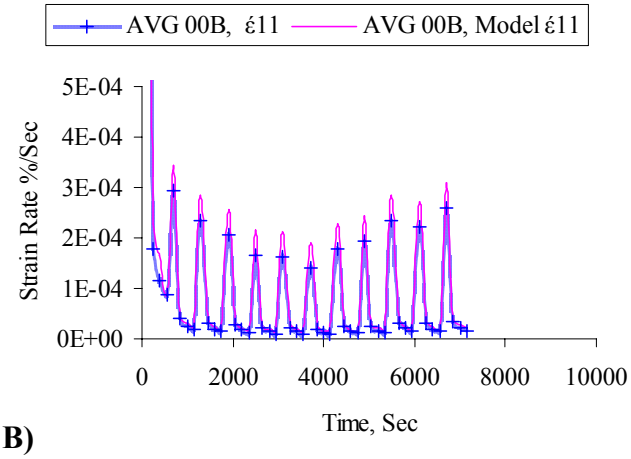

B)

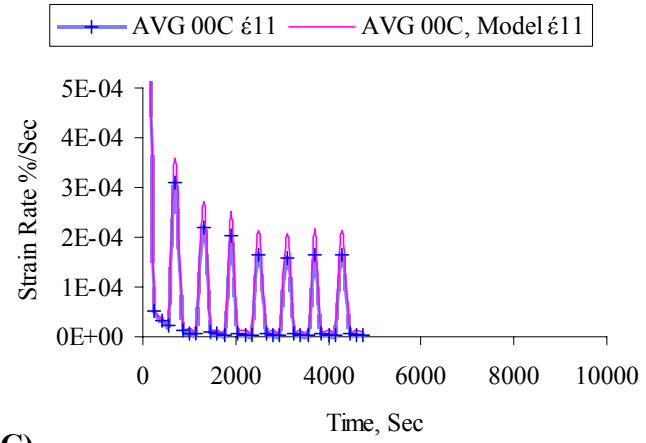

C)

Fig. A.19. Experimental Strain Rate and Model Strain Rate for the Granite Mix at A) High, B) Medium, and C) Low Stress Levels and 0 psi Confinement

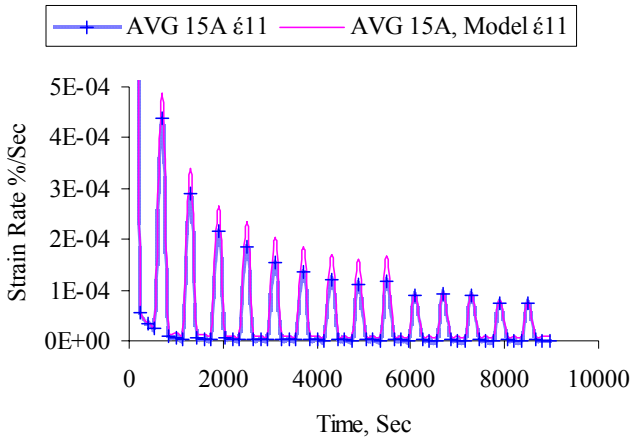

A)

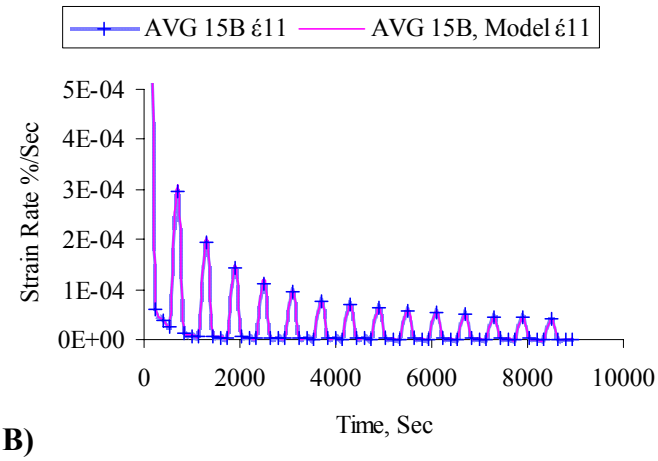

B)

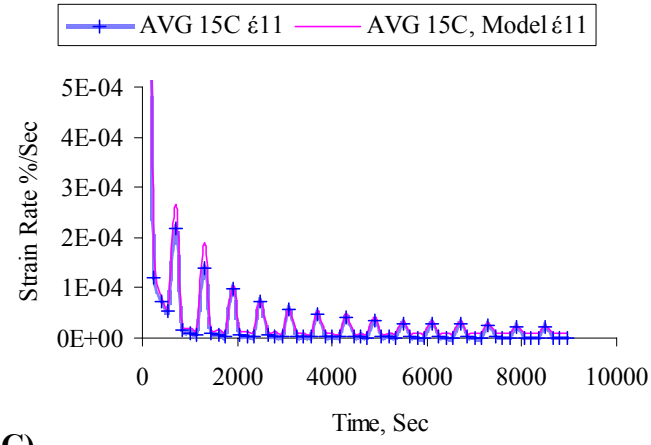

C)

Fig. A.20. Experimental Strain Rate and Model Strain Rate for the Granite Mix at A) High, B) Medium, and C) Low Stress Levels and 15 psi Confinement

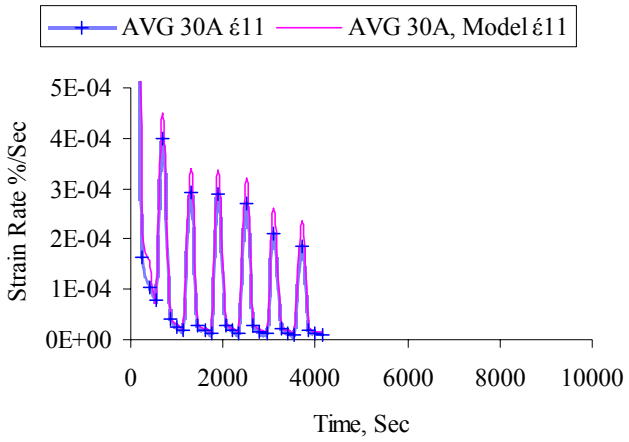

A)

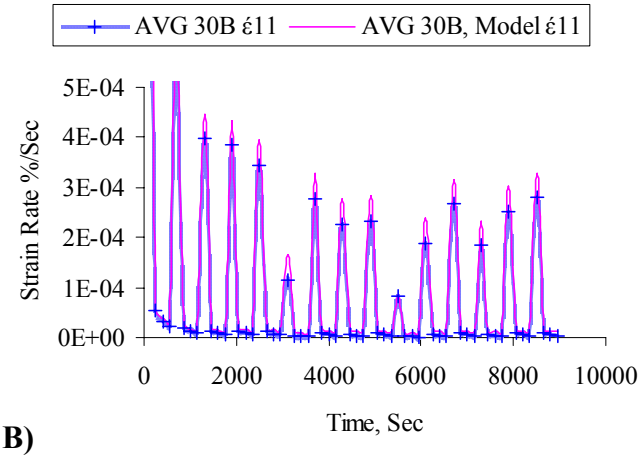

B)

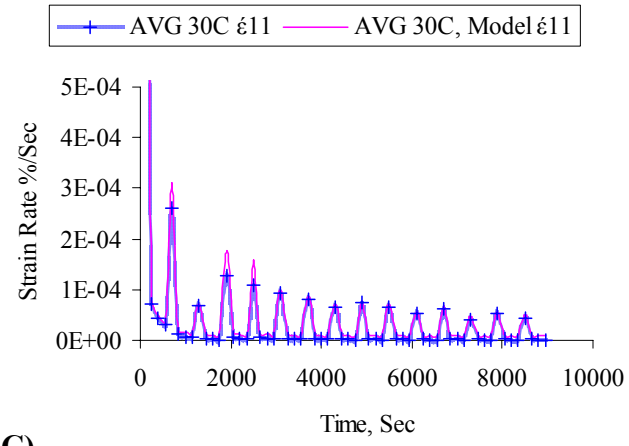

C)

Fig. A.21. Experimental Strain Rate and Model Strain Rate for the Granite Mix at A) High, B) Medium, and C) Low Stress Levels and 30 psi Confinement

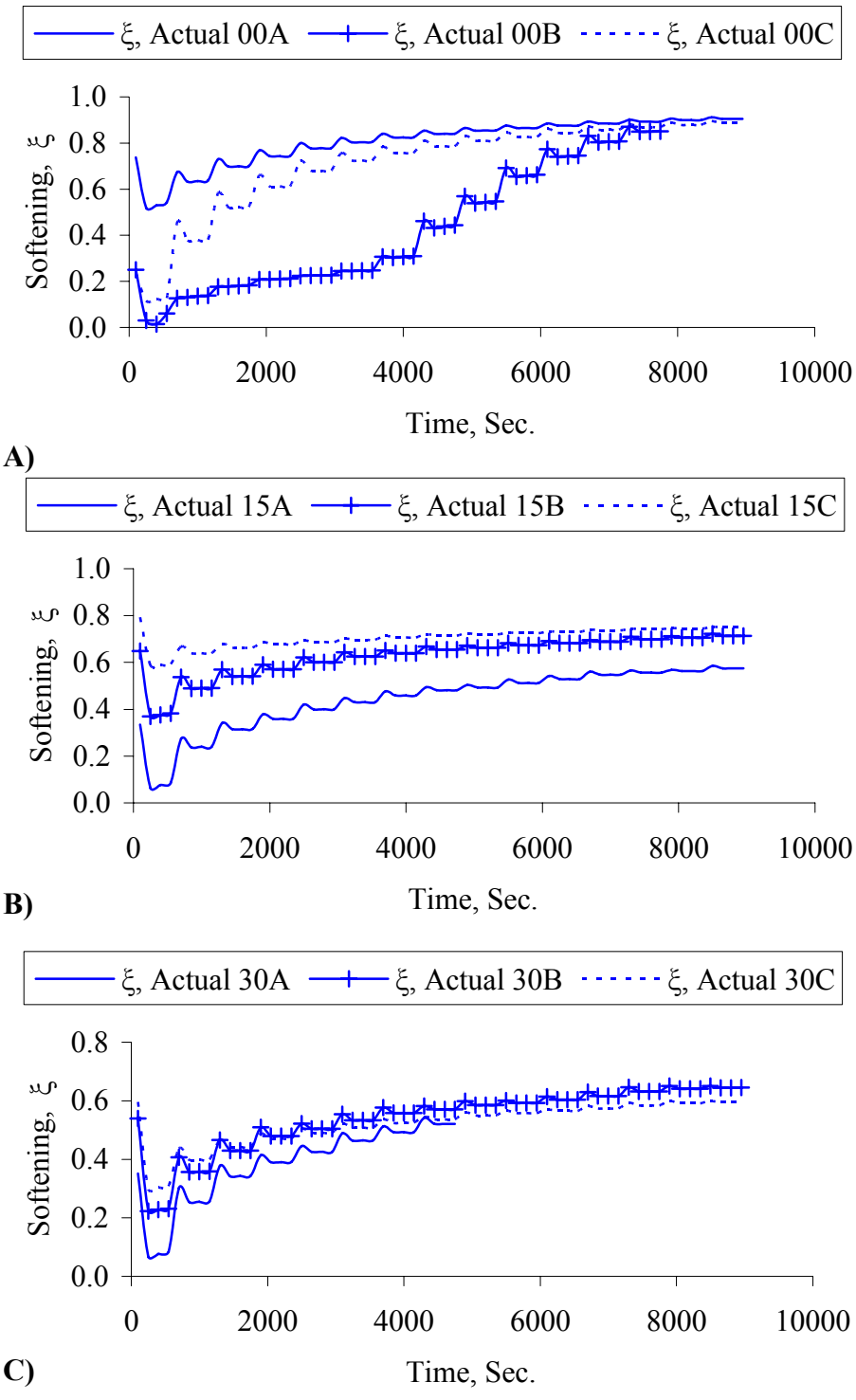

Fig. A.22. The Softening Parameter ξ for the Limestone Mix at A) 0, B) 15, and C) 30 psi Confinement

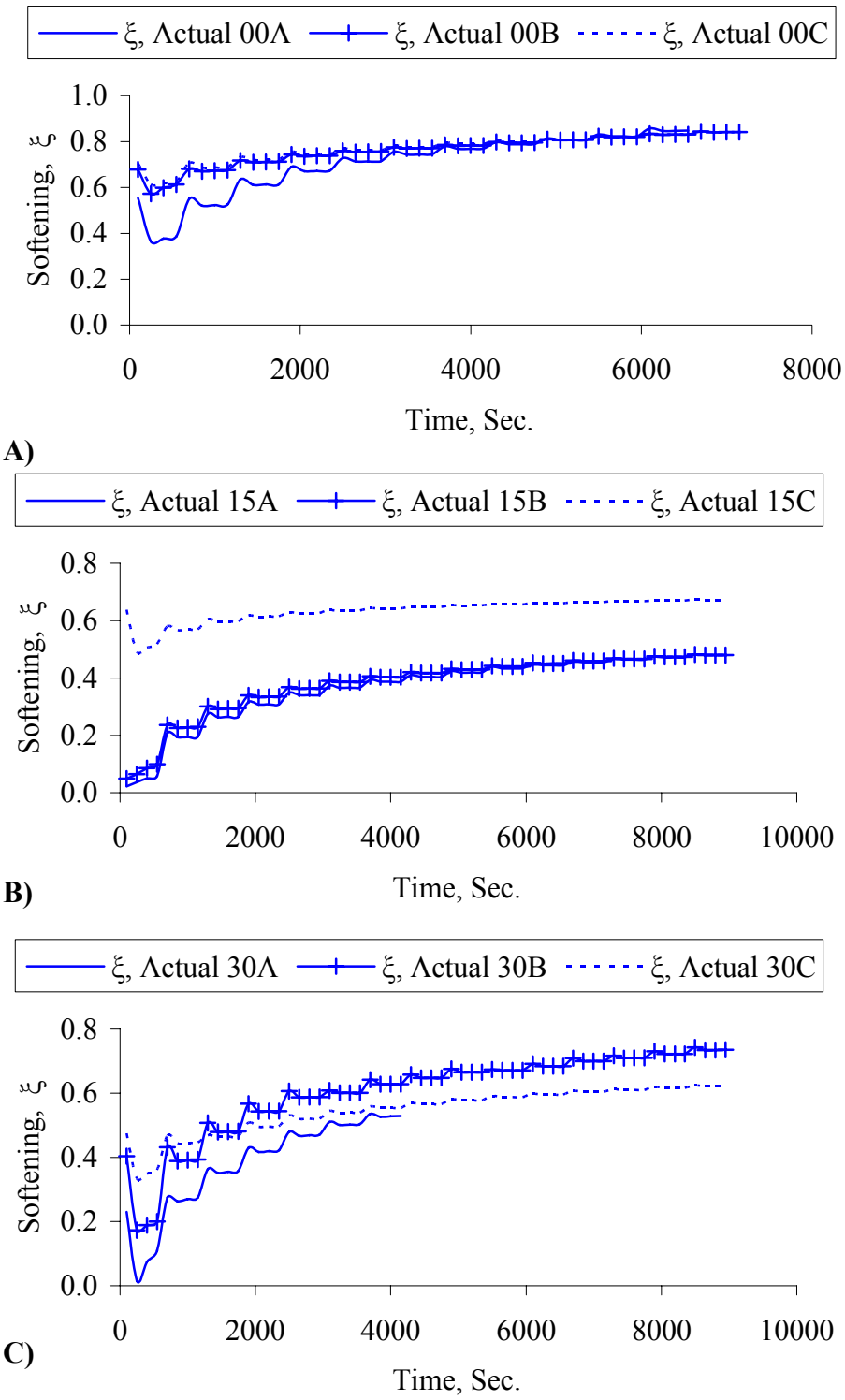

Fig. A.23. The Softening Parameter ξ for the Granite Mix at A) 0, B) 15, and C) 30 psi Confinement

VITA

Shadi Abdel-Rahman Saadeh was born in Amman, Jordan, on July 15, 1975. He received his Bachelor of Science in civil engineering from the University of Jordan in June 1997. He worked as civil engineer at Omrania and Associates between October 1997 and February 1999. He worked with Electro Industries as a project engineer between March 1999 and August 2000.

He joined the graduate school at Washington State University in January 2001 and received his Master of Science in civil engineering in May 2002. He started his Ph.D. program in civil engineering at Washington State University in May 2002. Shadi transferred to Texas A&M University in January 2003 and received his Ph.D. in December 2005. His address is as follows:

P.O. Box 230903

Amman 11132 Jordan